

## Site U1405<sup>1</sup>

R.D. Norris, P.A. Wilson, P. Blum, A. Fehr, C. Agnini, A. Bornemann, S. Boulila, P.R. Bown, C. Cournede, O. Friedrich, A.K. Ghosh, C.J. Hollis, P.M. Hull, K. Jo, C.K. Junium, M. Kaneko, D. Liebrand, P.C. Lippert, Z. Liu, H. Matsui, K. Moriya, H. Nishi, B.N. Opdyke, D. Penman, B. Romans, H.D. Scher, P. Sexton, H. Takagi, S.K. Turner, J.H. Whiteside, T. Yamaguchi, and Y. Yamamoto<sup>2</sup>

### Chapter contents

Background and objectives .....	1
Operations .....	2
Lithostratigraphy .....	3
Biostratigraphy .....	7
Paleomagnetism .....	10
Age-depth model and mass accumulation rates .....	13
Geochemistry .....	14
Physical properties .....	16
Stratigraphic correlation .....	17
References .....	18
Figures .....	21
Tables .....	72

### Background and objectives

Integrated Ocean Drilling Program (IODP) Site U1405 (proposed Site JA-14A; 40°08.30'N, 51°49.20'W; 4287 m water depth) (Fig. F1) is a mid- to deepwater site located on J-Anomaly Ridge that was planned to capture a record of sedimentation 657 m shallower than the largely sub-carbonate compensation depth (CCD) record drilled at Site U1403 (Figs. F2, F3, F4). Our scientific objectives for drilling Site U1405 were

- To test the hypothesis that this seismically homogeneous package is a plastered drift deposit of Paleogene age,
- To obtain a sedimentary section suited to paleoceanographic study at suborbital timescales featuring very high rates of deposition compared to those typically found in deep sea pelagic sites (1–2 cm/k.y.), and
- To capture excursions of the Cenozoic CCD (Figs. F2, F3).

Coring at Site U1404 recovered an ~300 m thick sequence of clays and oozes of Miocene, Oligocene, and late middle to late Eocene age featuring distinct increases in calcium carbonate content in sediment of Eocene, Eocene–Oligocene transition (EOT), and late Oligocene–early Miocene age. Prior to drilling, Site U1405 was hypothesized to be more carbonate rich than Site U1404 in time-equivalent strata and also a sensitive recorder of those CCD shoaling and deepening events not quite large enough to have triggered changes in calcium carbonate accumulation at Site U1404. Initial results from Site U1403 indicated that the CCD in the North Atlantic Ocean during the early Eocene was much deeper (by ~1.5 km) than in the contemporaneous equatorial Pacific Ocean (Pälike et al., 2012), whereas initial results from Site U1404 indicated transient carbonate pulses and inferred CCD deepening events during the middle to late Eocene and EOT time intervals that bear some similarities to those seen in the Pacific Ocean. Coring at Site U1404 also recovered evidence of a pulse of carbonate deposition during the early Miocene and latest Oligocene that is not recognized in the tropical Pacific (Pälike et al., 2012). At Site U1405, our aim was to obtain a sedimentary record of one or more of these intervals of geologic time in shallower water than at Site U1404 and in a more expanded section to provide a more detailed paleoceanographic record of these events.

For the most part, average linear sediment accumulation rates documented at Site U1404 are characteristic of normal pelagic sedimentation ( $\leq 1.5$  cm/k.y.), but sedimentation rates in the latest

<sup>1</sup>Norris, R.D., Wilson, P.A., Blum, P., Fehr, A., Agnini, C., Bornemann, A., Boulila, S., Bown, P.R., Cournede, C., Friedrich, O., Ghosh, A.K., Hollis, C.J., Hull, P.M., Jo, K., Junium, C.K., Kaneko, M., Liebrand, D., Lippert, P.C., Liu, Z., Matsui, H., Moriya, K., Nishi, H., Opdyke, B.N., Penman, D., Romans, B., Scher, H.D., Sexton, P., Takagi, H., Turner, S.K., Whiteside, J.H., Yamaguchi, T., and Yamamoto, Y., 2014. Site U1405. In Norris, R.D., Wilson, P.A., Blum, P., and the Expedition 342 Scientists, *Proc. IODP*, 342: College Station, TX (Integrated Ocean Drilling Program). doi:10.2204/iodp.proc.342.106.2014

<sup>2</sup>Expedition 342 Scientists' addresses.



Oligocene and early Miocene are noticeably higher (~7 cm/k.y.) and closer to rates anticipated in sediment drift deposits. Site U1405 was positioned to penetrate the acoustically uniform sediment package at close to its maximum thickness (Fig. F4) to determine the extent to which these seismically distinctive features, common across J-Anomaly and Southeast Newfoundland Ridges, were in fact sediment drift deposits. Sediment drifts of Pliocene–Pleistocene age have been drilled in the northeast Atlantic and are shown to feature high sedimentation rates (4–20 cm/k.y.) suited to the study rates of abrupt climate change (e.g., Channell et al., 2010). At Site U1405, we expected to encounter a sediment sequence similar to that encountered at Site U1404 in terms of its overall stratigraphy, but we did not know whether upslope thickening between the two sites was attributable to higher long-term rates of carbonate burial in shallower water depths (a CCD effect) or to higher rates of clay or silica delivery to the site during geologically short intervals of time (drift sedimentation).

If our drilling target proved to be a Paleogene sediment drift with high accumulation rates, we hoped to obtain records for assessing rates of change in the Earth's system during transient episodes of extreme warming (analogous to the near future) and transitions from warm climates to the glaciated world. In particular, based on our results from Site U1404 we hoped to capture high-resolution sedimentary records of the late Eocene, EOT, and Oligocene–Miocene transition (Lyle, Wilson, Janecek, et al., 2002; Coxall et al., 2005; Holbourn et al., 2005; Pälike et al., 2006, 2012; Merico et al., 2008). In addition to our interest in CCD changes associated with these intervals, we also wanted to capture sediment archives to assess the debate concerning contemporaneous changes in global ice volume and competing hypotheses of the role for extensive pre-Pliocene glaciation in the northern hemisphere (e.g., Zachos et al., 1997; Tripati et al., 2005, 2007; Edgar et al., 2007; Eldrett et al., 2007; DeConto et al., 2008; Miller et al., 2008; Stickley et al., 2009; Liebrand et al., 2011).

Finally, drilling at Site U1405 was also needed to help understand the history of chemical stratification and ocean currents in the Paleogene North Atlantic Ocean. Most deep-ocean drill sites are located at mid-ocean depths in the Paleogene when we account for thermal subsidence. Hence, Site U1405 is rare in that it was selected to recover a representative sequence deposited in true deep water (~4000 meters below sea level [mbsl] in the Eocene). Furthermore, the site is well placed to record the history of deep water formed in the far North Atlantic, or even the Arctic, because the Deep Western Boundary Current

is constrained to flow directly over or around the Newfoundland ridges by geostrophic flow and the shape of the ocean basin. At the deep end of the J-Anomaly Ridge depth transect, the site should record the chemistry and flow history of abyssal waters in the Paleogene.

## Operations

All times are local ship time (UTC – 2.5 h). See Table T1 for coring summary.

### Hole U1405A summary

Latitude: 40°08.3001'N  
 Longitude: 51°49.1996'W  
 Water depth below sea level (m): 4285.8  
 Date started: 0745 h, 25 June 2012  
 Date finished: 1120 h, 27 June 2012  
 Time on hole (days): 2.1  
 Seafloor depth (m drilling depth below rig floor [DRF]): 4297.3  
 Seafloor depth estimation method: mudline core  
 Rig floor to sea level (m): 11.5  
 Penetration depth (m drilling depth below seafloor [DSF]): 308.6  
 Cored interval (m): 308.6  
 Recovered length (m): 270.34  
 Recovery (%): 88  
 Total cores (number): 33  
 Advanced piston corer (APC) cores (number): 26  
 Extended core barrel (XCB) cores (number): 7  
 Drilling system: 11 $\frac{1}{16}$  inch APC/XCB bit with 136.00 m bottom-hole assembly (BHA)  
 Objective: core from seafloor to ~250 m DSF  
 Result: target exceeded; objectives met

### Hole U1405B summary

Latitude: 40°08.2995'N  
 Longitude: 51°49.1845'W  
 Water depth below sea level (m): 4284.5  
 Date started: 1120 h, 27 June 2012  
 Date finished: 1610 h, 28 June 2012  
 Time on hole (days): 1.2  
 Seafloor depth (m DRF): 4296  
 Seafloor depth estimation method: mudline core  
 Rig floor to sea level (m): 11.5  
 Penetration depth (m DSF): 223.5  
 Cored interval (m): 218.5  
 Recovered length (m): 219.6  
 Recovery (%): 101  
 Drilled interval (m): 5  
 Drilled interval (number): 1  
 Total cores (number): 23  
 APC cores (number): 23



Drilling system: 11 $\frac{1}{16}$  inch APC/XCB bit with 136.00 m BHA  
 Objective: core from seafloor to ~250 m DSF  
 Result: target reached; objectives met

### Hole U1405C summary

Latitude: 40°08.2890'N  
 Longitude: 51°49.1847'W  
 Water depth below sea level (m): 4287.3  
 Date started: 1610 h, 28 June 2012  
 Date finished: 0200 h, 30 June 2012  
 Time on hole (days): 1.4  
 Seafloor depth (m DRF): 4298.8  
 Seafloor depth estimation method: mudline core  
 Rig floor to sea level (m): 11.52  
 Penetration depth (m DSF): 232.0  
 Cored interval (m): 232  
 Recovered length (m): 227.77  
 Recovery (%): 98  
 Total cores (number): 25  
 APC cores (number): 25  
 Drilling system: 11 $\frac{1}{16}$  inch APC/XCB bit with 136.00 m BHA  
 Objective: repeat cored sequence from Holes U1405A and U1405B  
 Result: target reached; objectives met

### Description

The vessel arrived at Site U1405 after a 7.5 nmi transit from Site U1404. The transit was made in dynamic positioning mode at a speed of 0.8 kt with the drill pipe suspended below the vessel. The vessel stabilized over Site U1405 at 0745 h on 25 June 2012. The plan for this site called for drilling three holes to a depth of ~250 m DSF. Holes U1405A–U1405C were successfully cored to depths of 308.6, 223.5, and 232.0 m DSF, respectively, without any significant problems.

### Hole U1405A coring

Hole U1405A was spudded at 1140 h on 25 June 2012, and a 6.2 m mudline core established seafloor depth at 4297.3 m below rig floor (DRF; 4285.8 mbsl). Cores 342-U1405A-1H through 26H were recovered from the seafloor to 241.9 m DSF using non-magnetic core barrels and the FlexIT core orientation tool. Advanced piston corer temperature tool (APCT-3) measurements were taken on Cores 4H, 7H, and 10H with good results. The first partial stroke was experienced with Core 26H, and the liner and core had to be pumped out of the core barrel. The XCB was deployed for Cores 27X through 33X to a total depth of 308.6 m DSF. The seafloor was cleared at 1120 h on 27 June, ending Hole U1405A. Overall core recovery for Hole U1405A was 270.34 m for the 308.6 m

interval cored (88% recovery). Total time spent on Hole U1405A was 51.6 h.

### Hole U1405B coring

The vessel was offset 20 m east, and Hole U1405B was spudded at 1305 h on 27 June. A 9.5 m mudline core established seafloor depth at 4296.0 m DRF (4284.5 mbsl). Cores 342-U1405B-1H through 24H were recovered from the seafloor to 218.5 m DSF using nonmagnetic core barrels and the FlexIT core orientation tool. An interval of 5 m was drilled without coring in an attempt to cover coring gaps in Hole U1405A. The seafloor was cleared at 1610 h on 28 June, ending Hole U1405B. Coring the 218.5 m interval yielded 219.60 m of core (101% recovery). The total time spent on Hole U1405B was 29.0 h.

### Hole U1405C coring

The vessel was offset 20 m south. Hole U1405C was spudded at 1915 h on 28 June and a 6.7 m mudline core established seafloor depth at 4298.8 m DRF (4287.3 mbsl). Cores 342-U1405C-1H through 25H were recovered to a total depth of 232.0 m DSF using nonmagnetic core barrels and the FlexIT core orientation tool. The cored interval of 232.0 m yielded 227.77 m of core (98% recovery). The total time spent on Hole U1405C was 33.75 h. The seafloor was cleared at 0200 h on 30 June, ending Hole U1405C.

After clearing the seafloor, the drill string was tripped to ~3500 m DRF and the vessel began moving in dynamic positioning mode to the next site at a speed of 1.5 kt. The positioning beacon was left on-site to minimize the risk of losing it during recovery in difficult weather conditions. The beacon was recovered after operations at Site U1406 were complete. The total time spent at Site U1405 was 114.25 h (4.8 days).

### Lithostratigraphy

Drilling operations in Holes U1405A–U1405C recovered an ~309 m thick sequence of pelagic sediment of Pleistocene to late Oligocene age, including an exceptionally expanded record of the Oligocene–Miocene transition. The lithology at Site U1405 is divided into two lithostratigraphic units. The upper unit (I) is divided into two subunits, and the lower unit (II) is divided into three subunits (Figs. F5, F6; Table T2).

The uppermost ~20 m (Unit I) of the sediment column at Site U1405 is composed of Pleistocene to Pliocene clay with abundant nannofossils, foraminifers, and manganese nodules. Subunit Ia is underlain by the carbonate-free silty clay of Subunit Ib. The

underlying ~280 m (Unit II) is lower Miocene to upper Oligocene clay and biogenic ooze characterized by greenish gray color and varying abundances of diatoms, radiolarians, and calcareous nannofossils. Subunit IIb, ~10 m of clayey nannofossil and biosiliceous ooze in the middle of Unit II, is characterized by several distinct layers of lighter colored ooze with a higher nannofossil abundance around the Oligocene/Miocene boundary.

Lithostratigraphic units and boundaries are defined by changes in lithology (as identified by macroscopic core description and microscopic smear slide observations), physical properties, color reflectance ( $L^*$ ,  $a^*$ , and  $b^*$ ), and biogenic content (calcium carbonate and silica). The lithologic differences observed between units are primarily attributable to varying abundance of nannofossils, diatoms, radiolarians, and foraminifers (Figs. F7, F8, F9, F10). Lithologic descriptions are based on sediment recovered from Hole U1405A and supplemented with observations from Holes U1405B and U1405C.

## Unit I

Intervals: 342-U1405A-1H-1, 0 cm, to 3H-2, 30 cm; 342-U1405B-1H-1, 0 cm, to 3H-2, 24 cm; 342-U1405C-1H-1, 0 cm, to 2H-6, 14 cm

Depths: Hole U1405A = 0.00–17.51 meters below seafloor (mbsf); Hole U1405B = 0.00–20.74 mbsf; Hole U1405C = 0.00–14.34 mbsf

Age: Pleistocene to Pliocene

Lithology: clay and nannofossil ooze

Unit I and its subunits (Ia and Ib) comprise the uppermost 15–20 m of the sediment column at Site U1405. The principal lithology of Unit I is brown to light brownish gray (most common is 10YR 5/3 but includes 7.5YR 5/3, 10YR 6/2, 10YR 6/3, and 2.5Y 6/1) clay and nannofossil ooze with varying abundances of foraminifers and silt-sized quartz. The unit includes (from most to least common): clay with silt, silty clay, nannofossil clay, foraminiferal nannofossil ooze, nannofossil ooze, and nannofossil clay with foraminifers. Manganese nodules ranging from millimeter to centimeter scale are found throughout. Bioturbation is heavy to complete throughout Unit I with no discrete layers or burrows visible. Magnetic susceptibility is higher in Unit I than in Unit II, decreasing gradually over several sections above the unit boundary. The Unit I/II boundary is defined by a color and lithologic change and occurs sharply over ~1 cm. Unit I is divided into two subunits based on the presence (Subunit Ia) or absence (Subunit Ib) of calcium carbonate and calcareous nannofossils and/or foraminifers in smear slide analysis (Figs. F7, F8, F9, F10) and supported by subsequent shipboard measurements of carbonate content (Fig. F5).

## Subunit Ia

Intervals: 342-U1405A-1H-1, 0 cm, to 2H-4, 0 cm; 342-U1405B-1H-1, 0 cm, to 1H-2, 75 cm; 342-U1405C-1H-1, 0 cm, to 1H-4, 16 cm

Depths: Hole U1405A = 0.00–10.70 mbsf; Hole U1405B = 0.00–2.25 mbsf; Hole U1405C = 0.00–4.66 mbsf

Age: Pleistocene to late Pliocene

Lithologies: foraminiferal sand and nannofossil ooze

Sand-sized foraminifers are common to abundant in the uppermost ~3 m of the sediment column in all three holes. The uppermost 5.6 m of Hole U1405A is composed of a distinct bed of foraminiferal sand, which is likely the best representation of a true mudline. Holes U1405B and U1405C likely did not recover the uppermost few meters of the sediment column. Foraminiferal abundance decreases downhole, yet calcareous nannofossil abundance remains high for the remainder of Subunit Ia (10.70 m total thickness in Hole U1405A). The boundary between Subunits Ia and Ib is defined as the lowest occurrence of “few” (1%–10%) or greater nannofossils in smear slide analysis. This definition is supported by carbonate content data in Hole U1405A that show a gradual decrease from a peak of 40 wt% in the uppermost foraminiferal sand to <1 wt% in uppermost Subunit Ib. The only sand-sized or larger lithic grains (presumably ice-raftered debris) described in Subunit Ia are three rounded lithic cobbles found in a visibly disturbed interval (likely fall-in) in the uppermost 5 cm of Section 342-U1405C-1H-1.

## Subunit Ib

Intervals: 342-U1405A-2H-4, 0 cm, to 3H-2, 30 cm; 342-U1405B-1H-2, 75 cm, to 3H-2, 24 cm; 342-U1405C-1H-4, 16 cm, to 2H-6, 14 cm

Depths: Hole U1405A = 10.70–17.51 mbsf; Hole U1405B = 2.25–20.74 mbsf; Hole U1405C = 4.66–14.34 mbsf

Age: late Pliocene

Lithologies: clay and silty clay

Subunit Ib is silty clay ranging in color from light yellowish brown (10YR 6/4 and 10YR 6/6) to pale brown (10YR 6/3). Manganese occurs as centimeter-scale nodules and also as submillimeter-scale flecks commonly concentrated in distinct centimeter-scale dark layers. Silt-sized sediment is mostly rounded to subangular quartz, but feldspar, mica, and heavy minerals including zircons are also present in low abundances. No sand-sized or larger lithic grains were identified by visual core description in Subunit Ib. The contact between this yellowish brown sediment and the distinctively greenish gray sediment in underlying lithostratigraphic Unit II is readily appar-



ent (Fig. F5). In Holes U1405A and U1405C, the Unit I/II boundary occurs as a very sharp contact. However, in Hole U1405B, a two-step color change is observed. Between the pale brown (10YR 6/3 to 2.5Y 6/2) of Subunit Ib and the distinctive greenish gray (5GY 6/1 to 5GY 5/1) of Unit II is a distinct 20 cm layer of gray (2.5Y 6/1) carbonate-free silty clay. Based on smear slide analysis, the silty clay of this gray intermediate interval is assigned to Subunit Ib.

## Unit II

Intervals: 342-U1405A-3H-2, 30 cm, to 33X-CC, 40 cm; 342-U1405B-3H-2, 24 cm, to 24H-CC, 28 cm; 342-U1405C-2H-6, 13 cm, to 25H-CC, 20 cm

Depths: Hole U1405A = 17.51–307.03 mbsf; Hole U1405B = 20.74–223.30 mbsf; Hole U1405C = 14.34–232.35 mbsf

Age: middle Miocene to late Oligocene

Lithology: clay, biosiliceous ooze, and nannofossil ooze

Unit II and its subunits (IIa, IIb, and IIc) comprise an ~280 m thick sequence of clay with abundant calcareous nannofossils, diatoms, and radiolarians. Commonly no component makes up >50% of total smear slide abundance. As with all lithologic names, the major lithology indicates the most abundant component, the preceding modifier indicates abundant (>25%) components, and the succeeding modifier indicates common (10%–25%) components. For example, a “radiolarian nannofossil ooze with clay” describes an ooze in which nannofossils are the most abundant component (but not necessarily >50%), radiolarians are abundant (>25%), and clay is common (10%–25%). The terms “biosiliceous ooze” and “clayey biosiliceous ooze” are used to denote sediment in which the combined biosiliceous components (i.e., diatoms + radiolarians) are more abundant than any other component (e.g., a sediment composed of 10% clay, 30% calcareous nannofossils, 30% radiolarians, and 30% diatoms would be called a nannofossil biosiliceous ooze with clay). These terms are distinguished from, for example, “radiolarian ooze,” which would imply radiolarians alone as the most abundant component. Under this terminology, the most common major lithologies in Unit II are clay, biosiliceous ooze, and nannofossil ooze. Note that the assignment of lithology in the visual core descriptions is done primarily on the basis of smear slides, without the benefit of carbonate content data, which are acquired later. Comparison of smear slide-based lithologic names with carbonate data suggests that core description tends to overestimate the nannofossil component and underestimate the clay component. In Unit II, most lithologies described as nannofossil ooze contain 20–40 wt% carbonate.

Unit II is characterized by distinctive greenish gray biosiliceous ooze. The most common Munsell description is 5GY 5/1 (greenish gray) in Subunits IIa and IIb and 10Y 4/1 (dark greenish gray) in Subunit IIc. Throughout the unit, however, there are slight centimeter- to meter-scale alternations between the dominant lighter green (5GY 5/1) intervals and darker greenish gray (10Y 4/1 and 5GY 4/1) intervals that appear brownish by comparison. Submillimeter-scale black sulfide flecks and centimeter-scale sulfide mottles are present throughout Unit II. Occasional darker green (5G 4/1) layers and mottles contain a greater abundance of glauconite in smear slide analysis. Bioturbation is heavy, with individual burrows rarely visible, but centimeter-scale color alternations and distinct horizons of lighter, nannofossil-rich sediment (see “[Subunit IIb](#)”) are preserved. The overall lithologies of Subunits IIa and IIc are similar. However, Subunit IIb is distinguished from the overlying and underlying subunits by the presence of intervals of high nannofossil abundance nearly contemporaneous with the biostratigraphically defined Oligocene–Miocene transition (Figs. F11, F12, F13). Subunits IIa and IIc are not devoid of carbonate but generally lack the clearly defined lighter units seen in Subunit IIb. Color reflectance ( $L^*$ ) data in Hole U1405A show cyclic variations throughout Unit II (Figs. F5, F6, F11, F12, F14). Power spectrum and filtering show, in particular, two prominent cyclicities of wavelengths of 16.4 and 4.3 m throughout the lower Miocene, which may reflect an orbitally induced control on sediment composition.

X-ray diffraction (XRD) (Fig. F15) analyses show significant abundances of the clay minerals chlorite, illite, and kaolinite throughout Unit II, suggesting relatively consistent contributions of each clay mineral. However, thorough quantification of the clay mineral assemblage would require analysis of the micrometer size fraction at much higher resolution than shipboard sampling allows. Calcite occurs in some XRD analyses and not others, consistent with carbonate data and smear slide analysis. Several microfaults were found throughout Unit II, in most cases pyritized along the fault surface. Magnetic susceptibility in Unit II is lower and more stable than in the overlying Unit I.

## Subunit IIa

Intervals: 342-U1405A-3H-2, 30 cm, to 16H-2, 20 cm; 342-U1405B-3H-2, 24 cm, to 16H-3, 20 cm; 342-U1405C-2H-6, 13 cm, to 16H-4, 34 cm

Depths: Hole U1405A = 17.51–140.98 mbsf; Hole U1405B = 20.74–141.20 mbsf; Hole U1405C = 14.34–144.54 mbsf

Age: early Miocene

Lithologies: clay and biosiliceous ooze



The lithology of Subunit IIa is clay with varying abundances of several biogenic components: diatoms, radiolarians, nannofossils, and sponge spicules. Individual lithologies are classified variously as (from most common to least common) clay, clay with biosilica, biosiliceous clay, clay with nannofossils, nannofossil clay, clayey biosiliceous ooze, clayey nannofossil ooze, biosiliceous ooze with clay, and nannofossil ooze with clay. The most common color is greenish gray (5GY 5/1) but ranges to other shades of greenish gray (10GY 5/1 and 10GY 6/1) and dark greenish gray (5GY 4/1).

### Subunit IIb

Intervals: 342-U1405A-16H-2, 20 cm, to 23H-1, 150 cm; 342-U1405B-16H-3, 20 cm, to 22H-7, 7 cm; 342-U1405C-16H-4, 34 cm, to 22H-7, 60 cm

Depth: Hole U1405A = 140.98–207.20 mbsf; Hole U1405B = 141.20–202.20 mbsf; Hole U1405C = 144.54–203.70 mbsf

Age: late Oligocene to early Miocene

Lithologies: clay, biosiliceous ooze, and nannofossil ooze

The general lithology of Subunit IIb is clay with varying contributions of diatoms, radiolarians, and calcareous nannofossils, similar to the overlying and underlying lithostratigraphic Subunits IIa and IIc. Subunit IIb, however, contains four prominent light-colored intervals (Layers I–IV in Fig. F11). Each of these layers is characterized by higher carbonate content, higher calcareous nannofossil abundance, and paler color (5GY 6/1 or 10Y 5/1) than the rest of Unit II (5GY 5/1 to 5GY 4/1).

The stratigraphically highest of these layers, Layer I, occurs in Cores 342-U1405B-16H and 342-U1405C-16H (Figs. F11, F12) but is not present in Hole U1405A, perhaps falling in a core gap. The top of Layer I marks the lithologic contact between Subunits IIa and IIb. In Core 342-U1405C-16H, Layer I contains high carbonate content (peaking at 35 wt%) and abundant calcareous nannofossil *Braarudosphaera*. The upper contact of Layer I in Core 342-U1405C-16H is sharp, a feature common among the four prominent light-colored layers observed in Subunit IIb. The upper contact of the corresponding Layer I in Core 342-U1405B-16H is gradational, which is different than in Core 342-U1405C-16H.

Calcareous nannofossil biostratigraphy constrains the Oligocene/Miocene boundary to immediately above the top of the second light-colored interval (Layer II) in Section 342-U1405A-19H-6, 48 cm (175.68 mbsf). Calcareous nannofossil abundance by smear slide analysis is higher in this interval (abundant to very abundant), and color is a lighter greenish gray (5GY 6/1) than underlying and overlying

strata (5GY 5/1). Carbonate content peaks in Core 342-U1405A-19H at 35 wt% within the lightest colored interval, as compared with <10% in the overlying and underlying darker strata (Fig. F11). The light color of this interval in Holes U1405A and U1405B has a sharp upper contact and a gradational lower transition on a decimeter scale (Fig. F12). This repeated stratigraphic pattern may reflect a carbonate accumulation event with gradual onset and abrupt termination or erosional truncation. Conversely, it may reflect a clay influx event with abrupt onset and gradual waning. The upper contact in Hole U1405C is obscured by drilling disturbance.

At ~5–8 m below Layer II, another similar light-colored nannofossil-rich interval (Layer III) occurs in all three holes in Core 20H near the Chron C6Cn.3n/C6Cn.2r boundary. Carbonate measurements in Cores 342-U1405A-20H and 342-U1405B-20H document an increase similar to the one seen in Layer II in Core 342-U1405A-19H, but the increase in carbonate content is of even greater amplitude (peak of 56 wt% in Core 342-U1405B-20H in Fig. F11). Much of this increase in carbonate in both intervals (Layers II and III) seems to be driven by calcareous nannofossil abundance, in particular *Braarudosphaera*, which is generally not observed with the exception of the four carbonate-rich intervals in Subunit IIb (i.e., Layers I–IV). The light-colored interval in Core 342-U1405A-20H has the same sharp upper and gradational lower contact observed in Layer I of Hole U1405C and Layer II of Holes U1405A and U1405B (Fig. F12). In contrast, the upper contact appears more gradual in Holes U1405B and U1405C, occurring over ~5 cm. The highest carbonate content and lightest color in Layer III of Hole U1405B occurs ~10 cm below the onset of the gradational color change (178 mbsf).

Layer IV is observed in Cores 342-U1405A-23H and 342-U1405B-22H and is the thinnest (10–20 cm) of the four light-colored layers. Because of the gradational nature of the lower contact of Layer IV, the placement of the lithologic contact between Subunits IIb and IIc is assigned based on the first darker Munsell color description, ~1 m below the lowermost peak in carbonate.

### Subunit IIc

Intervals: 342-U1405A-23H-2, 0 cm, to 33X-CC, 40 cm; 342-U1405B-22H-7, 7 cm, to 24H-CC, 28 cm; 342-U1405C-23H-1, 0 cm, to 25H-CC, 20 cm

Depths: Hole U1405A = 207.20–307.03 mbsf; Hole U1405B = 202.20–223.30 mbsf; Hole U1405C = 203.70–232.35 mbsf

Age: late Oligocene

Lithologies: clay, biosiliceous ooze, and nannofossil claystone



The lithology of Subunit IIc is overall very similar to that of Subunit IIa, consisting of alternating layers of mostly clay with varying contributions of biogenic components. Individual beds are classified variously as clay, clay with biosilica, biosiliceous clay, clay with nannofossils, nannofossil clay, clayey biosiliceous ooze, clayey nannofossil ooze, biosiliceous ooze with clay, nannofossil chalk, and nannofossil ooze with clay. The color is on average slightly darker than in Subunit IIa. The most common color is dark greenish gray (5GY 4/1), although the greenish gray (5GY 5/1) characteristic of Subunit IIa is also common. The lower 65 m of Subunit IIc is fractured and bisected by XCB coring in Cores 342-U1405A-27X through 33X (241.90–307.03 mbsf). The lithology of the XCB-cored interval consists of biosiliceous nannofossil ooze with clay (10Y 4/1) and nannofossil claystone (5GY 4/1). Sand-sized lithic grains were observed in Sections 342-U1405A-20H-4, 23H-1, 33X-2, and 33X-4, predominantly within the 63–150 µm sieve size fraction. Angular silt-sized quartz crystals, often showing conchoidal fractures, and various lithic fragments were found. The composition and size of these late Oligocene siliciclastics is very similar to those observed in the earliest Oligocene of Site U1404.

### Lithostratigraphic unit summary

Site U1405 sediment is composed of ~20 m of Pliocene to Pleistocene aged clay and nannofossil ooze (Unit I) overlying an expanded sequence of late Oligocene to early Miocene biosiliceous ooze and clay (Unit II). Carbonate contents vary considerably within the average range of 0 to 25 wt% throughout most of Unit II, with a few extreme values of up to 56 wt% suggesting that Site U1405 was very near or just above the CCD throughout most of the late Oligocene to early Miocene. Several light-colored beds in Subunit IIb document conspicuous fluctuations of carbonate content around the Oligocene/Miocene boundary, possibly the result of CCD fluctuations, carbonate production, and/or sea level, among other causes. However, the large range in carbonate content throughout Unit II and subtle, cyclical oscillations in color reflectance data suggest that perhaps these carbonate content fluctuations may be present throughout the stratigraphic range of Unit II at Site U1405, albeit undetected by the coarse resolution of shipboard carbonate sampling.

Lithostratigraphic Unit II at Site U1405 can be correlated to the upper part of Unit II at deeper water Site U1404, which also recovered a distinctive greenish gray unit of Oligocene–Miocene age of overall simi-

lar lithologic composition but with less carbonate content. The time-correlative equivalent of Unit II at Site U1405 at the deepest Expedition 342 Site U1403 is completely barren of carbonate.

## Biostratigraphy

Coring at Site U1405 recovered a 307 m thick sequence of Pleistocene to upper Oligocene clays, biosiliceous nannofossil ooze, and nannofossil ooze. Nannofossils and planktonic foraminifers are present in the uppermost brown foraminifer sandy clay and nannofossil ooze (Core 342-U1405A-1H; 0–6.18 mbsf) and indicate Quaternary to Pliocene ages (nannofossil Zones NN19–NN15/NN14). We were unable to provide biostratigraphic ages for the interval between 6.18 and 26.20 mbsf because of the absence of siliceous and calcareous microfossils. Below 26.20 mbsf, nannofossils, planktonic foraminifers, and radiolarians provide a well-defined biostratigraphy indicating upper lower Miocene to upper Oligocene sediment with relatively high sedimentation rates (1.4–10 cm/k.y.). Benthic foraminifers are generally rare throughout the entire sequence (the “present” category) but are well preserved and dominated by infaunal taxa, suggesting high organic matter flux to the seafloor.

An integrated calcareous and siliceous microfossil biozonation is shown in Figure F16. An age-depth plot including biostratigraphic and paleomagnetic datums is shown in Figure F17. Datum and zonal determinations from nannofossils, planktonic foraminifers, and radiolarians are in close agreement. The incorporated paleomagnetic data have helped to identify four relatively short hiatuses, each of ~1–2 m.y. duration, within the lower Miocene between 13.5 and 22 Ma. These hiatuses were not evident at the resolution of microfossil zones. Conversely, extremely high rates of sediment accumulation are inferred for the interval encompassing the Oligocene/Miocene boundary. Rates of 4.0–10.4 cm/k.y. are recorded between 22 and 24.5 Ma.

A summary of calcareous and siliceous microfossil abundance and preservation is given in Figure F18.

### Calcareous nannofossils

Calcareous nannofossil biostratigraphy is based on analysis of core catcher and additional working section half samples from Holes U1405A and U1405B. Depth positions and age estimates of biostratigraphic marker events are shown in Table T3. Calcareous nannofossil occurrence data are shown in Table T4.

Note that the distribution chart is based on shipboard study only and is, therefore, biased toward age-diagnostic species.

At Site U1405, the preservation of calcareous nannofossils is generally moderate and good but is occasionally poor in carbonate-poor intervals. Preservation is particularly good in pale, carbonate-rich beds around the Oligocene–Miocene transition (Fig. F18), evidenced by the presence of well-preserved spinose sphenoliths and holococcoliths (Fig. F19).

The uppermost sediment in Hole U1405A (Samples 342-U1405A-1H-1, 107 cm, to 1H-CC; 1.07–6.18 mbsf) contains abundant nannofossils indicative of Pleistocene–Pliocene Zones NN19–NN15/NN16 marked by the presence of *Pseudoemiliania lacunosa* (Sample 1H-1, 107 cm; 1.07 mbsf), top of *Discoaster brouweri* (Sample 1H-3, 107 cm; 4.07 mbsf), top of *Discoaster surculus* (Sample 1H-4, 60 cm; 5.10 mbsf), top of *Reticulofenestra pseudoumbilicus* (Sample 342-U1405A-1H-4, 120 cm; 5.70 mbsf), and top of *Amaurolithus* spp. and base of *Ceratolithus rugosus* (Sample 1H-CC; 6.18 mbsf). From Sections 342-U1405B-2H-CC through 3H-CC (11.90–25.72 mbsf), the sediment is noncalcareous and barren of nannofossils.

The interval from Sample 342-U1405A-4H-1, 100 cm, to 33H-CC (26.20–307.14 mbsf) contains frequent to abundant calcareous nannofossils ascribed to lower Miocene–upper Oligocene Zones NN4–NP25 primarily based on the top and base of *Sphenolithus heteromorphus*, top and base of *Sphenolithus bellemnus*, base of *Discoaster druggii*, top of *Sphenolithus delphix*, and top of *Sphenolithus ciperoensis*. The Miocene/Oligocene boundary is approximated by the top of the short-ranging species *S. delphix* and top of *Sphenolithus capricornutus* (Fig. F19). *S. delphix* has a reported longevity of 100 k.y. (see Table T1 in the “Methods” chapter [Norris et al., 2014a]) and is found through a 27 m interval at Site U1405 (Samples 342-U1405A-19H-6, 46 cm, to 22H-4, 110 cm; 175.66–201.80 mbsf).

The Miocene/Oligocene boundary interval also contains at least one carbonate-rich layer with common to abundant *Braarudosphaera* (Fig. F19) and may include thin (1–2 mm), discrete *Braarudosphaera* ooze layers disrupted by bioturbation. Similar layers have been described from the lower Oligocene of the North and South Atlantic Ocean (Parker et al., 1985). *Braarudosphaera* is normally restricted to shelf seas (Bown, 2005), so these range expansions may be caused by unusual paleoceanographic conditions, such as increased upwelling or reconfiguration of circulation that sweeps shelf waters away from the margin (Kelly et al., 2003).

## Radiolarians

Radiolarian biostratigraphy is based on analysis of selected core catcher samples from Hole U1405A. No

samples from Hole U1405B were examined. Radiolarians are absent from the undated upper part of Hole U1405A. They are abundant and well preserved through the lower Miocene and upper Oligocene but are rare and poorly preserved in the lower Oligocene at Site U1405. Depth positions and age estimates of biostratigraphic marker events are shown in Table T5, and the radiolarian distribution is shown in Table T6. Note that the distribution chart is based on shipboard study only and is, therefore, biased toward age-diagnostic species.

Uppermost Sections 342-U1405A-1H-CC through 3H-CC (6.18–25.72 mbsf) are barren or contain only rare and poorly preserved radiolarians.

Radiolarians are abundant and well preserved in Sections 4H-CC through 24H-CC (35.29–224.59 mbsf), and the assemblages can be correlated to lower Miocene–uppermost Oligocene radiolarian Zones RN4–RP22. Diatoms are also common to abundant in most samples examined. Sample 342-U1405A-4H-CC (35.29 mbsf) is correlated with the lower part of Zone RN4 based on the range overlap of *Calocyctella costata* and *Carpocanopsis cingulata*. Sample 6H-CC (54.14 mbsf) is correlated with the lower part of Zone RN3 based on the range overlap of *Stichocorys wolffii* and *Dorcadospyris dentata*. Sections 10H-CC through 12H-CC (92.19–110.85 mbsf) are correlated with Zone RN2 based on the range overlap of *Stichocorys delmontensis* and *Dorcadospyris ateuchus*. The top of *Theocyrtis annosa* is also identified in Sample 12H-CC (110.85 mbsf). Sections 15H-CC through 17H-CC (139.50–158.48 mbsf) are correlated with Zone RN1 based on the co-occurrence of *Cyrtocapsella tetradica* and *Calocyctella virginis* and the absence of *S. delmontensis*. Sections 19H-CC through 24H-CC (177.05–224.59 mbsf) are correlated with Zone RP22 based on the range overlap of *Lychnocanium elongata* and *Artorophormis gracilis*, as well as the absence of *C. tetradica*. Zone RP22 spans the Oligocene/Miocene boundary. Two intrazonal bioevents that have been found to help define the boundary in the low-latitude Pacific (Nigrini et al., 2006; Kamikuri et al., 2012), the base of *Eucyrtidium diaphanes* and the top of *Dorcadospyris papilio*, occur in Sample 22H-CC (206.11 mbsf).

Radiolarians are rare and poorly preserved in the interval 342-U1405A-25H-7, 0–5 cm, through 33X-CC (234.05–307.01 mbsf), and age-diagnostic taxa have not been identified.

## Planktonic foraminifers

Core catchers and additional samples from Hole U1405A working section halves were examined. Samples contained, for the most part, diverse and well-preserved assemblages of planktonic foraminif-



fers except for an interval in the lower Miocene (foraminifer Zones M2–M4), where samples were sporadically barren. Depth positions and age estimates of biostratigraphic marker events identified are shown in Table T7. The stratigraphic distribution of planktonic foraminifers is shown in Table T8 and Figure F18. The substantially improved abundance and preservation of planktonic foraminifers at Site U1405 (4285 mbsl) in comparison to Site U1404 (4747 mbsl) suggests that the mean position of the lysocline may have been located between these two sites throughout the early Miocene and Oligocene.

The uppermost interval from Samples 342-U1405A-1H-1, 105 cm, to 2H-CC (1.06–16.13 mbsf) contains *Globorotalia truncatulinoides*, indicative of Holocene–Pleistocene age sediment. Sections 342-U1405A-4H-1 through 19H-6 (35.26–175.40 mbsf) contain reasonably diverse and well-preserved lower Miocene assemblages containing the marker species *Praeorbulina sicana*, *Globorotalia birnageae*, *Catapsydrax dissimilis*, *Globorotalia praescitula*, *Globoturborotalita angulisutularis*, and *Paragloborotalia kugleri* and *Globoquadrina dehiscens*, indicating a continuous succession at the zonal level from Zone M5/M6 to Subzone M1a. Figure F20 shows a typical lower Miocene assemblage, including the distinctive dentoglobigerinids, and the first appearance of one of these, *G. dehiscens*, marks the Subzone M1a/M1b boundary. Figure F21 illustrates the remarkably good preservation of these lower Miocene planktonic foraminifers, revealing semiglassy taphonomy and even the presence of relict spines within the umbilici.

The base of *P. sicana* indicates Zone M5 in Sample 342-U1405A-5H-6, 110–112 cm (43.31 mbsf). Subzone M4b is marked by the base of *Fohsella birnageae*, which occurs in Sample 342-U1405A-7H-4, 110–112 cm (59.31 mbsf). The tops of *C. dissimilis* and *Catapsydrax unicavus* mark the top of Zone M3 and are observed in Sample 342-U1405A-8H-CC (73.02 mbsf). The base of *G. dehiscens* occurs in Sample 17H-CC (158.48 mbsf). The base of *P. kugleri* (e.g., Fig. F21) marks the Subzone M1a/Zone O7 boundary (22.96 Ma) and is observed in Sample 18H-4, 110–112 cm (163.84 mbsf), marking a position just above the Oligocene/Miocene boundary (23.03 Ma).

Samples 342-U1405A-19H-CC through 30X-CC (177.05–272.73 mbsf) contain few to abundant well-preserved planktonic foraminifers of late Oligocene age. The tops of *Paragloborotalia pseudokugleri* (Sample 26H-4, 5–7 cm) and *Globigerinoides primordius* (Sample 342-U1405A-26H-CC) enabled delineation of upper Oligocene Zones O7 and O6.

Below Sample 342-U1405A-31X-1, 55–55 cm (280.85 mbsf), planktonic foraminifers are rare or absent, preventing zonal demarcation.

## Benthic foraminifers

Benthic foraminifers were examined semiquantitatively in core catcher samples from Hole U1405A and from working section half samples of Cores 342-U1405A-4H through 33X. Additional working section-half samples taken from Cores 1H and 2H were examined for preservation and relative abundance of total benthic foraminifers and individual morpho-groups. Benthic foraminifers at this site are generally rare (the “present” category) relative to total sediment particles >150 µm (Fig. F18). Few samples in Cores 8H through 12H are barren of benthic foraminifers. Assemblages of Cores 4H through 32X are mainly represented by infaunal species, such as *Cassidulina subglobosa*, suggesting high primary production and organic matter flux to the seafloor.

Preservation of foraminifer tests is generally good to very good (Figs. F18, F22). The occurrences of benthic foraminifers at this site are shown in Tables T9 and T10.

Samples 342-U1405A-1H-CC and 2H-CC are dominated by a Pliocene–Pleistocene assemblage of the calcareous taxa *Cibicidoides* spp., *Eponides regularis*, *Laticarinata pauperata*, *Oridorsalis umbonatus*, and *Pullenia* spp. Agglutinated benthic foraminifers, such as *Eggerella bradyi* and *Spiroplectammina* sp., occur frequently.

Although benthic foraminifers occur almost continuously in Cores 342-U1405A-4H through 33X (27.70–301.54 mbsf), their abundance is low (the “present” category) throughout this interval. This lower Miocene to upper Oligocene sequence contains diverse calcareous benthic foraminifer assemblages of good to very good preservation. The assemblages are dominated by *C. subglobosa* and *Stilostomella* spp., including mainly *Stilostomella gracillima*, *Stilostomella lepidula*, and *Stilostomella subspinosa*. Abundant calcareous taxa are typically *Anomalinoides* sp., *Dentalina* sp., *Epistominella umbonifera?*, *Gyroidinoides* sp., *Pullenia bulloides*, *Pullenia quinqueloba*, and pleurostomellids. Agglutinated forms identified include abundant *E. bradyi*, whereas *Bathysiphon* sp. and *Dorothia trochoides* are subordinate.

Among calcareous species, infaunal taxa such as *C. subglobosa*, *Dentalina* sp., *Gyroidinoides* sp., *P. bulloides*, *P. quinqueloba*, and stiliostomellids are notably abundant (Table T9), indicating a high organic matter flux to the seafloor. Abundant diatoms and radiolarians accompany the occurrence of these taxa, which implies high export production to the seafloor.

Benthic foraminifer assemblages at Site U1405 are strikingly similar to those at Site U1404, which is sit-



uated ~300 m deeper on J-Anomaly Ridge. Assemblages at Site U1405, however, lack *Globobulimina pacifica*, which is an indicator species for bottom water dysoxia. *G. pacifica* is common in the lower Miocene to uppermost Oligocene sequence at Site U1404 but occurs only sporadically as single specimens in Samples 342-U1405A-11H-6, 85–87 cm (100.06 mbsf); 14H-6, 70–72 cm (128.44 mbsf); and 18H-6, 86–88 cm (166.62 mbsf). The occurrence of assemblages indicative of high primary productivity and organic matter flux to the seafloor at both Sites U1404 and U1405 suggests a similar paleoenvironment, but with higher bottom water dissolved oxygen concentrations indicated at the shallower Site U1405.

The lowermost samples from Hole U1405A (Samples 33X-4, 92–94 cm, to 33X-CC; 304.63–307.01 mbsf) show significantly lower abundances of infaunal taxa and an increase in epifaunal taxa such as *Anomalina* sp. and *Oridorsalis umbonatus*, suggesting a lower organic matter flux to the seafloor than in the overlying sequence (27.70–301.54 mbsf).

## Paleomagnetism

We completed a paleomagnetic study of APC and XCB cores from Holes U1405A–U1405C with the primary objective of establishing a magnetostratigraphic age model for the site. The natural remanent magnetization (NRM) of each archive half section was measured at 2.5 cm intervals before and after demagnetization treatment in a peak alternating field (AF) of 20 mT for Hole U1405A. For cores from Holes U1405B and U1405C, we only measured NRM after 20 mT demagnetization to compensate for time lost while trouble shooting a problem with the superconducting rock magnetometer (SRM). These problems with the SRM, and their solutions, are detailed below. Archive-half measurement data were processed by removing measurements made within 7.5 cm of section ends and from disturbed intervals described in the Laboratory Information Management System database. Cores 342-U1405A-12H through 26H, 342-U1405B-1H through 24H, and 342-U1405C-1H through 25H were azimuthally oriented using the FlexIT tool (Table T11); all other cores were not oriented.

We also collected 189 discrete samples from working section halves to verify the archive half measurement data and to measure anisotropy of magnetic susceptibility (AMS) and bulk susceptibility of Site U1405 sediment. Discrete samples were collected and stored in 7 cm<sup>3</sup> plastic cubes and typically taken from the least disturbed region closest to the center of each section in Hole U1405A. Selected samples were subjected to AMS measurements, including

bulk susceptibility, and NRM measurements after 20 mT AF demagnetization. Seven samples were further selected for step-wise demagnetization at 10, 20, 30, 40, and 60 mT. All discrete sample data are volume corrected to 7 cm<sup>3</sup>.

## Results

Downhole paleomagnetic data after 20 mT demagnetization are presented for Holes U1405A, U1405B, and U1405C in Figures F23, F24, and F25, respectively. Similar to paleomagnetic results from Sites U1403 and U1404 (see “Paleomagnetism” in the “Site U1403” chapter and “Paleomagnetism” in the “Site U1404” chapter [Norris et al., 2014b, 2014c]), section-half measurement data from XCB cores are difficult to interpret because of biscuiting and substantial core disturbance. Therefore, we chose to interpret only results obtained from APC cores.

We report the following principal features in the paleomagnetic data at Site U1405:

- Magnetic data are noisier in Hole U1405A than in Holes U1405B and U1405C;
- Magnetic intensity and susceptibility decrease significantly over the uppermost ~20–30 mbsf, followed by a gradual decrease downhole; and
- Inclination clusters at ~60° and –45°, associated with a corresponding clustering of declinations of ~0° and 180°, respectively.

## Anomalous y-axis flux jumps and magnetic noise when using the superconducting rock magnetometer

The SRM lost functionality for ~15 h during the initial phases of Hole U1405B data acquisition (1500 h, 28 June to 0600 h, 29 June 2012). Prior to complete loss of functionality, we noticed an increase in the frequency and number of magnetic flux jumps in the y-axis superconducting quantum interference device (SQUID). Initially, one or two flux jumps were recorded by the y-axis SQUID during every few measurement runs following 20 mT demagnetization. Flux jumps always began when the core section first entered the measurement region of the magnetometer from the degausser side of the SRM. The number and frequency of these flux jumps increased rapidly over the next hour, reaching hundreds of jumps per measurement run and while measuring core sections without first using the degausser. We did not observe any flux jumps on the x- and z-axis SQUIDs during any of these measurement runs, indicating that the problem was isolated to the y-axis SQUID. Remanent magnetizations calculated from these data invariably yielded inclination and declination values of 0° and



270°, respectively, and magnetic intensity values that increased linearly downhole in each section half.

Several initial attempts at troubleshooting proved fruitless. These included

- Washing the sample tray and track with anti-static solution,
- Measuring the length of the magnetometer sample track with a fluxgate magnetometer to detect stray high-magnetization material inside the magnetometer,
- Heating the SQUIDs to release any trapped flux,
- Heating the strip line to remove any circulating currents from the pickup coil structure,
- Switching the  $x$  and  $y$  SQUID electronics boxes, and
- Replacing the serial card on the magnetometer PC used to communicate with the SQUID electronic boxes.

During various test runs to isolate the source of the anomalous magnetic flux, we noticed that the problem was isolated to core sections longer than 1 m. Data collected from short (<0.7 m) core sections could be interpreted, although the quality of the data was still poor. These observations, however, led us to discover that an ~1 cm interval of a power cable attached to the in-line degausser was not properly shielded. Most of this cable is shielded with Mu-metal foil to prevent ambient electromagnetic field (EMF) from interfering with the magnetometer. The ~1 cm gap between the shielded degausser and the shielded power cable was covered with aluminum foil, but this foil was connected to the outside of the cable shielding and therefore was not electrically grounded. Moreover, this gap in cable shielding was adjacent to a join in the magnetic shielding assembly around the magnetometer track that is known to leak EMF inside the shielding assembly. We re-wrapped the cable gap with aluminum foil, making sure this foil was electrically connected to the existing shielding material. The number and frequency of  $y$ -axis flux jumps decreased abruptly thereafter. We continued to observe occasional flux jumps, but the typical recurrence interval was 1 flux jump every 30–40 core sections, occurring most frequently after the 20 mT AF demagnetization run. High-quality results could be acquired immediately upon remeasurement.

We attribute the large  $y$ -axis flux jumps to the “antennae” effect, in which wet and typically carbonate-containing core sections longer than ~1–1.25 m channel stray magnetic flux from the core laboratory into the magnetometer sensing region (Fig. F26). The  $y$ -axis SQUID coil configuration is particularly sensitive to induction currents that can be

conducted along the section-half surface. In this particular case during Expedition 342, the antennae effect was amplified by the gap in magnetic shielding of the degausser power cable described above. We suspect that the ungrounded foil that previously covered this gap collected, rather than shielded against, ambient EMF. This collected EMF was then transmitted to the  $y$ -axis coil through the section-half surface by an inducting current. We suspect that stray radio or electromagnetic field was exceptionally high during measurement of Hole U1405B cores because of rough seas and therefore greater use of electric thruster and drilling motors and motion of these motors onboard the R/V *JOIDES Resolution*.

Finally, we note that after properly shielding the gap, the practical background level for SRM measurements improved to  $\sim 1 \times 10^{-5}$  A/m. This is approximately one order of magnitude greater sensitivity than we were achieving prior to arriving at Site U1405. SRM demagnetization data from Hole U1405B and subsequent holes have been remarkably free of noise and reveal a strong square-wave reversal pattern, particularly in the inclination domain.

## Downhole intensity trends

Downhole magnetic intensity and susceptibility values show distinct downhole changes and trends (Figs. F23, F24, F25). Magnetic intensity decreases from  $\sim 10^{-2}$  to  $\sim 10^{-4}$  A/m over the uppermost ~20 m of sediment at Site U1405. From ~20 to ~240 mbsf, intensity continues to decrease, reaching sustained values of  $\sim 10^{-5}$  A/m. A notable exception to this trend is between ~180 and 190 mbsf in all three holes, where intensity increases to  $\sim 10^{-4}$  A/m.

Magnetic susceptibility values also show a sharp decrease from  $\sim 50 \times 10^{-5}$  to  $< 10 \times 10^{-5}$  SI (volume normalized) in the uppermost ~20 m of recovered sediment. Magnetic susceptibility values remain low for the remainder of each Site U1405 core.

These magnetic trends correspond with lithostratigraphy. The uppermost ~20 m of sediment at Site U1405 is composed of yellow to brown Pleistocene-Pliocene foraminiferal nannofossil ooze (lithostratigraphic Subunit Ia) and clay to silty clay (Subunit Ib). The remaining lithostratigraphy is composed of green clay with varying abundances of biosilica, nannofossil ooze, and carbonate (Unit II and division; see “[Lithostratigraphy](#)”). No abrupt changes in sulfate concentration with depth are apparent in Hole U1405A, but manganese shows a pronounced downhole increase beginning at ~20 mbsf (see “[Geochemistry](#)”). These trends suggest that the initial decrease in magnetic intensity and susceptibility values reflect the downward migration of redox fronts in



the upper 2–30 m of sediment. Although lithostratigraphic Unit II is characterized by glauconitic clay, we cannot, at this time, determine if the drop in magnetic intensity is attributable to diagenetic loss of paramagnetic and ferromagnetic material, a change in initial supply of these materials, dilution of these materials by silica and/or carbonate, or a combination of these processes in the Miocene drift deposits.

### Inclination and declination clustering

Inclination values following 20 mT AF demagnetization treatments often cluster around  $60^\circ$  and  $-45^\circ$ . This behavior is especially pronounced for data from Holes U1405B and U1405C. Inclination clustering is usually associated with declination clustering at  $\sim 0^\circ$  and  $180^\circ$ . The approximately  $-45^\circ$  inclination is slightly shallow with respect to the reserved polarity value expected at the  $\sim 40^\circ\text{N}$  latitude of Site U1405. This shallow bias is readily attributed to a small drilling overprint that remains after 20 mT AF demagnetization. We note, however, that 20 mT AF demagnetization treatment is much more effective at removing the drilling overprint than it was with sediment recovered from Sites U1403 and U1404. This may reflect a difference in the remanence characteristics between these sites or a change in SRM sensitivity, as described above. Regardless of the effectiveness of AF treatment between sites, we can utilize the positive and negative polarity-clustering behavior to readily identify magnetozones in recovered intervals at Site U1405.

### Comparison between pass-through and discrete sample data

AF demagnetization results for discrete samples are summarized in Table T12. Of the seven samples treated with peak AF demagnetization field of 60 mT, five reveal relatively stable components of magnetization (e.g., Fig. F27). These samples have remanent magnetizations strong enough to be measured by the onboard JR-6A spinner magnetometer. The remaining samples typically display NRM intensities that decrease by an order of magnitude following AF demagnetization in a 20 mT field. This behavior indicates that the combination of drilling overprint and magnetic-intensity decrease described above has obscured the primary magnetic signal in these stratigraphic intervals, similar to results from Site U1404. Nevertheless, these results are useful for verifying the 20 mT pass-through paleomagnetic data from the archive section halves. In general, paleomagnetic data from archive section halves and discrete samples from oriented core intervals agree well.

Hole U1405A data are noisier than those for Holes U1405B and U1405C, but remanence data from discrete samples provide a straightforward check on the identification of magnetozones (Fig. F23). As detailed previously, we attribute this change in data noise to a change in the sensitivity of the SRM before and after shielding against the antennae effect.

### Magnetostratigraphy

Shipboard downhole magnetostratigraphy results reveal a continuous series of normal and reversed magnetozones between Cores 342-U1405A-5H and 26H ( $\sim 39$ – $242$  mbsf), between Cores 342-U1405B-5H and 24H ( $\sim 39$ – $224$  mbsf), and between Cores 342-U1405C-5H and 24H ( $\sim 37$ – $215$  mbsf). Downhole plots indicate additional series of magnetozones are recorded higher and possibly lower in the recovered section in all three holes, but shore-based studies are necessary to identify and fully characterize magnetozones in these low magnetic intensity intervals and provide preliminary age control to correlate them to the geomagnetic polarity timescale (GPTS). Magnetozones can be straightforwardly correlated between all three holes, especially below  $\sim 90$  mbsf. Although the pattern and stratigraphic thickness of magnetozones in Cores 5H through 8H in all three holes is similar, significant offsets exist between the mbsf depths of these magnetozone boundaries in Hole U1405A and those in Holes U1405B and U1405C.

By utilizing radiolarian, foraminifer, and nannofossil biostratigraphic datums from Hole U1405A (see “[Biostratigraphy](#)”), we can correlate magnetozones to the GPTS. The shipboard magnetostratigraphic age model is based primarily on Hole U1405A, for which we have the most biostratigraphic tie points. Extension of this age model to the magnetozonation observed in Holes U1405B and U1405C is contingent on the accuracy of the stratigraphic correlation between holes, which is corroborated by some lithologic horizons and physical property features (see “[Stratigraphic correlation](#)”). Our correlation is presented in Table T13 and shown in Figures F23, F24, F25, and F28.

In Hole U1405A, we correlated the magnetostratigraphy in Cores 342-U1405A-5H through 8H and 13H through 21H to chron boundaries C5Br/C5Cn.1n (15.974 Ma) through C5Cn.2r/C5Cn.3n (16.543 Ma) and C6Bn.2n/C6Br (22.268 Ma) through C6Cn.3n/C6Cr (23.295 Ma), respectively. Additionally, the identification of nannofossil Zone NN3 in Sections 9H-3 and 9H-4 indicates that the reversed-to-normal downhole polarity transitions observed around this interval correlate to the Chron C5Dr.2r/C5En

(18.056 Ma) and C5Er/C6n (18.748 Ma) boundaries. We note that the series of magnetozones above and below this interval are straightforwardly correlated to a continuous series of chronos on the GPTS, but both of these continuous correlations break down in Cores 8H, 10H, and 11H.

In Hole U1405B, we correlated a series of magnetozone boundaries in Cores 342-U1405B-5H to 9H to chron boundaries C5Br/C5Cn.1n (15.974 Ma) to C5Cn.3n/C5Cr (16.721 Ma). A second series of magnetozone boundaries are correlated to the Chron C6AAr.2n/C6AAr.3r (21.688 Ma) to C6Cn.3n/C6Cr (23.295 Ma) boundaries.

Magnetozone correlations in Hole U1405C are similar to those in Hole U1405B. From Sections 342-U1405C-5H-1 to 9H-6, we correlate magnetozone boundaries to the Chron C5Br/C5Cn.1n (15.974 Ma) to C5Cn.3n/C5Cr (16.721 Ma) boundaries. We did not observe the short reversed Chron C5Cn.1r in Hole U1405C, but we note that, based on the stratigraphic correlation, the interval in which we expected it occurs within the gap between Cores 37H and 8H. Magnetozone boundaries observed in Sections 11H-4 through 21H-7 are continuously correlated to the Chron C6AAr.2n/C6AAr.3r (21.688 Ma) to C6Cn.3n/C6Cr (23.295 Ma) boundaries.

The correlations described above provide a shipboard chronostratigraphic framework for interpreting the latest late Oligocene–middle Miocene sediment drift record at Site U1405. The most salient implications of this age model are summarized here. The Oligocene–Miocene transition is dated by the base of Chron C6Cn.2n (23.030 Ma), which we identified in Sections 342-U1405A-18H-7 through 19H-1, 342-U1405B-18H-3 through 18H-4, and 342-U1405C-17H-6. The shipboard magnetostratigraphic age model also indicates at least two unconformities in Hole U1405A that could be as long as 1.5 or 3.7 m.y. for hiatuses above the Chron C5Dr.2r/C5En boundary and below the Chron C5Er/C6n boundary. Only one hiatus of ~5 m.y. is easily identified between Chrons C5Cr and C6AAr.3r in Holes U1405B and U1405C. These observations suggest highly localized sediment deposition in these sediment drifts. Finally, this age model demonstrates that exceptionally high (~10 cm/k.y.) deep-sea sedimentation rates during the Oligocene–Miocene transition decreased only by a factor of 2–3 (~3.3–5.7 cm/k.y.) over the early Miocene at this site (Fig. F17).

### Magnetic susceptibility and anisotropy of magnetic susceptibility

Bulk magnetic susceptibility measured on 59 discrete samples is summarized in Table T14. Downhole

variation in whole-round magnetic susceptibility (WRMS) and discrete sample magnetic susceptibility (DSMS) for Hole U1405A are shown in Figure F23. The raw WRMS data for Hole U1405A were trimmed at section ends to remove edge effects; obviously spurious data points were also removed. We multiplied the WRMS data, which are in instrument units, by a factor of  $0.577 \times 10^{-5}$  to convert to approximate SI volume susceptibilities (see “Paleomagnetism” in the “Methods” chapter [Norris et al., 2014a]). WRMS and DSMS data agree very well after this conversion, and we attribute small absolute differences to the fact that the conversion factor applied to the WRMS data is not constant downhole because of changes in core diameter and density; only discrete samples provide calibrated susceptibility values in SI units. Both magnetic susceptibility data sets, where they overlap in the uppermost ~80 m of sediment, show the same first- and second-order cyclic trends, indicating that these trends are robust features of Site U1405 sediment. Although discrete samples were collected through the entire depth of Hole U1405A, we chose to cease measurements below ~80 mbsf to compensate for time lost addressing measurement problems with the SRM.

AMS results for the discrete samples are also summarized in Table T14 and are shown in Figure F29. The eigenvalues associated with the maximum ( $\tau_1$ ), intermediate ( $\tau_2$ ), and minimum ( $\tau_3$ ) magnetic susceptibilities at Site U1405 show prominent downhole trends.  $\tau_1$  and  $\tau_3$  are indistinguishable from the top of Hole U1405A to the base of lithostratigraphic Sub-unit Ib (0–17.51 mbsf) (see “Lithostratigraphy”), indicating magnetic anisotropy remains weak over the depth of these upper units. This isotropic fabric is also reflected in low and invariable  $P$  values over this interval. Divergence between  $\tau_1$  and  $\tau_3$  increases substantially and as a step function at the top of Sub-unit IIa (17.51 mbsf) and then remains invariant down-hole to ~82 mbsf, where our shipboard measurements stop. Although the AMS data indicate a strong oblate-shape anisotropy in the upper ~60 m of Sub-unit IIa, the inclination of the minimum eigenvector ( $V_3$ ) does not show a preferred orientation. This indicates that although there is an abundance of oblate paramagnetic (or ferromagnetic) grains in this lithostratigraphic unit, they do not form a strong, depth-dependent magnetic fabric.

### Age-depth model and mass accumulation rates

Coring at Site U1405 recovered a 307 m thick sequence of Pleistocene to upper Oligocene clay, biosi-



liceous nannofossil ooze, and nannofossil ooze. Biostratigraphic and magnetostratigraphic datums from Hole U1405A (Table T15) were compiled to construct an age-depth model for this site (Fig. F17). A selected set of datums (Table T16) was used to create an age-depth correlation and calculate linear sedimentation rates (LSRs). Total mass accumulation rate (MAR), carbonate MAR (CAR), and noncarbonate MAR (nCAR) were calculated at 0.2 m.y. intervals using a preliminary shipboard splice rather than the sampling splice described in this volume (Table T17; Fig. F30).

### Age-depth model

The main objective at Site U1405 was to recover an expanded record of upper Paleogene sediment. An expanded record through the Oligocene–Miocene transition was recovered, comprising a ~100 m thick sediment section with LSRs from 4 to 10 cm/k.y.

The age-depth model is tied to Pleistocene to lower Miocene nannofossil datums in the upper 30 mbsf. Through the lower Miocene and upper Oligocene, a well-integrated suite of biostratigraphic and paleomagnetic datums identifies four hiatuses within the Miocene separated by four intervals of relatively high LSRs from 4 to 6 cm/k.y. Paleomagnetic and nannofossil datums identify a maximum LSR of 10.4 cm/k.y. across the Oligocene/Miocene boundary. Below 190 mbsf, the age model is based on three widely spaced nannofossil datums, which indicate that LSR decreases progressively downhole through the upper Oligocene.

### Linear sedimentation rates

Below the condensed Pleistocene–Miocene interval in the upper 30 mbsf, LSRs in Hole U1405A are relatively high to very high (2–10.4 cm/k.y.) through the lower Miocene and lower Oligocene.

### Mass accumulation rates

MARs at Site U1405 are driven predominantly by noncarbonate components, as indicated by low carbonate contents of generally <40 wt%. A double peak in MAR spans the uppermost Oligocene (4 g/cm<sup>2</sup>/k.y.) to Oligocene/Miocene boundary (6 g/cm<sup>2</sup>/k.y.). These MARs are among the highest encountered during Expedition 342. In the lower Miocene sequence, MAR is ~2 g/cm<sup>2</sup>/k.y.

## Geochemistry

The geochemistry program at Site U1405 included

- Analysis of hydrocarbon gas compounds on headspace samples;

- Measurement of minor and trace element concentrations in interstitial water extracted from whole-round samples; and
- Inorganic carbon, total carbon, and total nitrogen determinations of solid sediment samples.

### Headspace gas samples

Headspace gas samples for routine safety monitoring were collected at a frequency of one sample per core in Hole U1405A (Table T18), usually from the bottom half of each core (i.e., Sections 4, 5, or 6). Methane increases very slightly downhole, with values between 1.59 and 3.49 ppmv. Higher molecular weight hydrocarbons were not detected in measurable amounts.

### Interstitial water samples

Twenty-eight interstitial water samples were collected at a typical frequency of one per core immediately after sectioning the cores on the catwalk. In some cases, cores were too disturbed or recovery was too low to allow a whole-round sample to be taken for analysis. Results of the chemical analyses are presented in Table T19 and Figure F31.

Overall, pH measurements show a gradually decreasing downhole trend at Site U1405, whereas alkalinity measurements show an overall increasing then decreasing trend. Alkalinity reaches maximum values at ~190–210 mbsf with a modest decline downhole thereafter, suggesting that the depth interval centered on ~200 mbsf represents the locus of peak organic matter consumption. This explanation is corroborated by the downhole profile of interstitial water ammonium concentrations, a common respiration product of organic matter consumption. Ammonium concentrations are 0 mM in the upper 20 mbsf of Hole U1405A (corresponding to the Pleistocene–Pliocene clay and nannofossil ooze in lithostratigraphic Subunits Ia and Ib; see “[Lithostratigraphy](#)”) and then increase to peak values around 350 mM at ~210–300 mbsf, near the middle of lithostratigraphic Subunit IIb, an interval composed of silty clay. The decrease in alkalinity at the bottom of the sequence corresponds to a marked transition from biogenic ooze to lithified clay near the middle of Subunit IIc in upper lower Oligocene biosiliceous clay.

Manganese concentrations show a marked increase from seawater values at 5 mbsf to peak values of ~120 µM (210–220 mbsf) and then decrease to 60 µM at the bottom of the hole. Dissolved iron concentrations are low through much of the core but increase to an isolated maximum of 100 µM at 213 mbsf before returning to low values at the base of the section. These profiles suggest sedimentary diagenetic



sis driven by organic matter degradation. The typical sequence of electron acceptor use during early diagenesis is manganese, followed by iron, then sulfate. In Hole U1405A, although there is a modest decreasing trend in sulfate concentrations downhole, the low iron concentrations combined with high manganese concentrations from the top of the sediment column to the top of lithostratigraphic Subunit IIc (Fig. F31) indicates a sedimentary redox sequence that does not progress beyond manganese oxidation until within the lowermost parts of the subunit. This conclusion is corroborated by high sulfate concentrations and a near-linear profile within the locus of peak organic matter consumption (190–210 mbsf) inferred from the alkalinity, ammonium, manganese, and iron profiles. Thus, it is likely that interstitial fluid geochemistry is not driven to sulfate reduction by reactions within the sampled interval (cf. Emerson and Hedges, 2003). Instead, the near-linear, slightly decreasing trend in sulfate may be the result of downward diffusion of sulfate through the Cenozoic sedimentary sequence (e.g., Berner, 1980). The cause of this downward diffusion is unclear. It is possible that an unsampled deeper zone of reduction has superimposed a modest sulfate depletion profile on the entire sampled section.

Potassium interstitial water concentrations decrease from maximum values of 13–16 mM near the top of Hole U1405A in lithostratigraphic Unit I to a minimum value of 6 mM at the bottom of the hole. A prominent inflection to higher values occurs at 190 mbsf and may reflect enhanced sorption onto clay minerals (e.g., Arthur, 1979), particularly illite, which is found in greater abundance in Subunit IIc (see “[Lithostratigraphy](#)”).

The calcium and magnesium profiles in Hole U1405A mimic the overall form of those encountered in deep-sea pelagic settings. The interstitial water profile for calcium in Hole U1405A shows a steady, near-linear increasing trend from ~10 mM at the core top to 28 mM at the base. (Fig. F31). Magnesium concentrations decrease from the core top (53–54 to ~40 mM at ~205 mbsf). Mg/Ca ratios decline steeply from the core top value of ~5 to ~1.5 at depth, with a flattening profile. The Sr profile is markedly different from the classic situation. Instead of the typical increase to a maximum value within the upper 200 m of the sediment column and a concentration plateau to the base of the hole (Gieskes, 1981), the Sr profile at Site U1405 shows a linear increase from the sediment/water interface to the deepest sample analyzed (300 mbsf), suggesting a deep source for Sr. The increase in strontium concentrations is similar to that seen at Sites U1403 and

U1404, suggesting a carbonate-rich neritic section at the base of the site below the drilled section.

Sr/Ca ratios remain nearly constant between 6 and 8, suggesting that carbonate recrystallization and dissolution reactions within the sediment column drilled at Site U1405 (cf. Baker et al., 1982) have a negligible effect on interstitial water calcium concentrations. The variations in Ca, Sr, and Mg concentrations most likely reflect some combination of exchange reactions with the basaltic basement rocks (Gieskes and Lawrence, 1981), formation of authigenic dolomite deposition (e.g., resulting in a reduction in magnesium and increase in calcium), and diffusion. In Figure F32, we plot calcium and magnesium concentrations and Ca/Mg ratio for Sites U1403, U1404, and U1405 with the distance to basement noted. Overall, the calcium, magnesium, and Mg/Ca ratio profiles in Site U1405 interstitial water follow closely with those observed at Site U1404 but differ from the significantly steeper trends observed at Site U1403. These differences may relate to the closer proximity of Site U1403 to basement, which permitted stronger exchange of calcium and magnesium in the Site U1403 interstitial water with the basaltic basement rocks

Collectively, the downhole profiles of interstitial water chemistry in Hole U1405A reflect a combination of diffusion and postdepositional modifications. The modifications include those associated with organic matter degradation, sorption/desorption of chemical components on the surfaces of clay minerals, and chemical exchange with minerals undergoing diagenetic reactions.

## Sediment samples

Sediment plugs (5 cm<sup>3</sup>) for downhole analysis of sediment elemental geochemistry were taken from Cores 342-U1405A-1H to 33X at an average resolution of one sample per section, adjacent to the moisture and density samples (Table T20).

## Results

Carbonate content ranges from 0 to 46 wt% (Fig. F33). Values decline gradually from a maximum of 42 wt% in the uppermost Pliocene–Pleistocene foraminiferal sand to <1 wt% in the uppermost part of lithostratigraphic Subunit Ib. In the upper portion of Subunit IIa, carbonate contents are generally between 0 and 10 wt% and increase to 10–20 wt% in the lower portion of Subunit IIa. Several distinct intervals can be identified in the carbonate record in Hole U1405A:

1. An interval of 0 wt% carbonate within Core 342-U1405A-10H (~80–90 mbsf),



2. Prominent peaks in carbonate content at 60–70 and 110–125 mbsf,
3. Stratigraphically thin intervals of high carbonate content in light-colored intervals around the lithostratigraphic Subunit IIa/IIb and IIb/IIc boundaries (30 and 46 wt%, respectively), and
4. Low carbonate content (<15 wt%) in the lower portion of Subunit IIc.

Elemental analysis of Site U1405 sediment reveals that most of the total carbon in Site U1405 sediment samples is present as calcium carbonate. Total carbon values range from ~0 to ~7 wt%, with the down-hole pattern of total carbon largely resembling that of carbonate content (Fig. F33).

Most of the total organic carbon (TOC) values (i.e., the difference between total carbon and inorganic carbon) are <0.5 wt%, with a smattering of values exceeding 0.6 wt%. Downhole trends in TOC are very subtle, with generally low values (0.1–0.4 wt%) in the upper 150 mbsf, slightly higher values (0.2–0.5 wt%) from 150 to 250 mbsf, and low values (0.1–0.4 wt%) in the lowermost 60 m of Hole U1405A. Most of the total nitrogen values fall into the 0.1–0.2 wt% range, with some higher values (i.e., >0.2 wt%) in the upper 110 m of Hole U1405A (Table T20; Fig. F33).

## Discussion

Based on the shipboard biostratigraphic- and paleomagnetic-derived age model for Site U1405 (see “[Biostratigraphy](#)”), the intervals of high calcium carbonate contents in Subunit IIa correspond with intervals of elevated carbonate content observed in the lowermost Miocene and upper Oligocene at Site U1404. These intervals of increased carbonate content in the uppermost Oligocene appear to be driven by calcareous nannofossil abundance, particularly the shelf taxon *Braarudosphaera* (see “[Biostratigraphy](#)”), which is absent in any other interval. Collectively, these conspicuous fluctuations of carbonate content possibly reflect the result of CCD fluctuations, carbonate production, and/or sea level. Regardless of the cause, the occurrence of multiple intervals with similar characteristics during the Oligocene–Miocene transition suggest repeated oceanographic changes over an extended stratigraphic interval (e.g., >70 m of sediment) at Site U1405.

## Physical properties

We made physical properties measurements on whole-round sections, section halves, and discrete samples from section halves. Gamma ray attenuation (GRA) bulk density, magnetic susceptibility, *P*-

wave velocity, and natural gamma radiation (NGR) measurements were made on whole-round sections using the Whole-Round Multisensor Logger (WRMSL) and NGR logger. Thermal conductivity measurements could not be performed at Site U1405 because of technical problems. Compressional wave velocity on section halves was also measured at a frequency of two in each section (at ~50 and 100 cm) using a *P*-wave caliper (PWC). For moisture and density (MAD) analyses, one discrete sample was collected in each section (typically at ~35 cm from the top of a section). The Section Half Multisensor Logger (SHMSL) was used to measure spectral reflectance and magnetic susceptibility on archive section halves.

### Magnetic susceptibility

From the top of the sediment column at Site U1405 to ~18 mbsf (lithostratigraphic Unit I), magnetic susceptibility first increases downhole from 50 to 100 instrument units (IU) and then decreases to ~5 IU at the top of Subunit Ib (Fig. F34). This decrease is associated with a decrease in carbonate content at 10 mbsf (see “[Geochemistry](#)”). Below, Unit II is largely composed of a uniform sequence of greenish gray biosiliceous ooze and clay, and magnetic susceptibility remains very low, averaging 5 IU in all three holes. A small peak to ~25 IU occurs in Holes U1405B and U1405C at ~80 mbsf and is associated with increased color reflectance a\*.

### Density and porosity

Bulk density, water content, porosity, and grain density measurements were obtained from 194 discrete samples using the MAD method. Bulk density was also determined using the GRA method on the whole-round sections. Changes in MAD bulk density are consistent with those in the GRA bulk density (Fig. F34). MAD values are ~2% lower than GRA density values throughout the section. The most striking feature in the density profile is the significantly higher values in lithostratigraphic Unit I than in Unit II. The average bulk density is 1.57 g/cm<sup>3</sup> in Subunit Ia of Holes U1405B and U1405C, increasing from 1.4 g/cm<sup>3</sup> at the top of the hole to 1.7 g/cm<sup>3</sup> at ~3 mbsf in Hole U1405A. Subunit Ib is characterized by a decrease from ~1.6 to ~1.3 g/cm<sup>3</sup> in all three holes. Bulk density values show a peak at ~4 mbsf in Holes U1405B and U1405C that is not seen in Hole U1405A.

In Unit II, bulk density shows a typical downhole increase from ~1.3 to 1.5 g/cm<sup>3</sup> caused by compaction, with several superimposed small peaks and shifts. In Hole U1405A, notable peaks are found at 68, 220,



and 238 mbsf. Broadly correlative peaks in bulk density are recorded at 78, 140, 178, and 220 mbsf in Hole U1405B and at 78, 135, 163, and 218 mbsf in Hole U1405C.

Water content and porosity increase downhole in Unit I from 40 to 70 wt% and from 65 to 87 vol%, respectively, with a distinctive shift at the contact between Units I and Unit II. Throughout Unit II, both of these parameters decrease gradually (to 40 wt% for water content and to 67 vol% for porosity) to the bottom of Hole U1405A. Some superimposed shifts appear at 70, 100, and 180 mbsf, and some of these are likely to be associated with stratigraphic hiatuses. Notable decreases in these physical properties occur (water content shifts from ~60 to 40 wt% and porosity from 75 to 63 vol%) at ~270 mbsf, but the link to lithology cannot be established because of the poor recovery below 250 mbsf in Hole U1405A.

Grain density generally varies between 2.6 and 2.8 g/cm<sup>3</sup> throughout Hole U1405A with the exception of one data point at ~70 mbsf that shows a specific density of 2.9 g/cm<sup>3</sup> and two data points that show values <2.5 g/cm<sup>3</sup> at ~218 mbsf.

### P-wave velocity

*P*-wave velocity from whole-round sections and section halves track each other well, with an average offset of ~15 m/s (Fig. F35). Overall, *P*-wave velocity gradually increases downhole in each of the three holes. Between the top of the sediment column and ~230 mbsf, *P*-wave velocity increases from 1500 to 1600 m/s and reaches 1650 m/s in the lower part of lithostratigraphic Subunit IIc of Hole U1405A (230–308 mbsf). In Hole U1405A, *P*-wave velocity measurements are slightly higher in Unit I than the upper part of Unit II. *P*-wave velocity shows a down-hole compaction trend similar to bulk density and water content.

### Natural gamma radiation

In all three holes from the top of the sediment column to ~25 mbsf (lithostratigraphic Unit I), NGR values range from 15 to 30 cps (Fig. F35). In Unit II, NGR values fluctuate from 15 to 25 cps and are on average lower than those in Unit I. Notable peaks are observed in all three holes. A peak of ~25 cps is seen at ~82 mbsf in Holes U1405B and U1405C and may be associated with the small peak at ~70 mbsf in Hole U1405A. However, other peaks cannot be traced between holes (see “Stratigraphic correlation”). For example, in Hole U1405B the 30 cps peak at 140 mbsf has no equivalents in Holes U1405A and U1405C. Physical property variations such as these likely reflect changes in sediment composition that

do not extend across all holes, which could reflect sedimentation changes associated with drift deposits.

### Color reflectance

Reflectance parameters were measured on archive section halves in Holes U1405A–U1405C. For Hole U1405C, the resolution was decreased from 2.5 to 5 cm in order to finish processing all cores from Hole U1405C before arriving at the next site.

Color reflectance parameters *a*\* and *b*\* follow similar trends to one another and characterize lithostratigraphic Units I and II in the three holes (Fig. F36). Within each lithostratigraphic unit, both *a*\* and *b*\* remain relatively constant, and at the unit boundary they drop dramatically. In Unit I, the values fluctuate from 0 to 6 for *a*\* and from 5 to 15 for *b*\*. In Unit II, *a*\* varies between -4 and 0 and *b*\* varies between -2 and 4. The positive values of *a*\* and *b*\* in Unit I correspond to yellow, brown, and gray sediment. The lower values in Unit II indicate higher blue and green content and reflect relatively homogeneous greenish gray sediment (see “Lithostratigraphy”).

In Unit II, *a*\* increases slightly downhole. Slightly more distinct variations occur at ~70–80 mbsf in Holes U1405A–U1405C, which correspond to features in the magnetic susceptibility and NGR data series at those depths (Fig. F35).

*L*\* corresponds to sediment brightness and generally follows pronounced lithologic changes (Fig. F36). In Unit I, the average *L*\* is 52 in all three holes. Unit II is characterized by slightly lower *L*\* values that vary between 40 and 55. In Hole U1405A, *L*\* fluctuates downhole between 40 and 60 from the top of the hole to ~210 mbsf. More than any other physical property, *L*\* profiles show somewhat different patterns, or noise distributions, in Holes U1405A–U1405C. The variations in *L*\* recorded at Site U1405 probably reflect changes in calcium carbonate content.

## Stratigraphic correlation

### Sampling splice

Achieving an accurate splice using shipboard data at Site U1405 was challenging because of weak signals in the physical property data throughout most of the sediment column. As a result, we conducted extensive postcruise X-ray fluorescence (XRF) core scanning of the archive halves of sections from 39.9 to 300.84 m core composite depth below seafloor (CCSF) using the Avaatech XRF core scanner at Texas A&M University (USA). The sampling splice is based primarily on the ratio of iron to calcium in this inter-



val (Fig. F37), with other elemental data used as necessary to select tie points. For the remainder of the correlation and splice construction (0–39.9 and 300.93–366.01 m CCSF), we relied on shipboard physical property data (Fig. F38). The correlation between Holes U1405B and U1405C is more reliable than either hole's correlation with Hole U1405A. In order to account for clear hiatuses in all three holes, we inserted some very large gaps (>10 m). Hole U1405A is the deepest hole drilled, with a maximum depth of ~299 mbsf; Hole U1405B extends to ~214 mbsf and Hole U1405C to ~223 mbsf. Our correlation yields a growth rate of 27% for Hole U1405A, 28% for Hole U1405B, and 29% for Hole U1405C (Fig. F39), which represents the average increase of the CCSF depth scale relative to each hole's mbsf depth scale. The affine table (Table T21) summarizes the individual offsets for each core drilled.

### Correlation during drilling operations

We attempted real-time correlation between Holes U1405A, U1405B, and U1405C using magnetic susceptibility and GRA bulk density data collected at 2.5 cm resolution on the Special Task Multisensor Logger (STMSL) before allowing cores to equilibrate to room temperature; however, the quickly generated records were inadequate for guiding drilling operations because the magnetic susceptibility signal rarely exceeded the noise level (<15 IU) below ~20 mbsf. Based on our experience with similar lithologies at Site U1404, we were skeptical of relying on GRA bulk density data alone for real-time correlation, particularly because the density of individual cores may be altered during drilling and curation. A clear color change in Cores 342-U1405A-3H and 342-U1405B-3H allowed us to obtain an initial offset in coring gaps by directing drilling operations to advance ~5 m without recovery (Core 342-U1405B-41) before shooting Core 342-U1405B-5H. This was the only adjustment to drilling operations made while drilling Holes U1405B and U1405C. Using the range of *S. delphix* (see “**Biostratigraphy**”) and GRA density data, we were able to verify complete stratigraphic coverage of the Oligocene–Miocene transition between Cores 342-U1405A-20H and 342-U1405B-20H. A final complication for real-time correlation was large ship heave during Tropical Storm Debbie, which may have contributed to apparently large coring gaps.

### Correlation and splice construction

For stratigraphic correlation and splice construction, we primarily used XRF core scanner Fe/Ca measurements, which showed significantly clearer features

than shipboard physical properties (see “**Physical properties**”). We assessed additional XRF elemental data as needed. Core photographs did not aid correlation because of the homogeneity of the recovered sediment.

Measured from the individual mudlines, the change from Pleistocene to Miocene sediment (from lithostratigraphic Unit I to II; see “**Lithostratigraphy**”) in Cores 342-U1405A-3H, 342-U1405B-3H, and 342-U1405C-2H is present at ~18, ~21, and ~14 mbsf, respectively. The large variation in the thickness of Unit I between holes probably indicates the presence of dunelike features (mudwaves or sandwaves) in the Pleistocene surface sediment. Correlation between Holes U1405B and U1405C was more straightforward than for Hole U1405A. The two clearest tie points (the Pleistocene–Miocene hiatus and the Miocene–Oligocene transition) constrained the correlation of Hole U1405A to the other holes above ~50 m CCSF and below ~150 m CCSF. Between these depths, the stratigraphy was complicated by hiatuses in Cores 342-U1405A-7H and 20H, 342-U1405B-16H, and 342-U1405C-16H. These hiatuses complicate straightforward correlation because they are present at different stratigraphic levels in each hole. To enable correlation of the same stratigraphic intervals present in the three holes despite these hiatuses, we apply gaps in the affine table. First, in Hole U1405A we insert a 13 m gap at ~80 m CCSF and a 10.7 m gap at ~233 m CCSF. The offsets applied to account for hiatuses in Holes U1405B and U1405C are 17.5 m at ~182 m CCSF and 25.5 m at 192 m CCSF, respectively. These large offsets have a significant influence on the mbsf-to-CCSF growth rate, which is ~28% (Fig. F39). Therefore, the growth rate no longer reflects sediment expansion and differences between the advance of the drill string and curated core length alone but reflects the difference in the stratigraphy present among the three holes. Our resulting composite depth scale and splice agrees with most paleomagnetism, biostratigraphy, and physical property data (Fig. F40). However, a number of tie points and depth offsets are tentative (Tables T21, T22), especially where only physical property data are available.

## References

- Arthur, M.A., 1979. Origin of Upper Cretaceous multicolored claystones of the Western Atlantic. In Tucholke, B.E., Vogt, P.R., et al., *Init. Repts. DSDP*, 43: Washington, DC (U.S. Govt. Printing Office), 417–420. doi:10.2973/dsdp.proc.43.111.1979
- Baker, P.A., Gieskes, J.M., and Elderfield, H., 1982. Diagenesis of carbonates in deep-sea sediments: evidence from



- Sr/Ca ratios and interstitial dissolved Sr<sup>2+</sup> data. *J. Sediment. Res.*, 52(1):71–82. doi:[10.1306/212F7EE1-2B24-11D7-8648000102C1865D](https://doi.org/10.1306/212F7EE1-2B24-11D7-8648000102C1865D)
- Berner, R.A., 1980. *Early Diagenesis: A Theoretical Approach*: Princeton, NJ (Princeton Univ. Press).
- Bown, P.R., 2005. Cenozoic calcareous nannofossil biostratigraphy, ODP Leg 198 Site 1208 (Shatsky Rise, northwest Pacific Ocean). In Bralower, T.J., Premoli Silva, I., and Malone, M.J. (Eds.), *Proc. ODP, Sci. Results*, 198: College Station, TX (Ocean Drilling Program), 1–44. doi:[10.2973/odp.proc.sr.198.104.2005](https://doi.org/10.2973/odp.proc.sr.198.104.2005)
- Coxall, H.K., Wilson, P.A., Pälike, H., Lear, C.H., and Backman, J., 2005. Rapid stepwise onset of Antarctic glaciation and deeper calcite compensation in the Pacific Ocean. *Nature (London, U. K.)*, 433(7021):53–57. doi:[10.1038/nature03135](https://doi.org/10.1038/nature03135)
- Channell, J.E.T., Sato, T., Kanamatsu, T., Stein, R., and Alvarez Zarikian, C., 2010. Expedition 303/306 synthesis: North Atlantic climate. In Channell, J.E.T., Kanamatsu, T., Sato, T., Stein, R., Alvarez Zarikian, C.A., Malone, M.J., and the Expedition 303/306 Scientists, *Proc. IODP, 303/306: College Station, TX (Integrated Ocean Drilling Program Management International, Inc.)*. doi:[10.2204/iodp.proc.303306.214.2010](https://doi.org/10.2204/iodp.proc.303306.214.2010)
- DeConto, R.M., Pollard, D., Wilson, P.A., Pälike, H., Lear, C.H., and Pagani, M., 2008. Thresholds for Cenozoic bipolar glaciation. *Nature (London, U. K.)*, 455(7213):652–656. doi:[10.1038/nature07337](https://doi.org/10.1038/nature07337)
- Edgar, K.M., Wilson, P.A., Sexton, P.F., and Suganuma, Y., 2007. No extreme bipolar glaciation during the main Eocene calcite compensation shift. *Nature (London, U. K.)*, 448(7156):908–911. doi:[10.1038/nature06053](https://doi.org/10.1038/nature06053)
- Eldrett, J.S., Harding, I.C., Wilson, P.A., Butler, E., and Roberts, A.P., 2007. Continental ice in Greenland during the Eocene and Oligocene. *Nature (London, U. K.)*, 446(7132):176–179. doi:[10.1038/nature05591](https://doi.org/10.1038/nature05591)
- Emerson, S., and Hedges, J.I., 1988. Processes controlling the organic carbon content of open ocean sediments. *Paleoceanography*, 3(5):621–634. doi:[10.1029/PA003i005p00621](https://doi.org/10.1029/PA003i005p00621)
- Gieskes, J.M., 1981. Deep-sea drilling interstitial water studies: implications for chemical alteration of the oceanic crust, Layers I and II. In Warmer, J.E., Douglas, R.G., and Winterer, E.L. (Eds.), *The Deep Sea Drilling Project: A Decade of Progress*. Spec. Publ.—Soc. Econ. Paleontol. Mineral., 32:149–167.
- Gieskes, J.M., and Lawrence, J.R., 1981. Alteration of volcanic matter in deep-sea sediments: evidence from the chemical composition of interstitial waters from deep sea drilling cores. *Geochim. Cosmochim. Acta*, 45(10):1687–1703. doi:[10.1016/0016-7037\(81\)90004-1](https://doi.org/10.1016/0016-7037(81)90004-1)
- Gradstein, F.M., Ogg, J.G., Schmitz, M.D., and Ogg, G.M. (Eds.), 2012. *The Geological Time Scale 2012*: Amsterdam (Elsevier).
- Holbourn, A., Kuhnt, W., Schulz, M., and Erlenkeuser, H., 2005. Impacts of orbital forcing and atmospheric carbon dioxide on Miocene ice-sheet expansion. *Nature (London, U. K.)*, 438(7067):483–487. doi:[10.1038/nature04123](https://doi.org/10.1038/nature04123)
- Kamikuri, S., Moore, T.C., Ogane, K., Suzuki, N., Pälike, H., and Nishi, H., 2012. Early Eocene to early Miocene radiolarian biostratigraphy for the low-latitude Pacific Ocean. *Stratigraphy*, 9(1):77–108. [http://www.micropress.org/micropen2/articles/1/7/27546\\_articles\\_article\\_file\\_1785.pdf](http://www.micropress.org/micropen2/articles/1/7/27546_articles_article_file_1785.pdf)
- Kelly, D.C., Norris, R.D., and Zachos, J.C., 2003. Deciphering the paleoceanographic significance of early Oligocene *Braarudosphaera* chalks in the South Atlantic. *Mar. Micropaleontol.*, 43(1–2):49–63. doi:[10.1016/S0377-8398\(03\)00027-6](https://doi.org/10.1016/S0377-8398(03)00027-6)
- Kirschvink, J.L., 1980. The least-squares line and plane and the analysis of palaeomagnetic data. *Geophys. J. R. Astron. Soc.*, 62(3):699–718. doi:[10.1111/j.1365-246X.1980.tb02601.x](https://doi.org/10.1111/j.1365-246X.1980.tb02601.x)
- Liebrand, D., Lourens, L.J., Hodell, D.A., de Boer, B., van de Wal, R.S.W., and Pälike, H., 2011. Antarctic ice sheet and oceanographic response to eccentricity forcing during the early Miocene. *Clim. Past*, 7(3):869–880. doi:[10.5194/cp-7-869-2011](https://doi.org/10.5194/cp-7-869-2011)
- Lyle, M., Wilson, P.A., Janecek, T.R., et al., 2002. *Proc. ODP, Init. Repts.*, 199: College Station, TX (Ocean Drilling Program). doi:[10.2973/odp.proc.ir.199.2002](https://doi.org/10.2973/odp.proc.ir.199.2002)
- Mericco, A., Tyrrell, T., and Wilson, P.A., 2008. Eocene/Oligocene ocean de-acidification linked to Antarctic glaciation by sea-level fall. *Nature (London, U. K.)*, 452(7190):979–982. doi:[10.1038/nature06853](https://doi.org/10.1038/nature06853)
- Miller, K.G., Wright, J.D., Katz, M.E., Browning, J.V., Cramer, B.S., Wade, B.S., and Mizintseva, S.F., in press. A view of Antarctic ice sheet evolution from sea level and deep-sea isotope changes during the Late Cretaceous–Cenozoic. In Cooper, A., Raymond, C., and the ISAES Editorial Team (Eds.), *Antarctica: A Keystone in a Changing World—Online Proceedings for the Tenth International Symposium on Antarctic Earth Sciences*. USGS Open-File Rep., 2007–1047.
- Nigrini, C., Sanfilippo, A., and Moore, T.C., Jr., 2006. Cenozoic radiolarian biostratigraphy: a magnetobiostratigraphic chronology of Cenozoic sequences from ODP Sites 1218, 1219, and 1220, equatorial Pacific. In Wilson, P.A., Lyle, M., and Firth, J.V. (Eds.), *Proc. ODP, Sci. Results*, 199: College Station, TX (Ocean Drilling Program), 1–76. doi:[10.2973/odp.proc.sr.199.225.2006](https://doi.org/10.2973/odp.proc.sr.199.225.2006)
- Norris, R.D., Wilson, P.A., Blum, P., Fehr, A., Agnini, C., Bornemann, A., Boulila, S., Bown, P.R., Courneude, C., Friedrich, O., Ghosh, A.K., Hollis, C.J., Hull, P.M., Jo, K., Junium, C.K., Kaneko, M., Liebrand, D., Lippert, P.C., Liu, Z., Matsui, H., Moriya, K., Nishi, H., Opdyke, B.N., Penman, D., Romans, B., Scher, H.D., Sexton, P., Takagi, H., Turner, S.K., Whiteside, J.H., Yamaguchi, T., and Yamamoto, Y., 2014a. Methods. In Norris, R.D., Wilson, P.A., Blum, P., and the Expedition 342 Scientists, *Proc. IODP, 342: College Station, TX (Integrated Ocean Drilling Program)*. doi:[10.2204/iodp.proc.342.102.2014](https://doi.org/10.2204/iodp.proc.342.102.2014)
- Norris, R.D., Wilson, P.A., Blum, P., Fehr, A., Agnini, C., Bornemann, A., Boulila, S., Bown, P.R., Courneude, C., Friedrich, O., Ghosh, A.K., Hollis, C.J., Hull, P.M., Jo, K., Junium, C.K., Kaneko, M., Liebrand, D., Lippert, P.C., Liu, Z., Matsui, H., Moriya, K., Nishi, H., Opdyke, B.N., Penman, D., Romans, B., Scher, H.D., Sexton, P., Takagi,



- H., Turner, S.K., Whiteside, J.H., Yamaguchi, T., and Yamamoto, Y., 2014b. Site U1403. In Norris, R.D., Wilson, P.A., Blum, P., and the Expedition 342 Scientists, *Proc. IODP*, 342: College Station, TX (Integrated Ocean Drilling Program). [doi:10.2204/iodp.proc.342.104.2014](https://doi.org/10.2204/iodp.proc.342.104.2014)
- Norris, R.D., Wilson, P.A., Blum, P., Fehr, A., Agnini, C., Bornemann, A., Boulila, S., Bown, P.R., Courneude, C., Friedrich, O., Ghosh, A.K., Hollis, C.J., Hull, P.M., Jo, K., Junium, C.K., Kaneko, M., Liebrand, D., Lippert, P.C., Liu, Z., Matsui, H., Moriya, K., Nishi, H., Opdyke, B.N., Penman, D., Romans, B., Scher, H.D., Sexton, P., Takagi, H., Turner, S.K., Whiteside, J.H., Yamaguchi, T., and Yamamoto, Y., 2014c. Site U1404. In Norris, R.D., Wilson, P.A., Blum, P., and the Expedition 342 Scientists, *Proc. IODP*, 342: College Station, TX (Integrated Ocean Drilling Program). [doi:10.2204/iodp.proc.342.105.2014](https://doi.org/10.2204/iodp.proc.342.105.2014)
- Oda, H., and Shibuya, H., 1996. Deconvolution of long-core paleomagnetic data of Ocean Drilling Program by Akaike's Bayesian Information Criterion minimization. *J. Geophys. Res.: Solid Earth*, 101(B2):2815–2834. [doi:10.1029/95JB02811](https://doi.org/10.1029/95JB02811)
- Pälike, H., Lyle, M.W., Nishi, H., Raffi, I., Ridgwell, A., Gamage, K., Klaus, A., Acton, G., Anderson, L., Backman, J., Baldauf, J., Beltran, C., Bohaty, S.M., Bown, P., Busch, W., Channell, J.E.T., Chun, C.O.J., Delaney, M., Dewangan, P., Dunkley Jones, T., Edgar, K.M., Evans, H., Fitch, P., Foster, G.L., Gussone, N., Hasegawa, H., Hathorne, E.C., Hayashi, H., Herrle, J.O., Holbourn, A., Hovan, S., Hyeong, K., Iijima, K., Ito, T., Kamikuri, S., Kimoto, K., Kuroda, J., Leon-Rodriguez, L., Malinverno, A., Moore, T.C., Jr., Murphy, B.H., Murphy, D.P., Nakamura, H., Ogane, K., Ohneiser, C., Richter, C., Robinson, R., Rohling, E.J., Romero, O., Sawada, K., Scher, H., Schneider, L., Sluijs, A., Takata, H., Tian, J., Tsujimoto, A., Wade, B.S., Westerhold, T., Wilkens, R., Williams, T., Wilson, P.A., Yamamoto, Y., Yamamoto, S., Yamazaki, T., and Zeebe, R.E., 2012. A Cenozoic record of the equatorial Pacific carbonate compensation depth. *Nature (London, U.K.)*, 488(7409):609–614. [doi:10.1038/nature11360](https://doi.org/10.1038/nature11360)
- Pälike, H., Norris, R.D., Herrle, J.O., Wilson, P.A., Coxall, H.K., Lear, C.H., Shackleton, N.J., Tripati, A.K., and Wade, B.S., 2006. The heartbeat of the Oligocene climate system. *Science*, 314(5807):1894–1898. [doi:10.1126/science.1133822](https://doi.org/10.1126/science.1133822)
- Parker, M.E., Clark, M., and Wise, S.W., Jr., 1985. Calcareous nannofossils of Deep Sea Drilling Project Sites 558 and 563, North Atlantic Ocean: biostratigraphy and the distribution of Oligocene braarudosphaerids. In Bougault, H., Cande, S.C., et al., *Init. Repts. DSDP*, 82: Washington, DC (U.S. Govt. Printing Office), 559–589. [doi:10.2973/dsdp.proc.82.134.1985](https://doi.org/10.2973/dsdp.proc.82.134.1985)
- Stickley, C.E., St. John, K., Koç, N., Jordan, R.W., Passchier, S., Pearce, R.B., and Kearns, L.E., 2009. Evidence for middle Eocene Arctic sea ice from diatoms and ice rafted debris. *Nature (London, U.K.)*, 460(7253):376–379. [doi:10.1038/nature08163](https://doi.org/10.1038/nature08163)
- Tripati, A., Backman, J., Elderfield, H., and Ferretti, P., 2005. Eocene bipolar glaciation associated with global carbon cycle changes. *Nature (London, U.K.)*, 436(7049):341–346. [doi:10.1038/nature03874](https://doi.org/10.1038/nature03874)
- Tripati, A.K., Eagle, R.A., Morton, A., Dowdeswell, J.A., Atkinson, K.L., Bahé, Y., Dawber, C.F., Khadun, E., Shaw, R.M.H., Shorttle, O., and Thanabalan Sundaram, L., 2008. Evidence for glaciation in the Northern Hemisphere back to 44 Ma from ice-raftered debris in the Greenland Sea. *Earth Planet. Sci. Lett.*, 265(1–2):112–122. [doi:10.1016/j.epsl.2007.09.045](https://doi.org/10.1016/j.epsl.2007.09.045)
- Tucholke, B.E., and Vogt, P.R., 1979. Western North Atlantic: sedimentary evolution and aspects of tectonic history. In Tucholke, B.E., Vogt, P.R., et al., *Init. Repts. DSDP*, 43: Washington, DC (U.S. Govt. Printing Office), 791–825. [doi:10.2973/dsdp.proc.43.140.1979](https://doi.org/10.2973/dsdp.proc.43.140.1979)
- Zachos, J.C., Flower, B.P., and Paul, H., 1997. Orbitally paced climate oscillations across the Oligocene/Miocene boundary. *Nature (London, U.K.)*, 388(6642):567–570. [doi:10.1038/41528](https://doi.org/10.1038/41528)

Publication: 3 March 2014  
MS 342-106



**Figure F1.** Bathymetric map of the southwestern end of J-Anomaly Ridge and location of Site U1405 (red star). Track lines are from a single-channel seismic survey conducted during the KNR179-1 site survey. See Figures F2, F3, and F4 for seismic profiles.

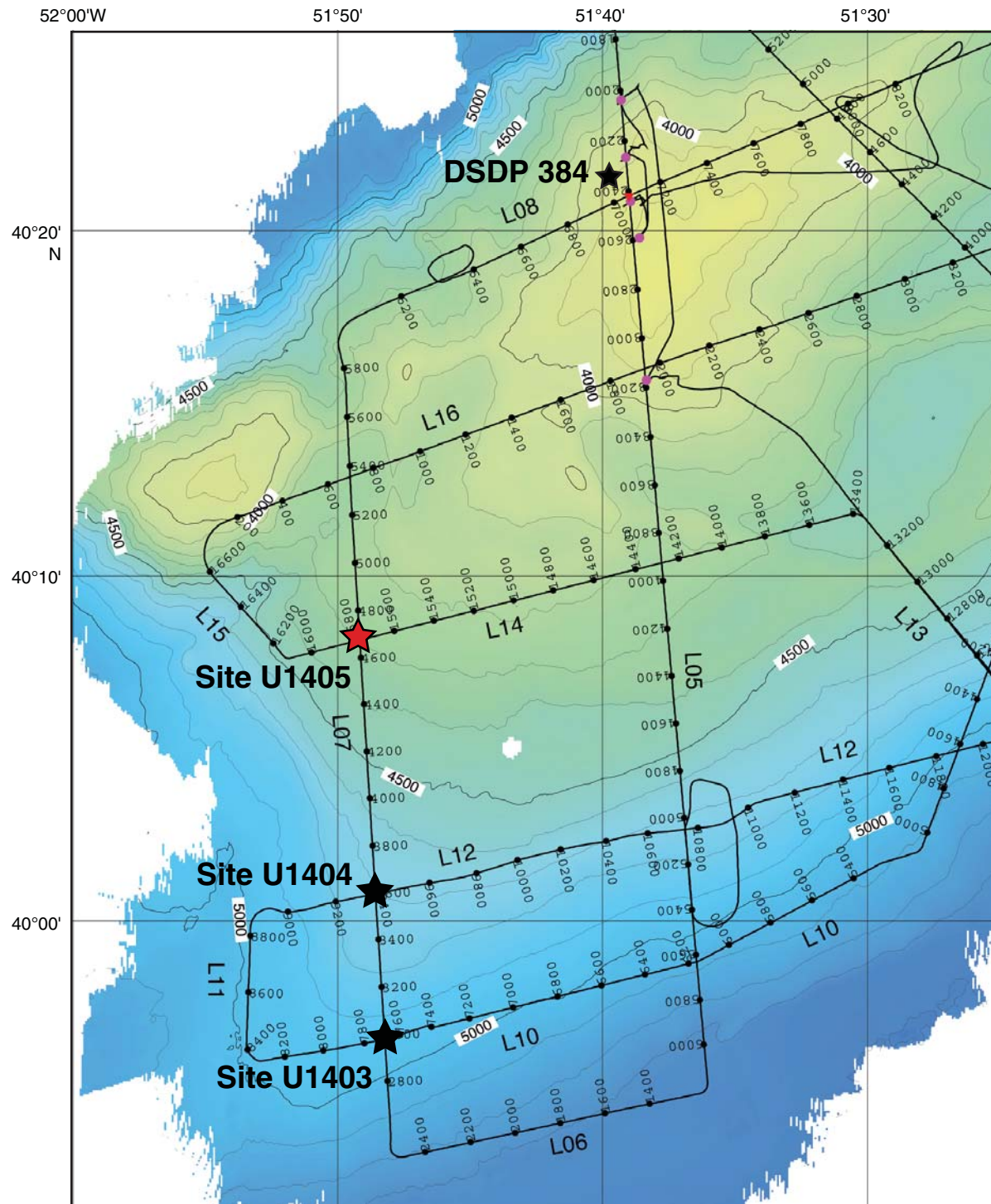


**Figure F2.** Single-channel seismic line KNR179-1 Line 7. This is the north–south dip line crossing Site U1405 (at shotpoint [SP] 4650). White bar represents the approximate depth of penetration.

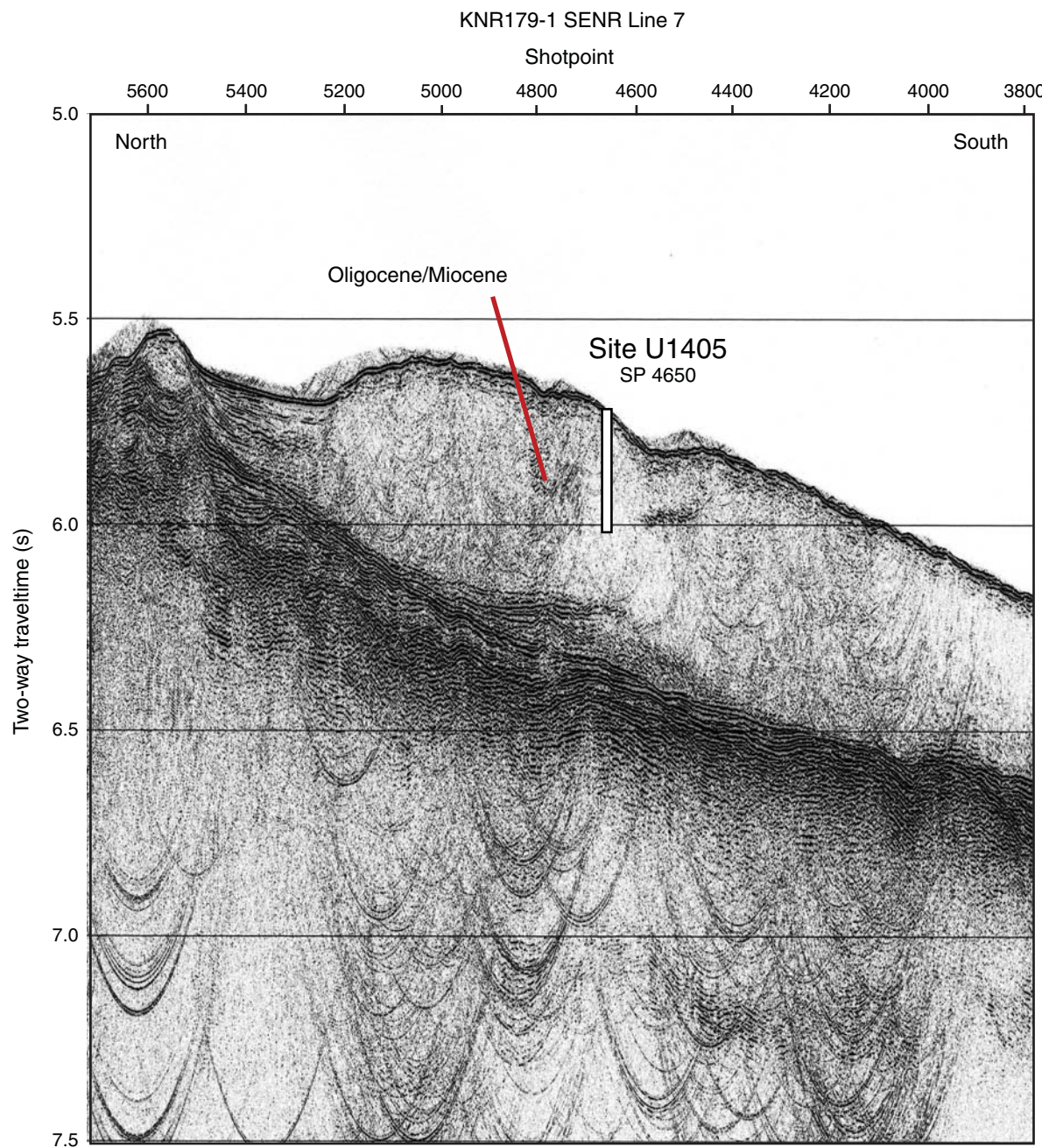


**Figure F3.** Single-channel seismic KNR179-1 Line 14. This is the northeast–southwest strike line crossing Site U1405 (at shotpoint [SP] 15790). White bar represents the approximate depth of penetration.

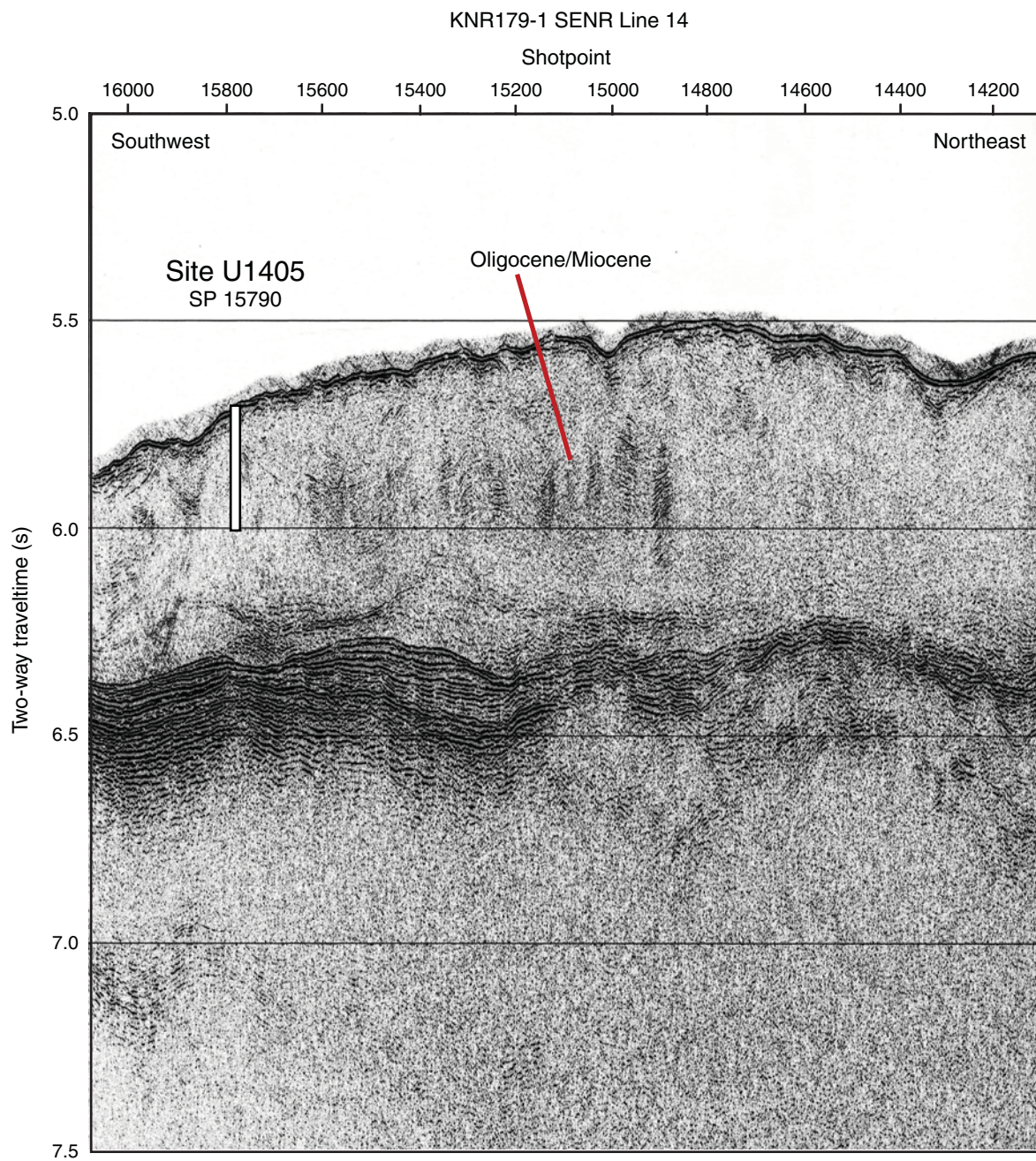


**Figure F4.** Single-channel seismic KNR179-1 Line 7. North–south dip line crosses Sites U1403–U1405. Note the upslope thickening of the acoustically uniform sediment package drilled at these sites. White bars represent the approximate depths of penetration.

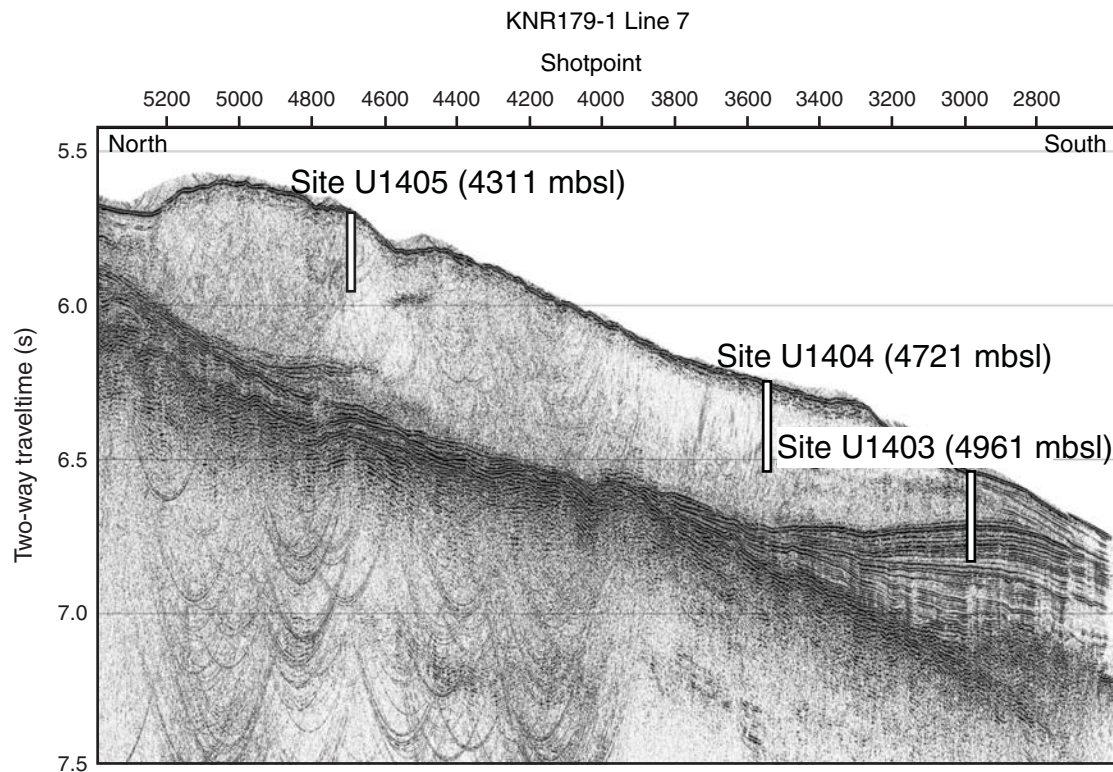
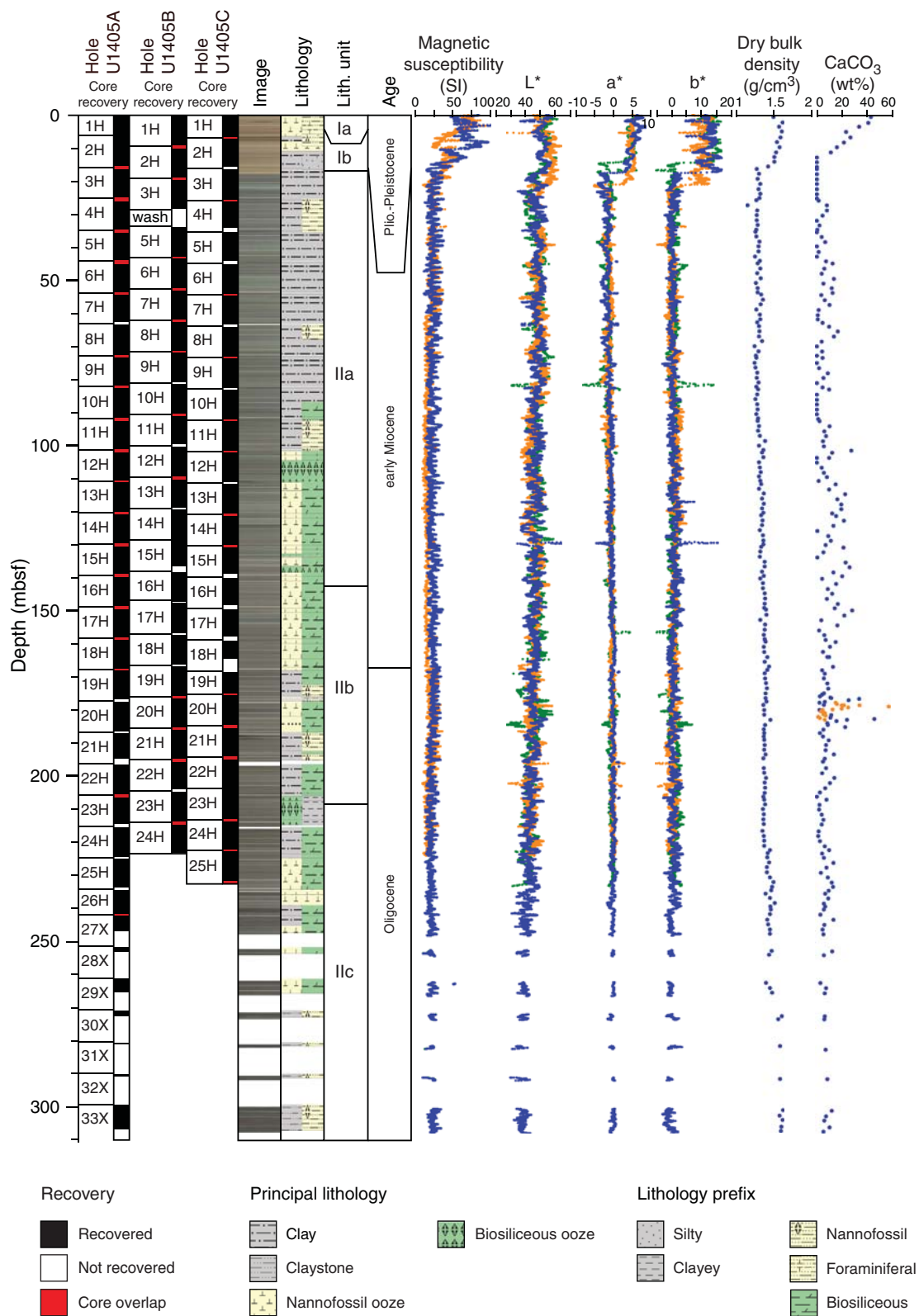
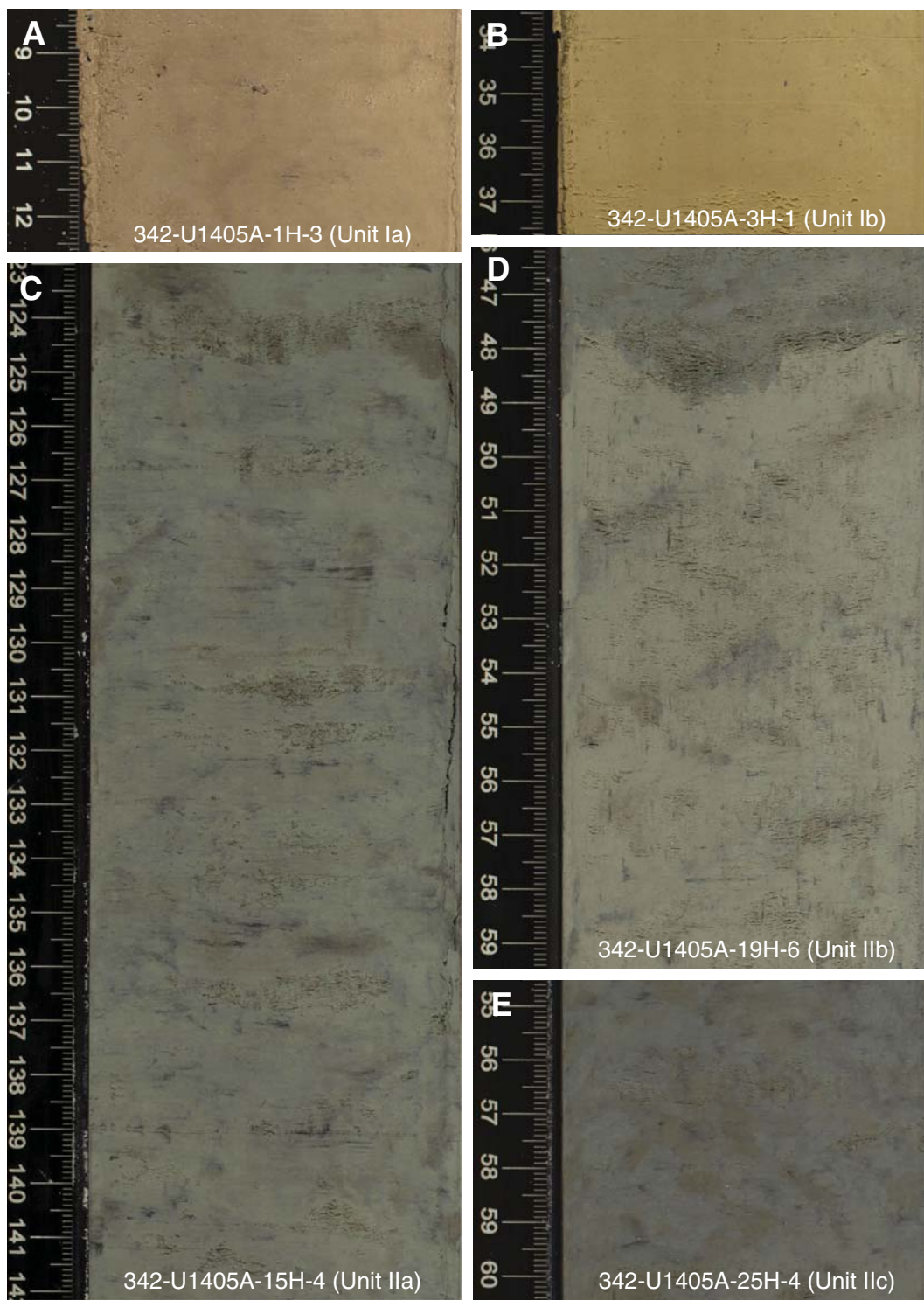


Figure F5. Lithostratigraphic summary, Site U1405.



**Figure F6.** Line scan images from most common lithologies, Site U1405. A. Pliocene–Pleistocene nannofossil ooze, Subunit Ia. B. Upper Pliocene silty clay, Subunit Ib. C. Lower Miocene biosiliceous clay, Subunit IIa. D. Transition at 48 cm from biosiliceous clay above to nannofossil ooze below at or immediately below the Oligocene–Miocene transition at the Subunit IIa/IIb boundary. E. Upper Oligocene biosiliceous clay, Subunit IIc.



**Figure F7.** Photomicrographs of smear slides indicating the dominant lithologies of Units I and II, Site U1405. A. Silty clay, Subunit Ib. B. Nannofossil ooze with radiolarians, Subunit IIa. C. Nannofossil ooze, Subunit IIb. D. Diatomaceous clay with radiolarians, Subunit IIc.

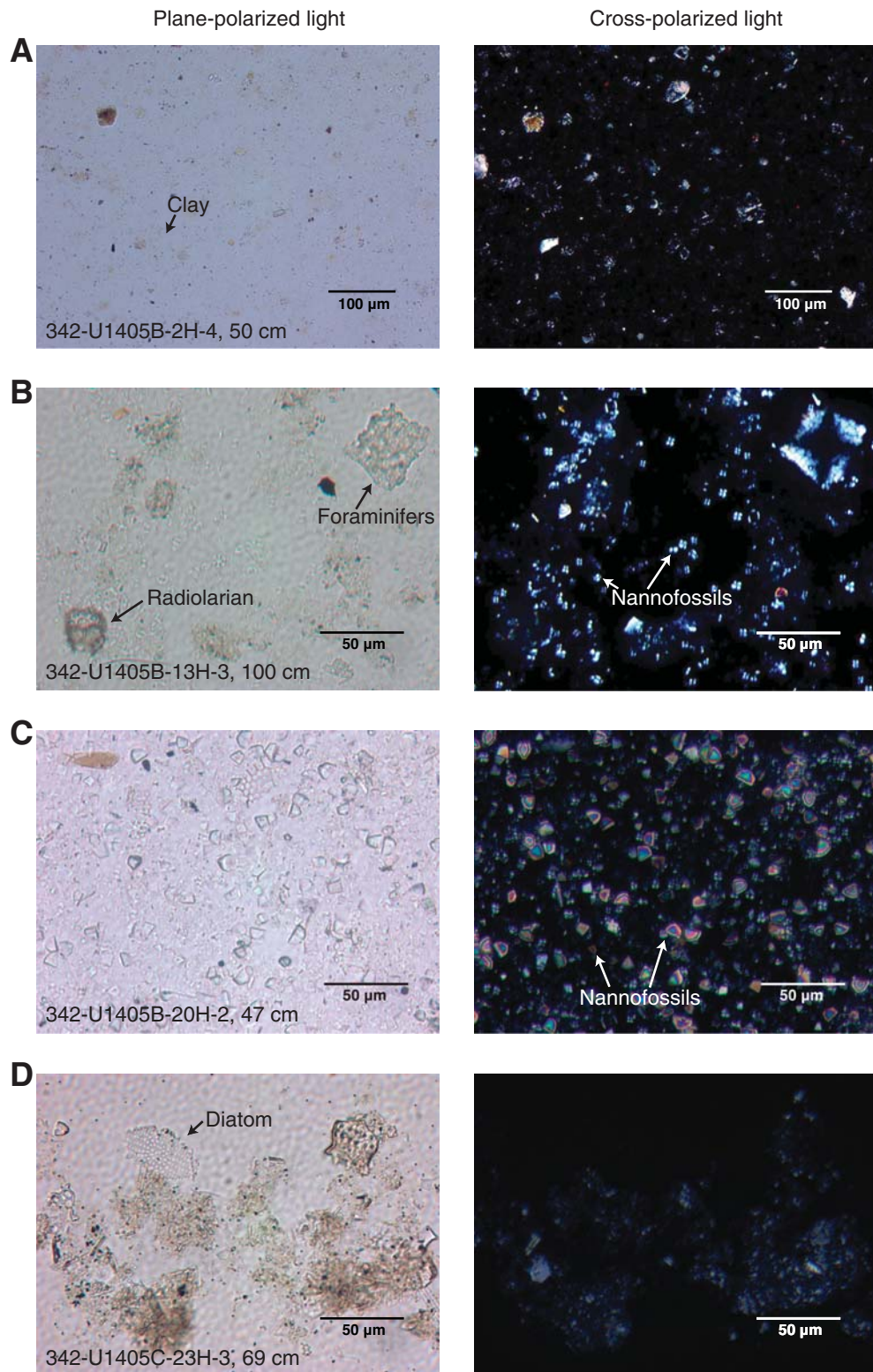


**Figure F8.** Plots of smear slide results of major biogenic and lithologic components and their relative abundance, Hole U1405A. VA = very abundant, A = abundant, C = common, F = few, P = present.

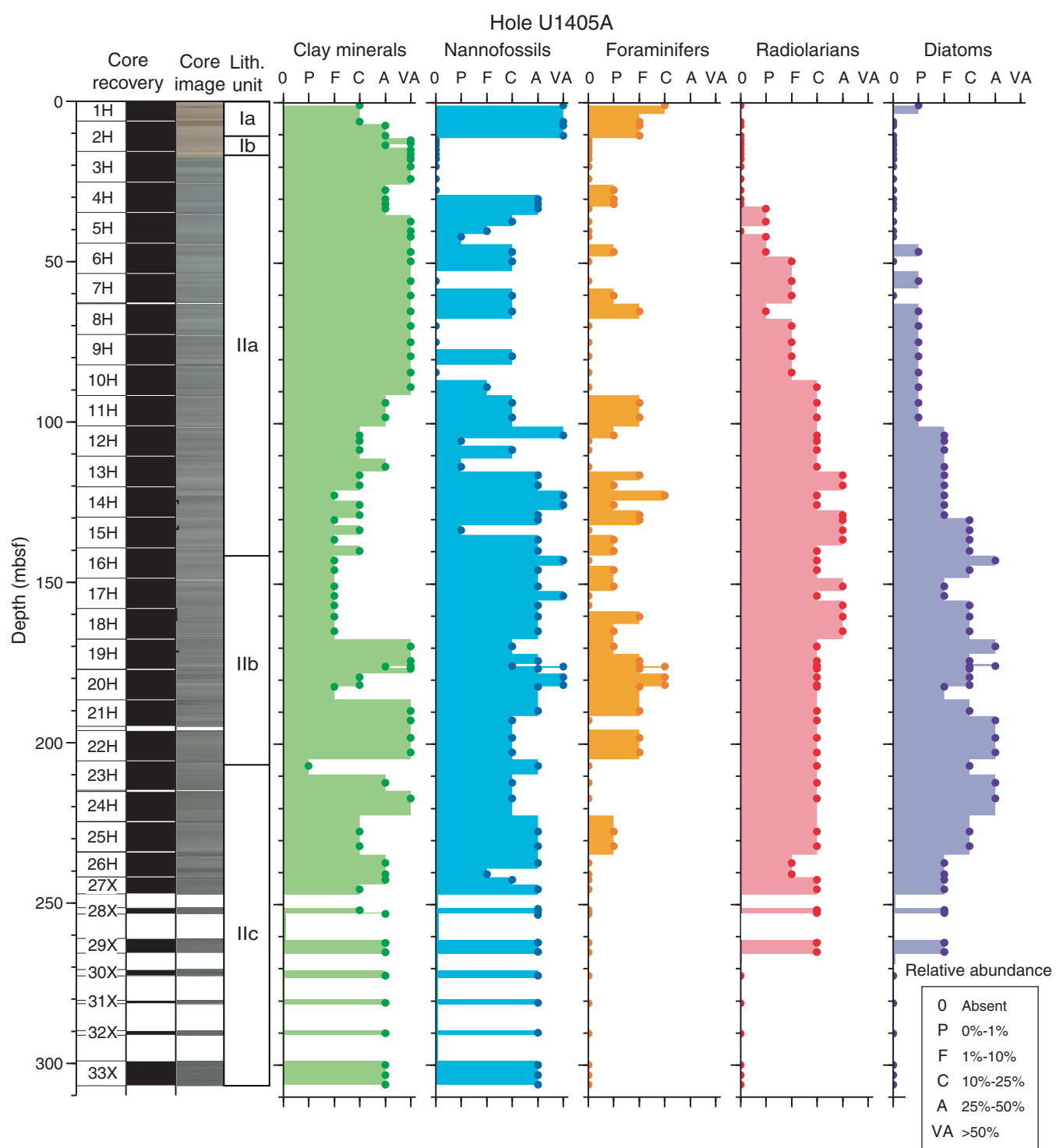


**Figure F9.** Plots of smear slide results of major biogenic and lithologic components and their relative abundance, Hole U1405B. VA = very abundant, A = abundant, C = common, F = few, P = present.

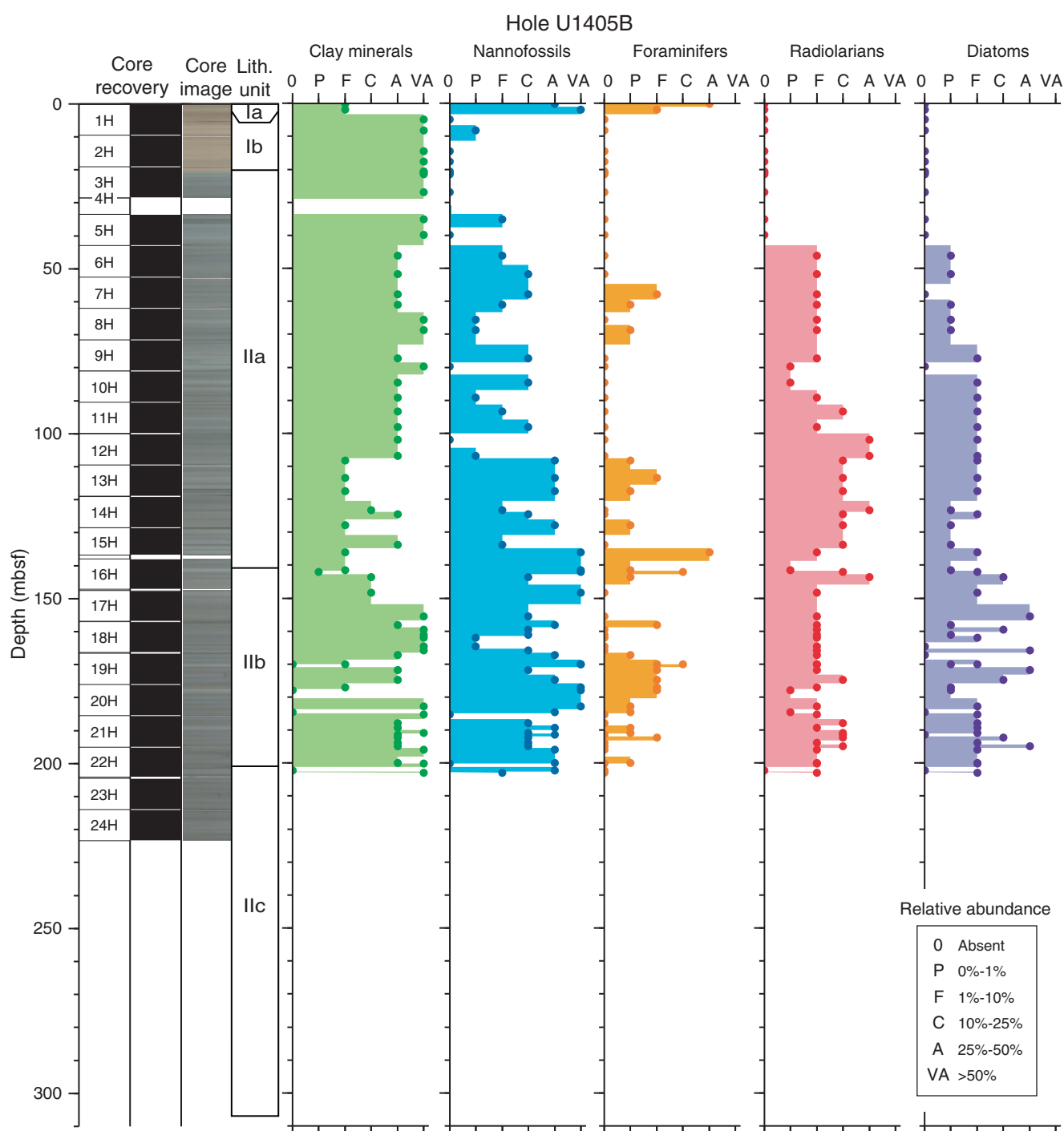


**Figure F10.** Plots of smear slide results of major biogenic and lithologic components and their relative abundance, Hole U1405C. VA = very abundant, A = abundant, C = common, F = few, P = present.

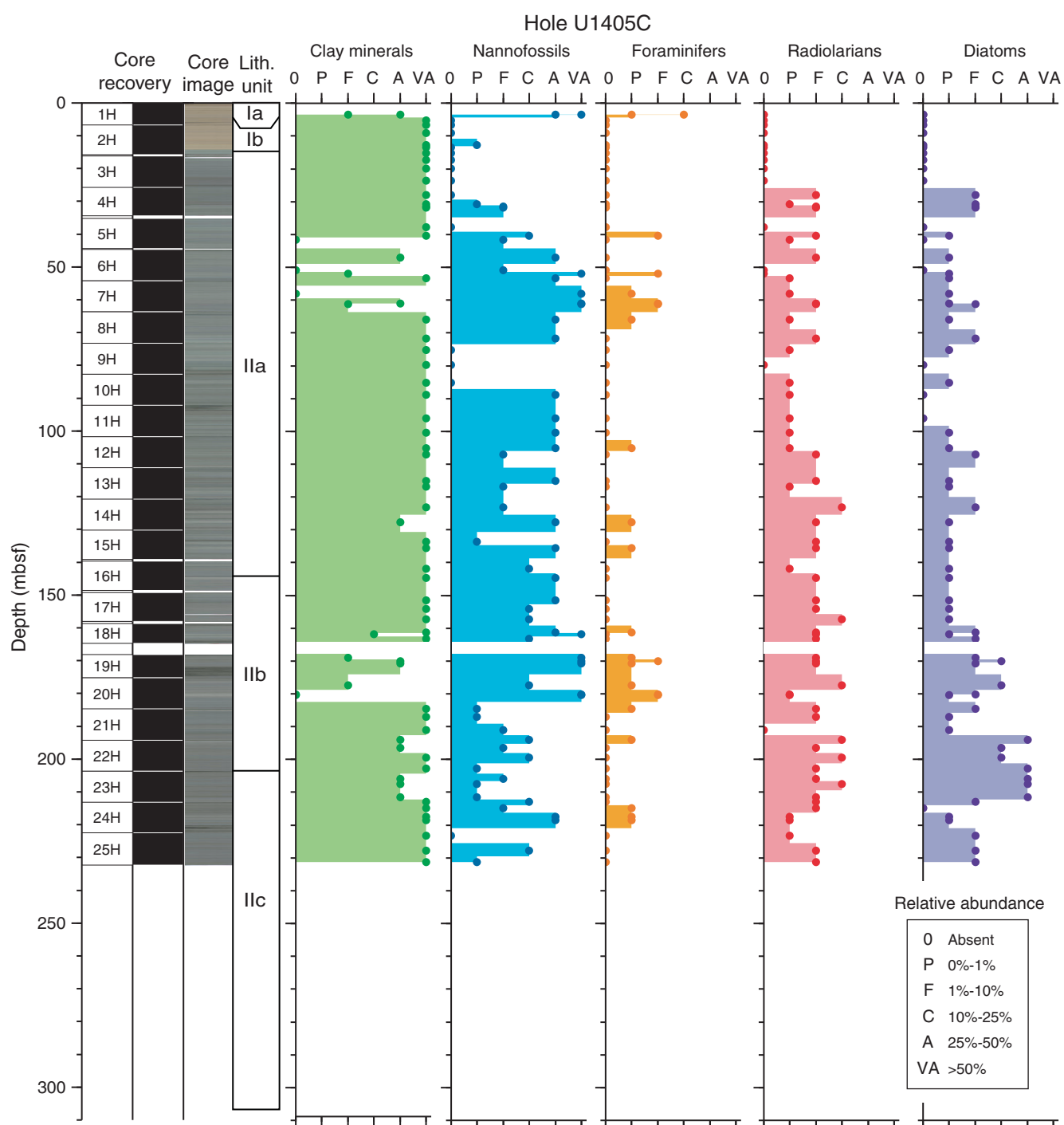


**Figure F11.** Plots of gamma ray attenuation (GRA) density, color reflectance ( $L^*$ ), and carbonate content of Subunit IIb around the Oligocene–Miocene transition, Site U1405. Layers I–IV (based on direct observation) are indicated by light brown bands. Relative time is indicated by magnetostratigraphy and the first occurrence (FO) and last occurrence (LO) of *Sphenolithus delphix* (Holes U1405A and U1405B). The true color of section line scan images may be distorted in print.

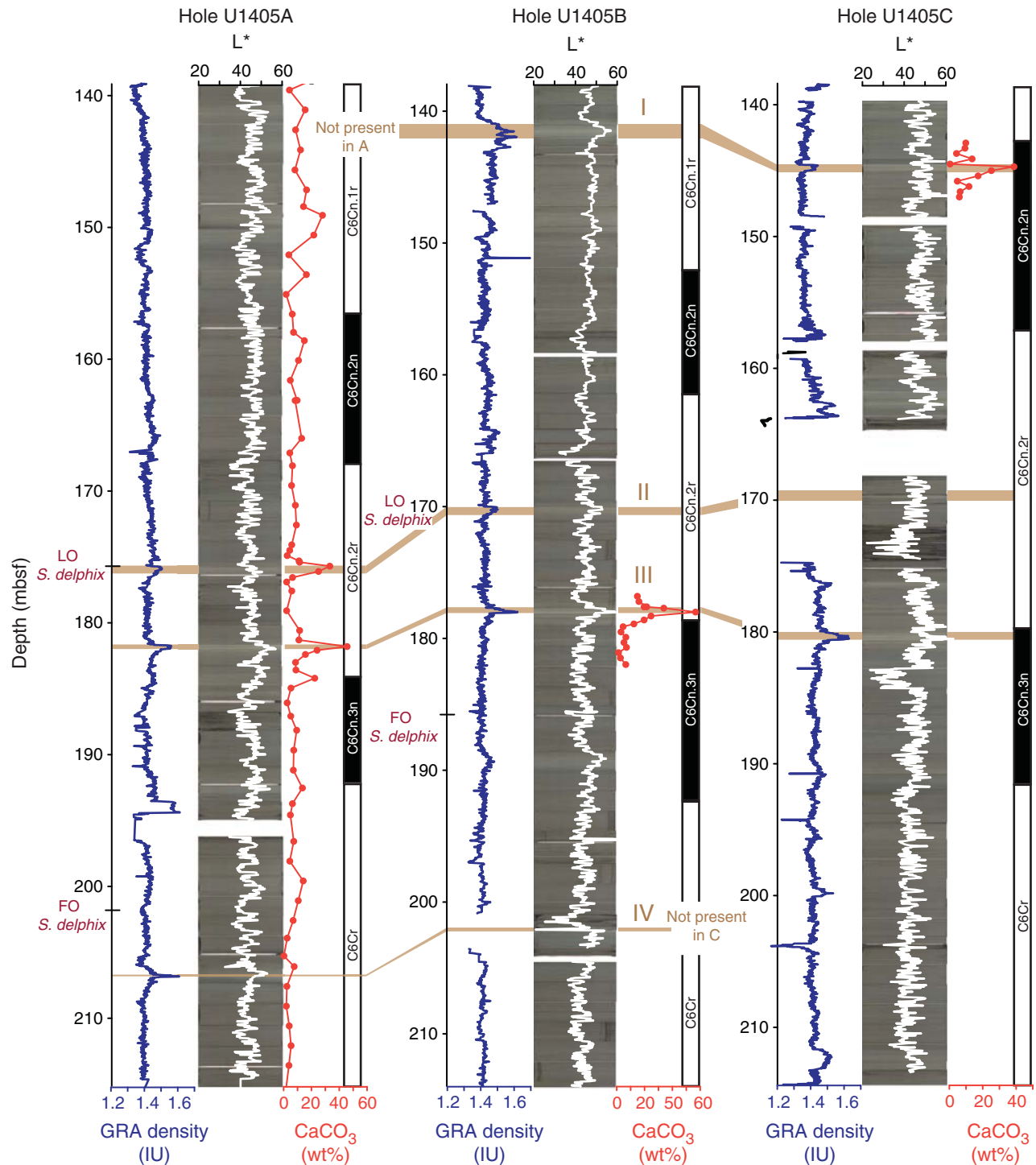


**Figure F12.** Core images of sharp upper contacts of carbonate events in Subunit IIb, Site U1405. Brown bars and roman numerals relate the carbonate-rich events to those shown in Figure F11. In each hole, the stratigraphic thickness of core present but not visualized is indicated by broken lines and accompanying thickness.

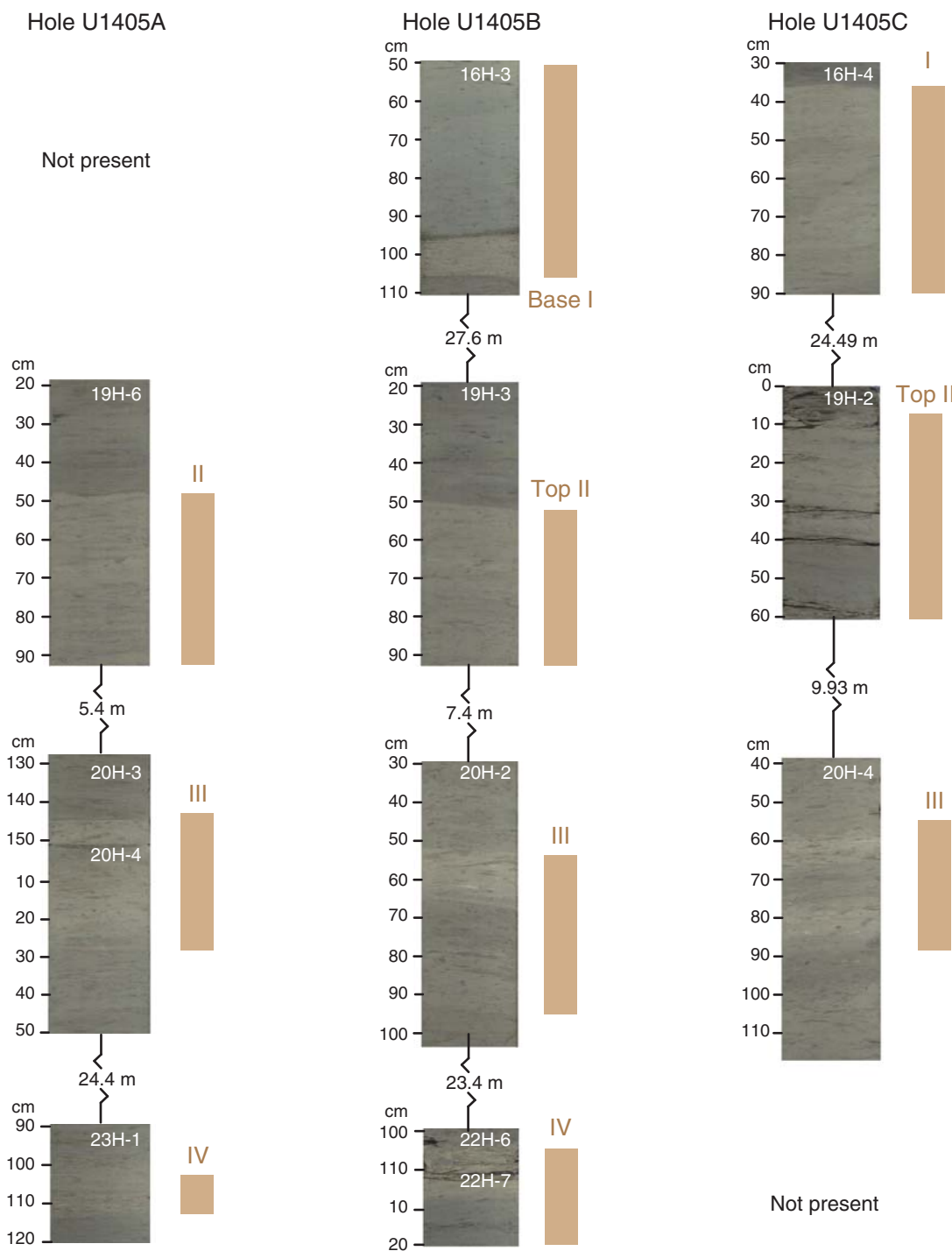
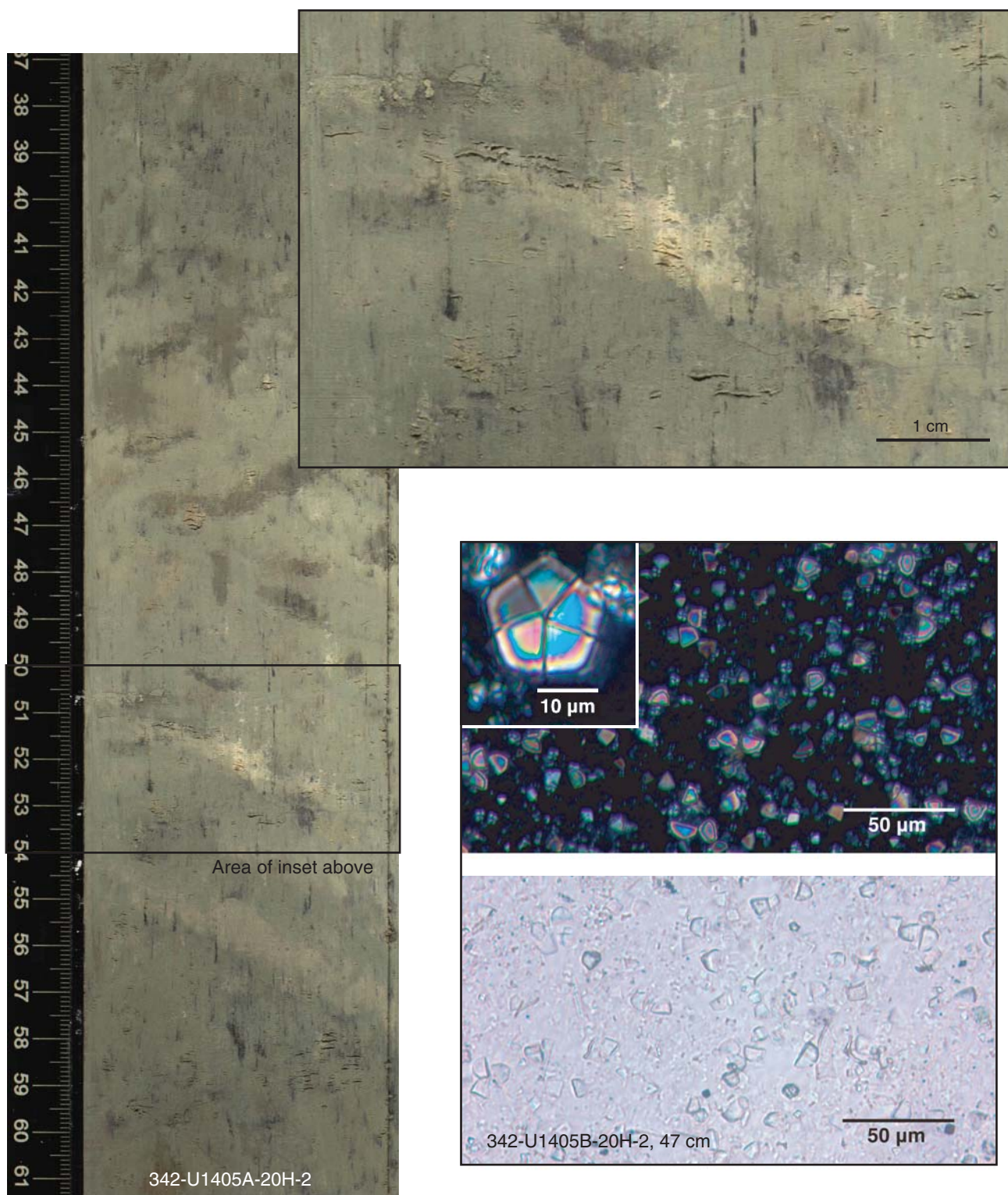
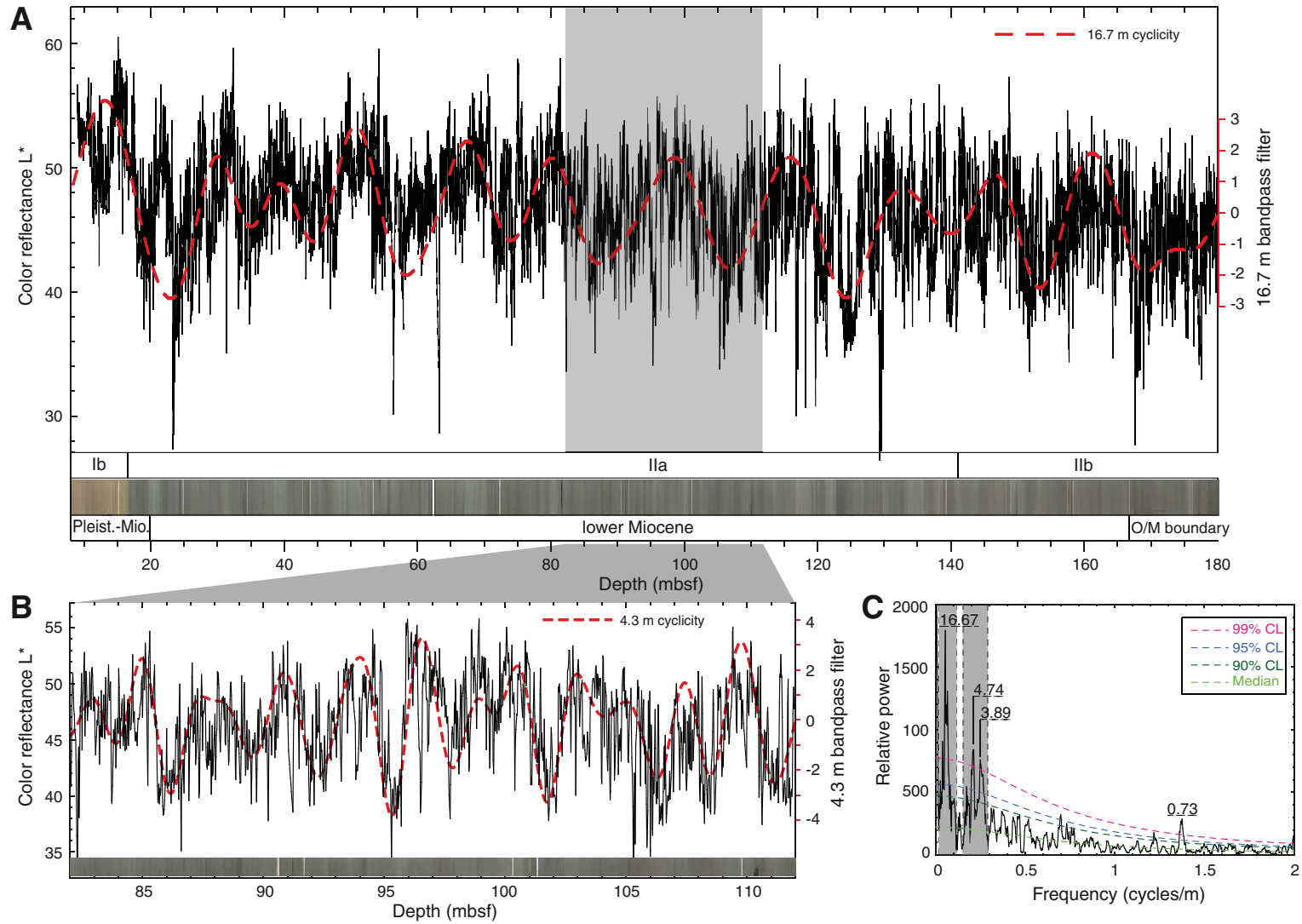


Figure F13. Line scan images and photomicrographs of *Braarudosphaera*-rich layer in Subunit IIb, Site U1405.



**Figure F14.** Plots of color reflectance L\* variations, Hole U1405A. Measurements were performed at high resolution (2.5 cm) on section halves using spectrophotometry (point measurements from Section Half Multisensor Logger). A. L\* variations at 9–180 mbsf. A bandpass Gaussian filter output highlights 16.7 m cyclicity. B. Expanded view of the gray area in A. A bandpass Gaussian filter output highlights 4.3 m cyclicity. C. Power spectrum of A with red noise modeling. Only periods (in meters) of peaks exceeding 99% confidence level (CL) are shown. The two gray areas indicate frequency pass bands filtered to isolate the 16.7 and 4.3 m cyclicitics shown in A and B. Note that only the low-frequency portion of the spectrum (0–2 cycles/m) is plotted to highlight the prominent 16.7 and 4.3 m cyclicitics (see text for discussion).



**Figure F15.** X-ray diffractograms for five selected samples from different lithostratigraphic units, Site U1405. The data show a rather uniform picture of the sediment composition. Only calcite occurs in some samples and not others, and the clay minerals show subtle changes, but detailed quantification would require analysis of the  $<2\text{ }\mu\text{m}$  fraction.

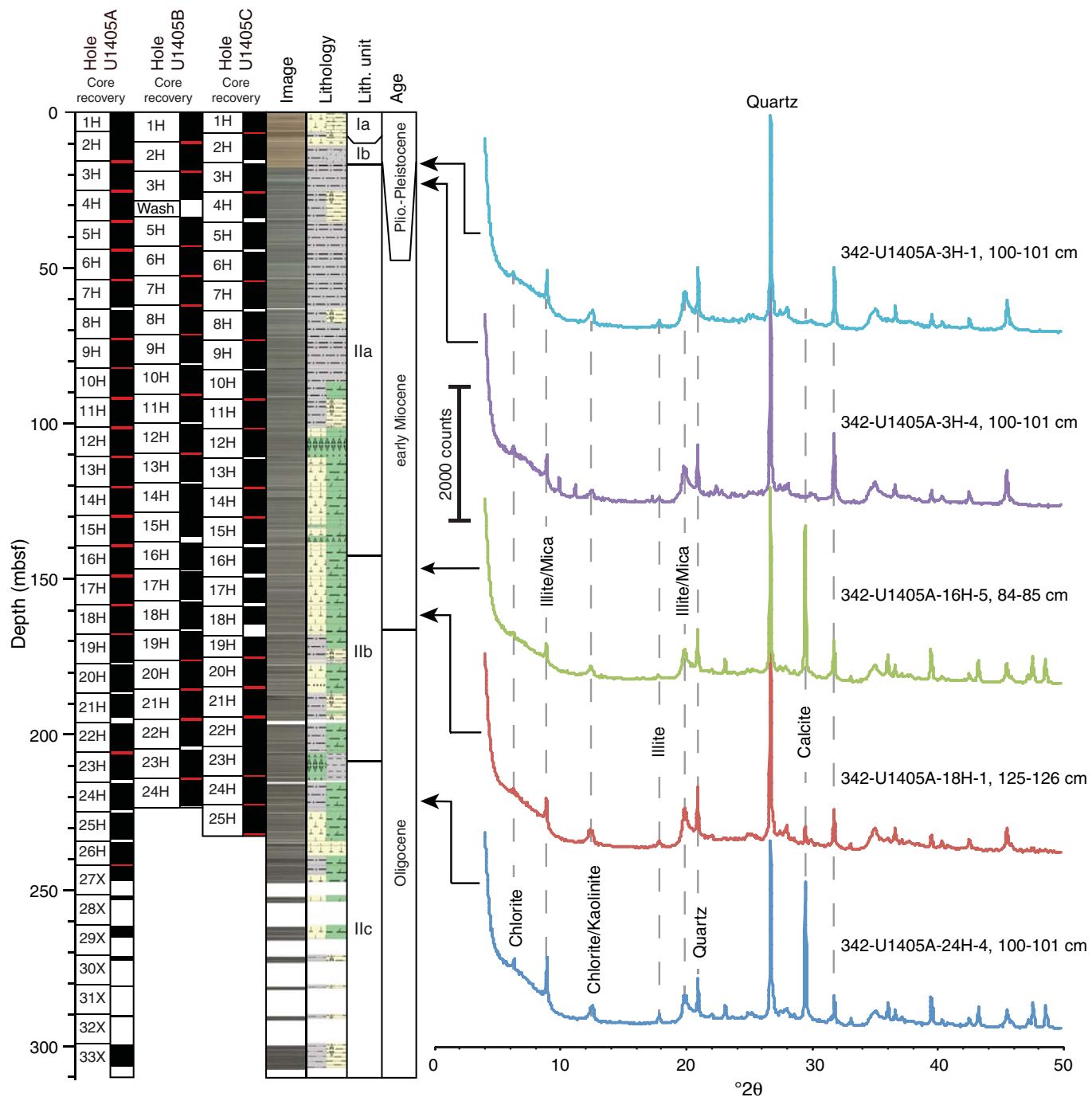
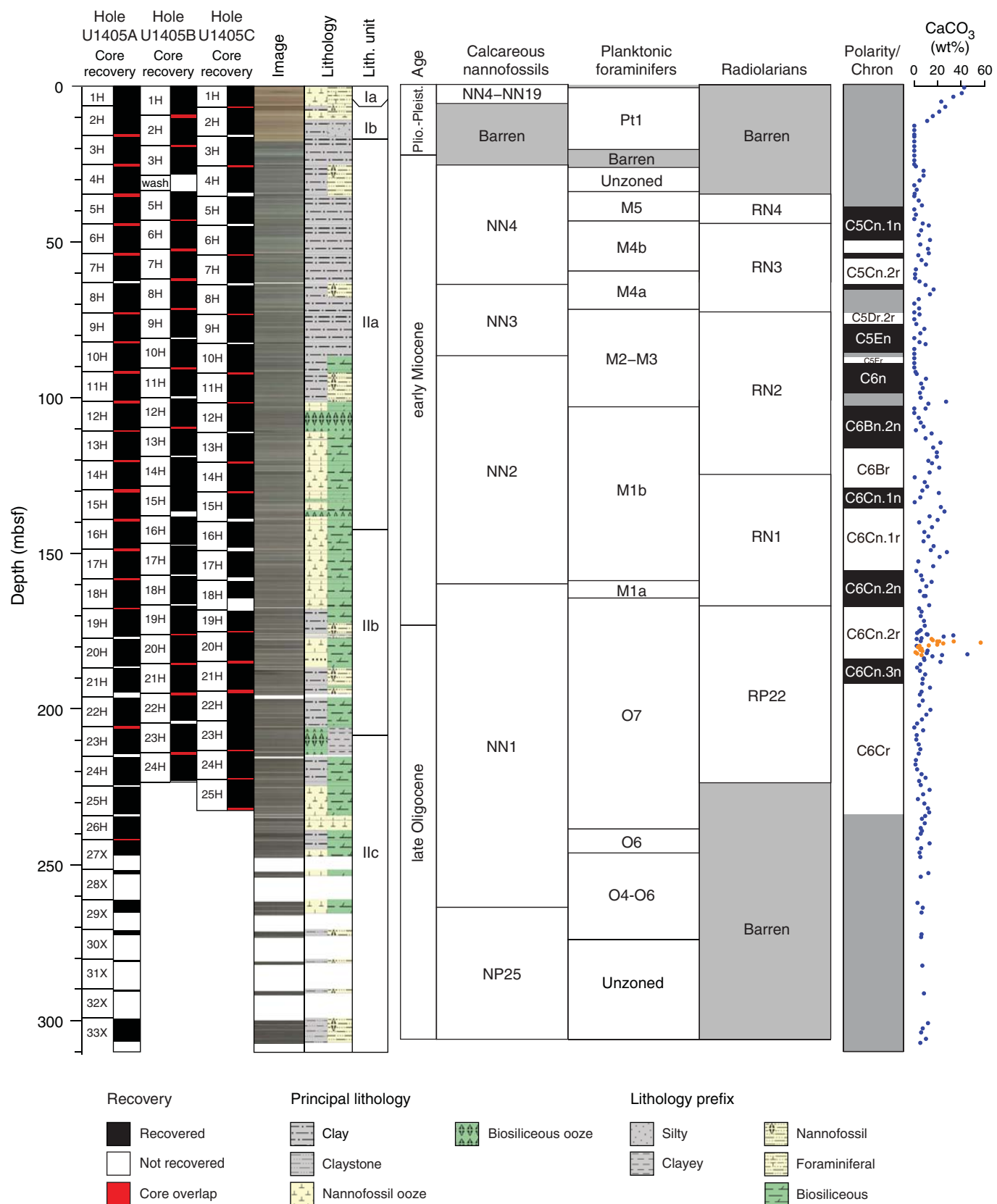
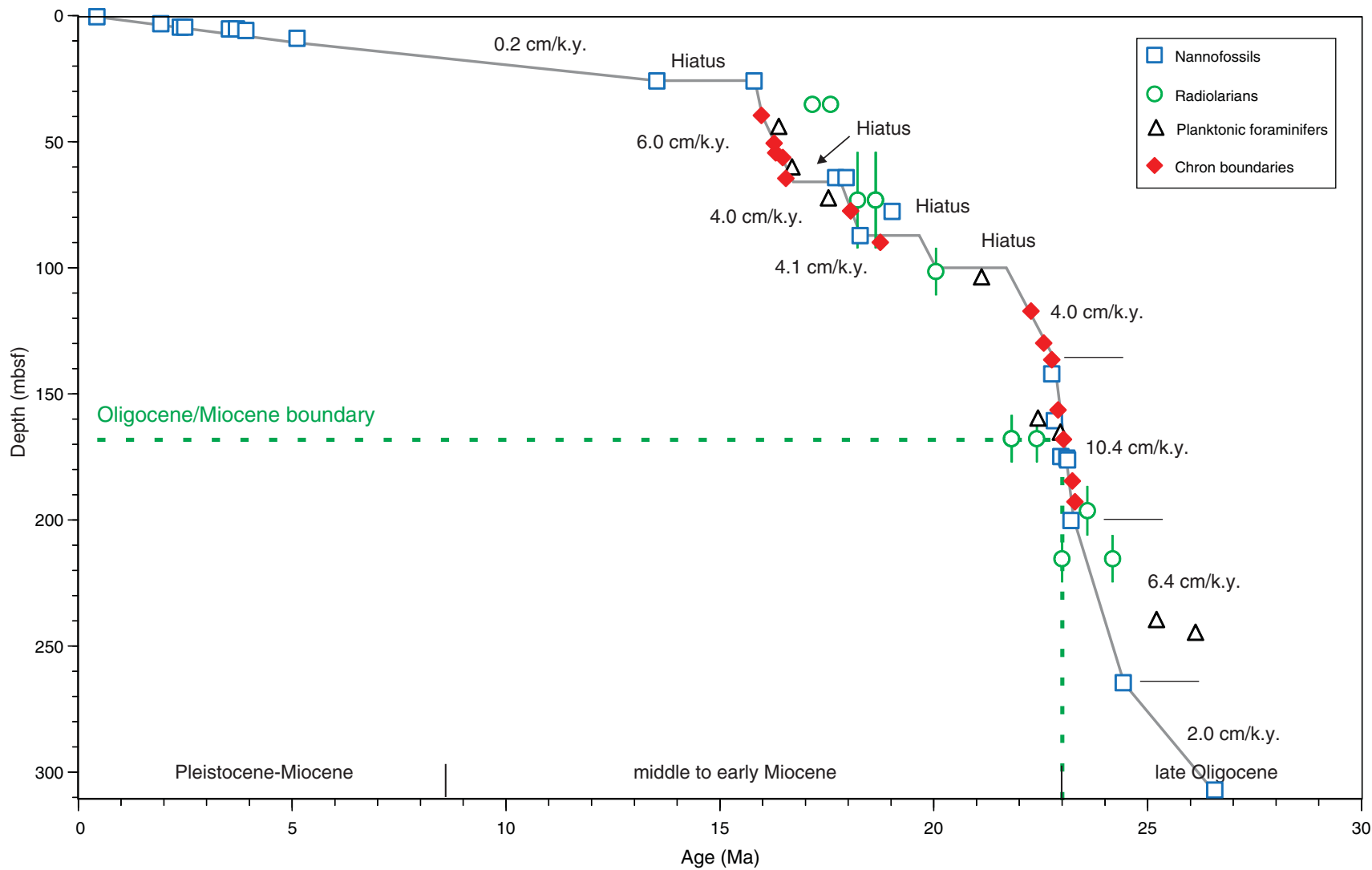


Figure F16. Integrated calcareous and siliceous microfossil biozonation, Site U1405.



**Figure F17.** Plot of age-depth model for Hole U1405A showing biostratigraphic and magnetostratigraphic datums. Also shown are estimated linear sedimentation rates for line segments based on the datums listed in Table T16.



**Figure F18.** Plots of group abundance and preservation of calcareous and siliceous microfossils, Site U1405. Open and solid symbols represent Holes U1405A and U1405B, respectively. Abundance: B = barren, P = present, R = rare, F = few, C = common, A = abundant, D = dominant. Preservation: P = poor, M = moderate, G = good, VG = very good.

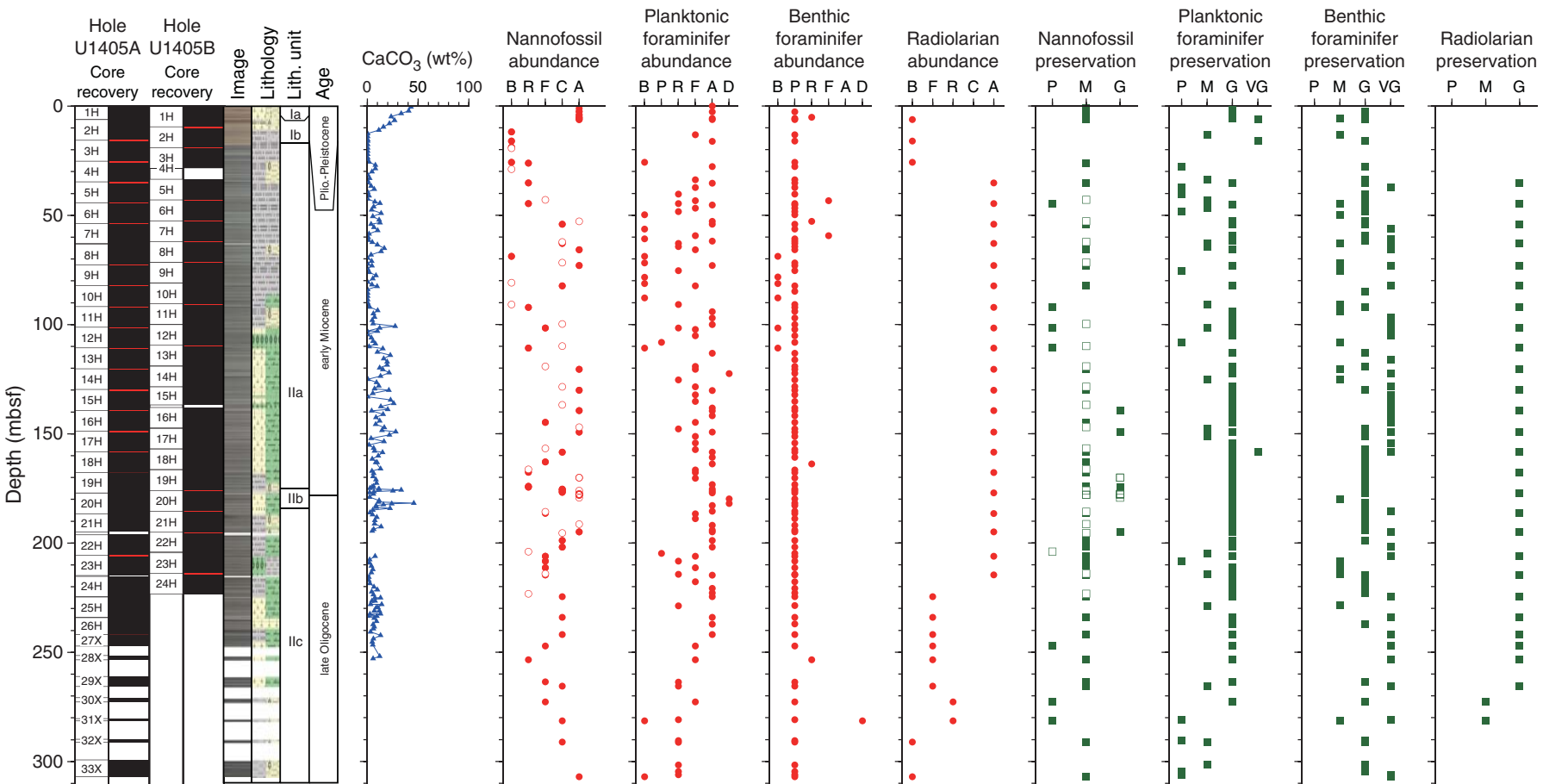


**Figure F19.** Photomicrographs of upper Oligocene/lower Miocene boundary interval nannofossils, Site U1405. Upper panel is age-diagnostic upper Oligocene (*Sphenolithus ciperoensis*) and Oligocene/Miocene boundary interval sphenoliths (*Sphenolithus delphix* and *Sphenolithus capricornutus*). Lower panel is a braarudosphaerid ooze sample predominantly showing abundant fragmented, trapezoidal, pentalith segments but also a complete *Braarudosphaera* specimen in the center.

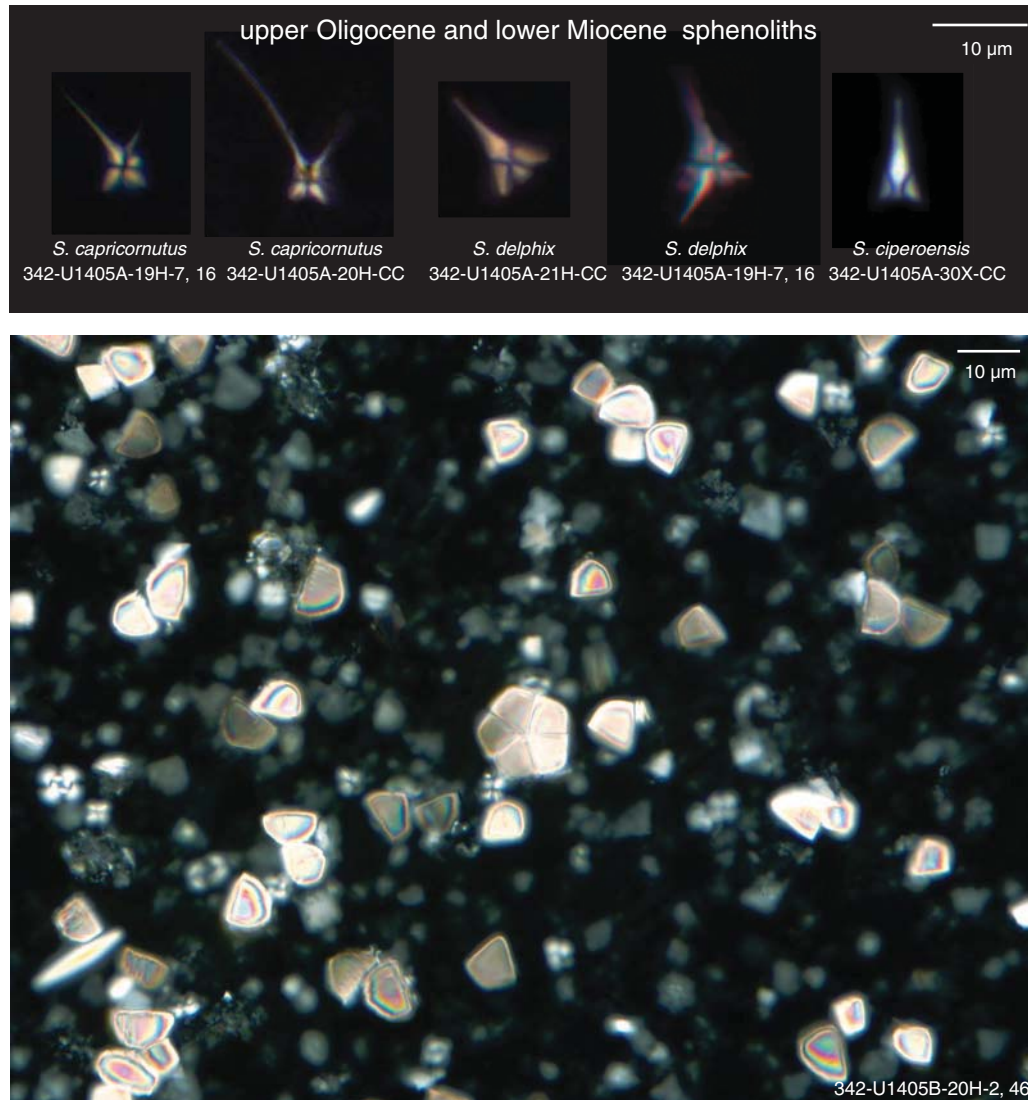


**Figure F20.** Photomicrographs of typical lower Miocene planktonic foraminiferal assemblage (upper panel; Sample 342-U1405A-17H-CC) including the morphologically distinctive dentoglobigerinids (lower panel; Sample 342-U1405A-14H-2, 100–102 cm), so named after the presence of their characteristic calcite “teeth” secreted over the apertural opening.



**Figure F21.** Photomicrograph of the remarkably good preservation of lower Miocene planktonic foraminifers at Site U1405 revealing semiglassy taphonomy and even the presence of relict spines within the umbilici. The first appearance of *Paragloborotalia kugleri* marks the base of Subzone M1a, ~70 k.y. after the Oligocene/Miocene boundary (Samples 342-U1405A-13H-6, 100–102 cm; 15H-2, 100–102 cm; 15H-CC; and 16H-CC).



**Figure F22.** Selected benthic foraminiferal taxa, Site U1405. A. *Laticarinina pauperata* (Sample 342-U1405A-15H-6, 100–102 cm). B. *Parafissurina* sp. (Sample 342-U1405A-19H-6, 100–102 cm). C. *Pleurostomella acuta* (Sample 342-U1405A-15H-6, 100–102 cm). D. *Pleurostomella tenius* (Sample 342-U1405A-15H-2, 100–102 cm). E. *Stilostomella lepidula* (Sample 342-U1405A-14H-6, 70–72 cm). F. *Stilostomella subspinosa* (Sample 342-U1405A-15H-6, 100–102 cm). G, H. *Oridorsalis umbonatus* (Sample 342-U1405A-13H-2, 100–102 cm). I, J. *Cassidulina subglobosa* (Sample 342-U1405A-14H-6, 70–72 cm). K, L. *Pullenia bulloides* (Sample 342-U1405A-16H-2, 100–102 cm). Scale bars = 100 µm.

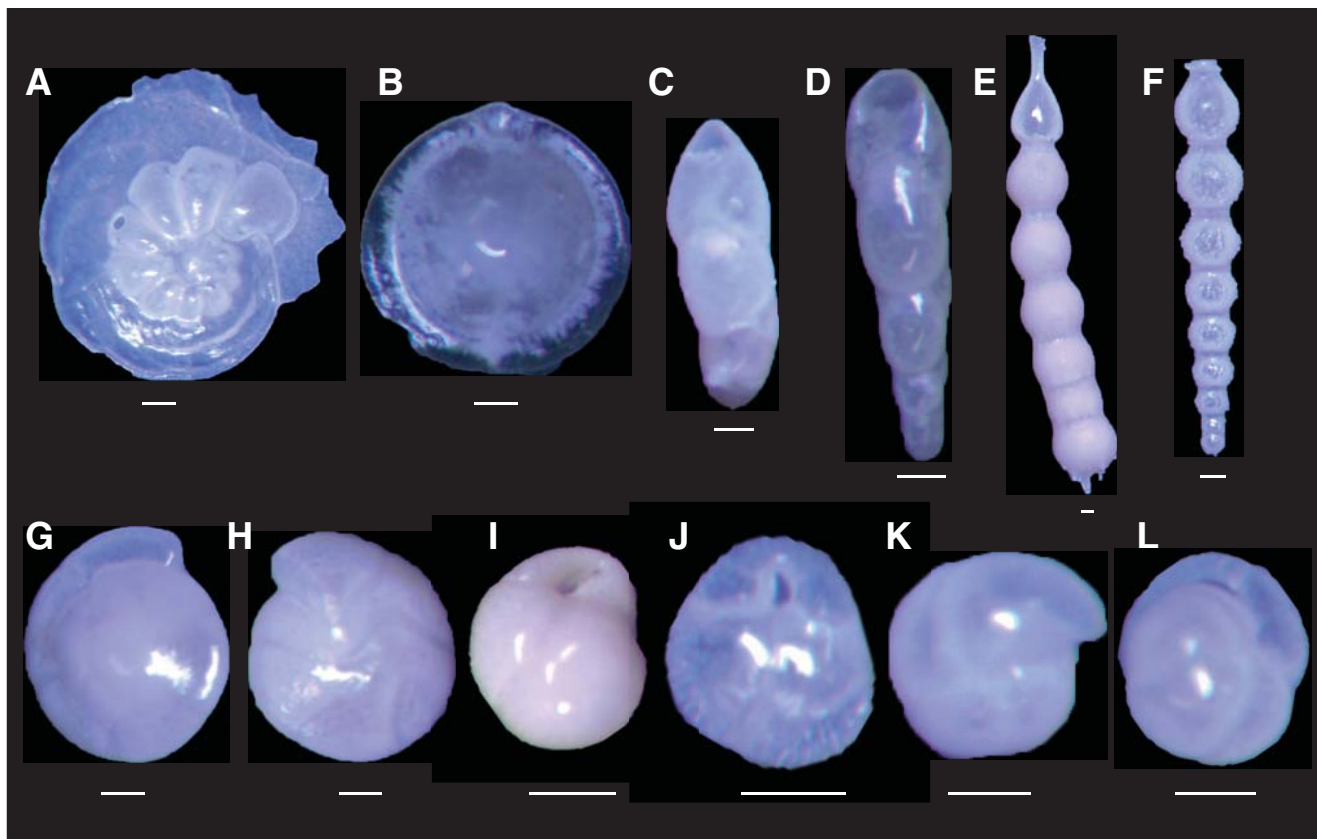


**Figure F23.** Plots of downhole variation of magnetic susceptibility and paleomagnetic data, Hole U1405A. Magnetization intensity, inclination, and declination are after 20 mT demagnetization. Only oriented advanced piston corer (APC) intervals show directions in geographic coordinates. Directions from all other intervals are shown in sample coordinates. For discrete sample data, if the samples were analyzed by principal component analysis (PCA; Kirschvink, 1980), then directions are shown according to PCA declination and inclination. Otherwise, directions following 20 mT demagnetization are shown. XCB = extended core barrel. Polarity: black = normal chron, white = reversed chron, gray = unidentified interval.

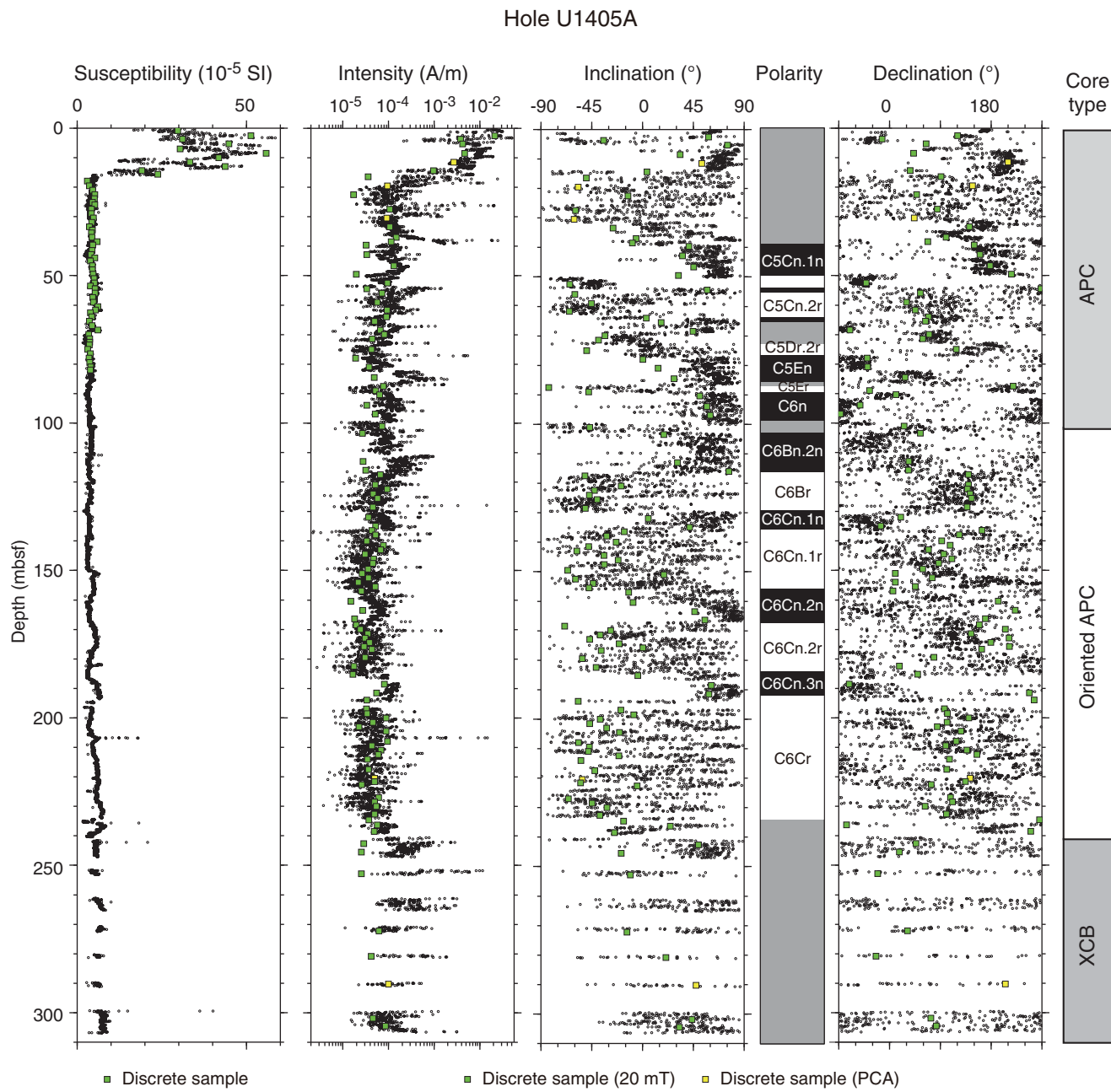


**Figure F24.** Plots of downhole variation of magnetic susceptibility and paleomagnetic data, Hole U1405B. Magnetization intensity, inclination, and declination are after 20 mT demagnetization. Directions are shown in geographic coordinates. APC = advanced piston corer. Polarity: black = normal chron, white = reversed chron, gray = unidentified interval.

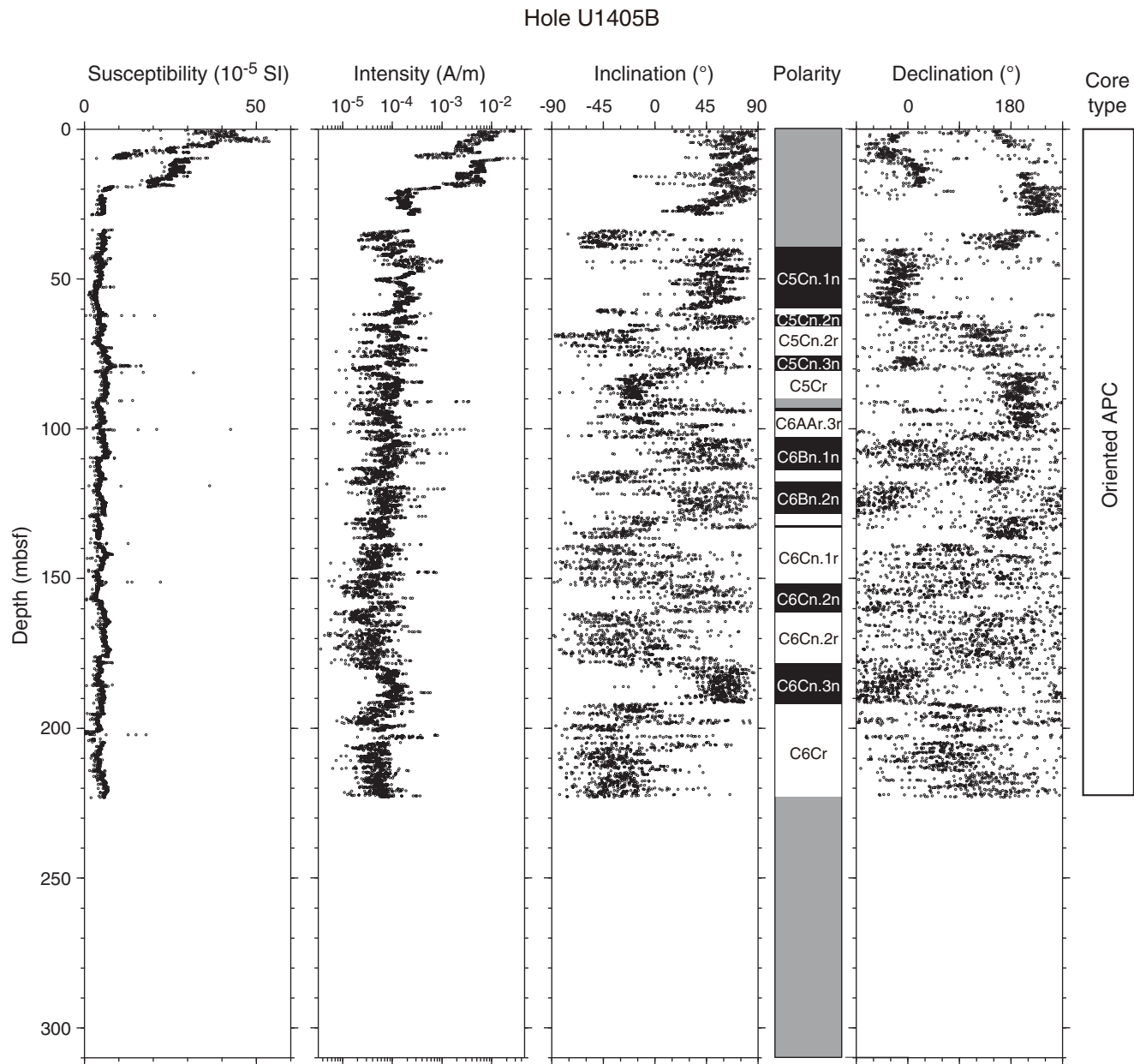


**Figure F25.** Plots of downhole variation of magnetic susceptibility and paleomagnetic data, Hole U1405C. Magnetization intensity, inclination, and declination are after 20 mT demagnetization. Directions are shown in sample coordinates. APC = advanced piston corer. Polarity: black = normal chron, white = reversed chron, gray = unidentified interval.

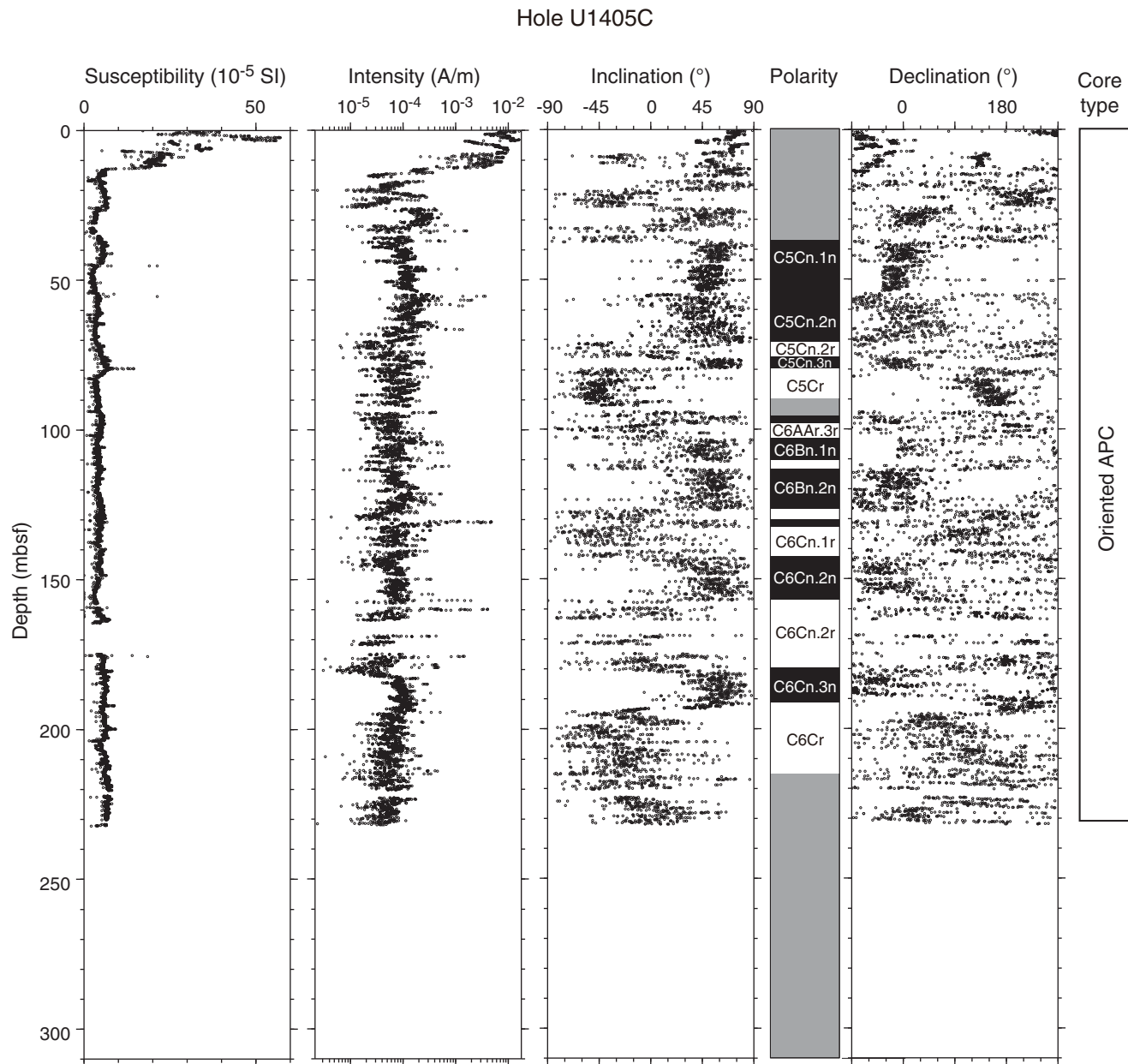


**Figure F26.** Schematic diagram illustrating the “antennae” effect experienced during Expedition 342 that channeled stray radio or electromagnetic field (EMF) from the core laboratory into the measurement region of the superconducting rock magnetometer (SRM). Illustration of the  $y$ -axis coil is redrawn from Oda and Shibuya (1996). SQUIDs = superconducting quantum interference devices.

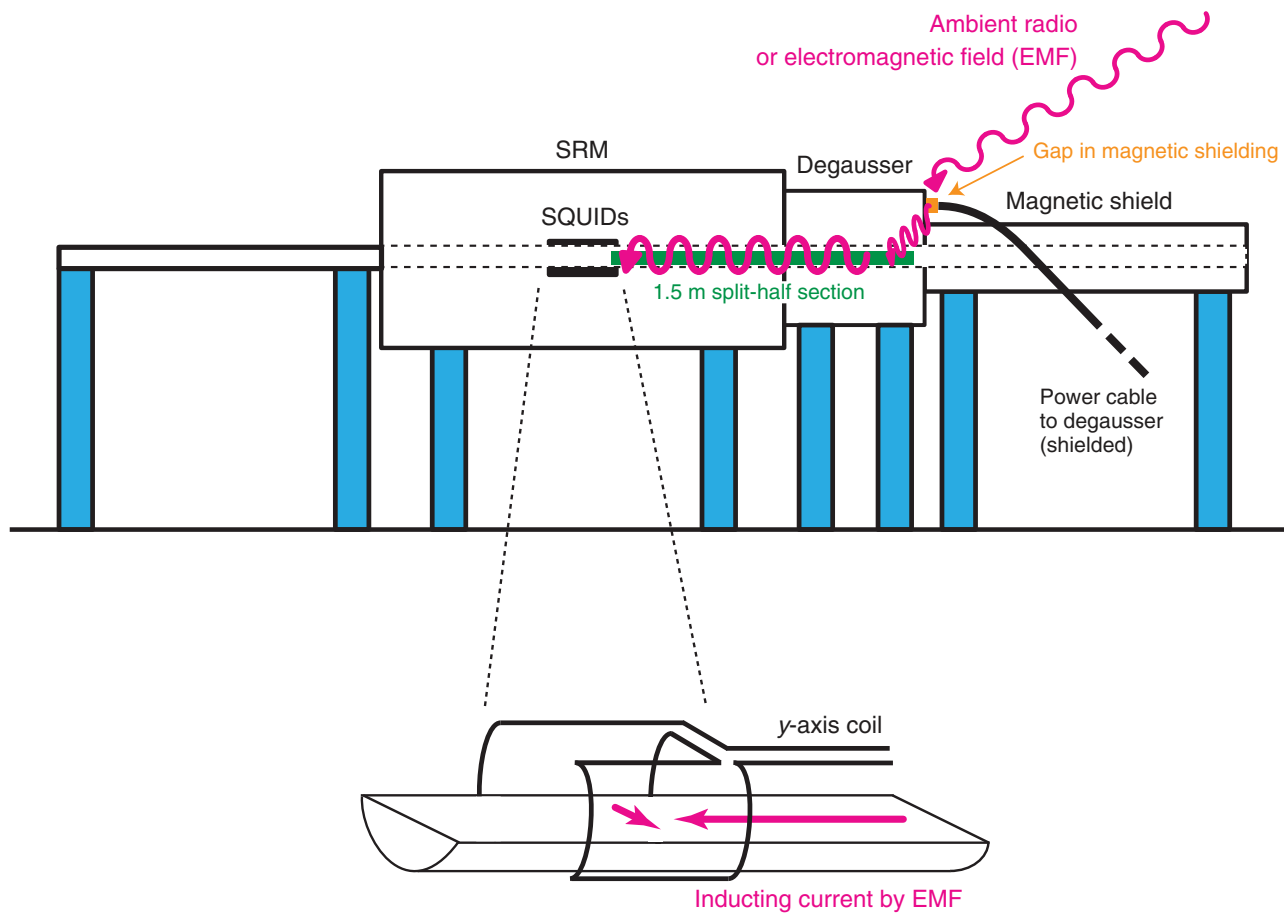


**Figure F27.** Plots of representative alternating-field (AF) demagnetization results for discrete paleomagnetic samples, Site U1405. Upper plots show intensity variation with progressive demagnetization, and lower plots show vector endpoints of paleomagnetic directions on orthogonal vector diagrams (i.e., Zijderveld plots). Vector diagrams indicate reasonably resolved characteristic remanent magnetization (ChRM) directions for the (A) normal and (B) reversed chronos. Solid circles = horizontal projections, open circles = vertical projections, gray circles = data not used to calculate the ChRM direction, black dashed line = ChRM direction. Inc = inclination, Dec = declination, MAD = maximum angle of deviation.

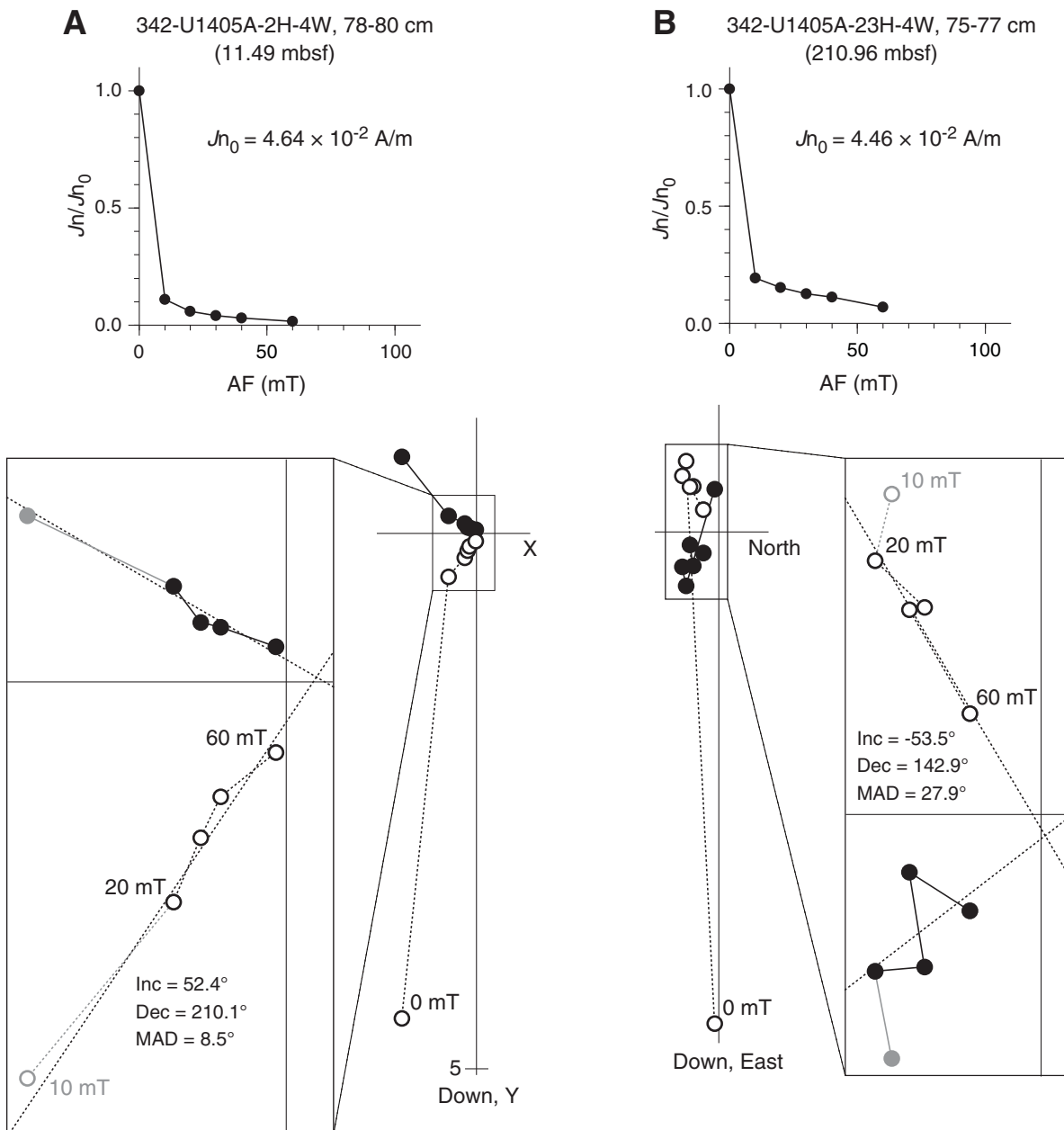


**Figure F28.** Illustration of magnetostratigraphy, Site U1405. Core recovery: black = recovered, white = not recovered, red = core overlap.

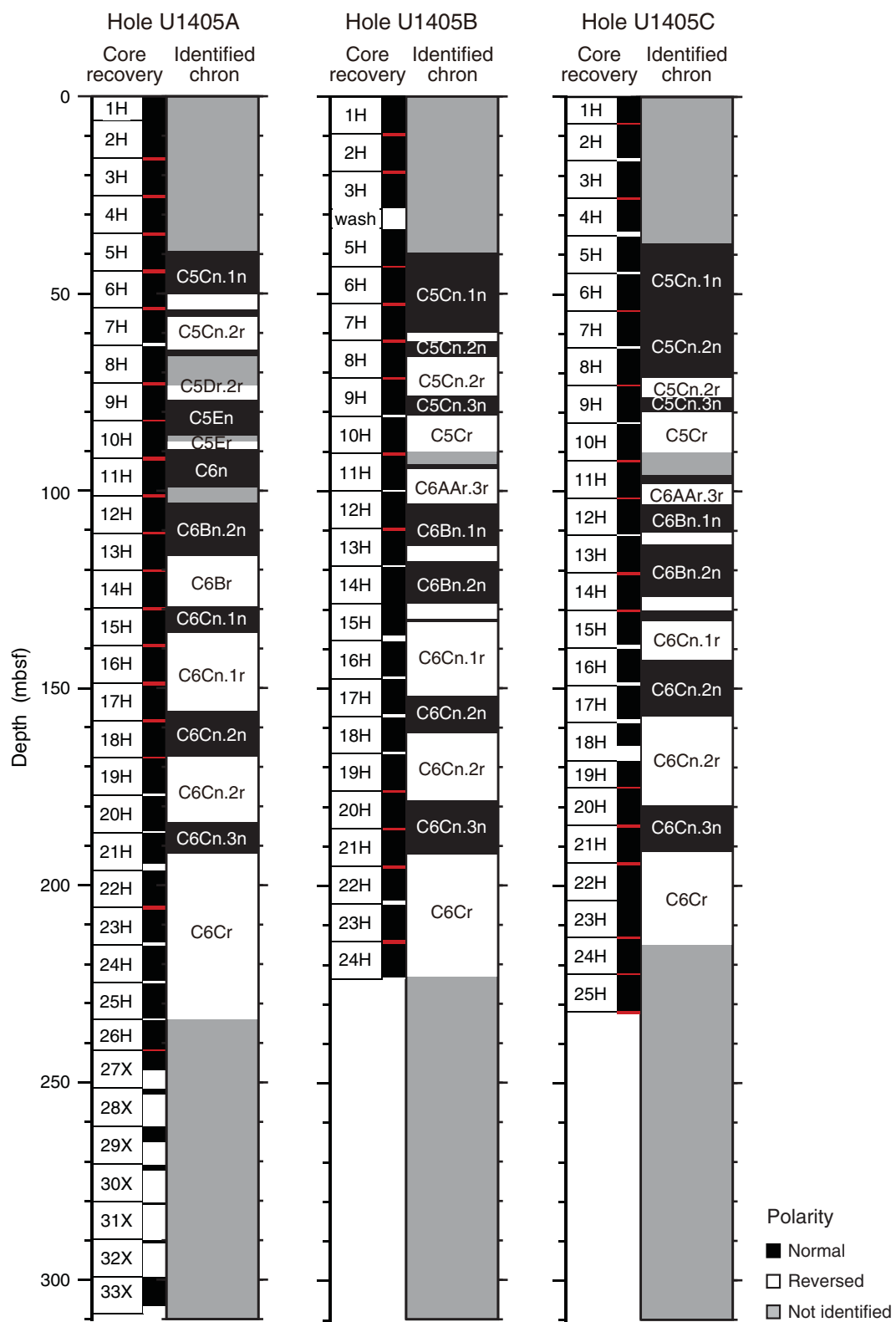


**Figure F29.** Plots of anisotropy of magnetic susceptibility vs. depth, Hole U1405A. Separation of eigenvalues is related to the shape and degree of the magnetic fabric (see “[Paleomagnetism](#)” in the “Methods” chapter [Norris et al., 2014a]). For example, if  $\tau_1$  and  $\tau_2$  are close or indistinguishable but distinct from  $\tau_3$ , then the bulk fabric is oblate. Lithostratigraphic units are described in “[Lithostratigraphy](#).” Eigenvalues:  $\tau_1$  = maximum,  $\tau_2$  = intermediate,  $\tau_3$  = minimum.  $V_3$  = minimum eigenvector,  $P$  = degree of anisotropy ( $\tau_1 / \tau_3$ ). APC = advanced piston corer, XCB = extended core barrel.

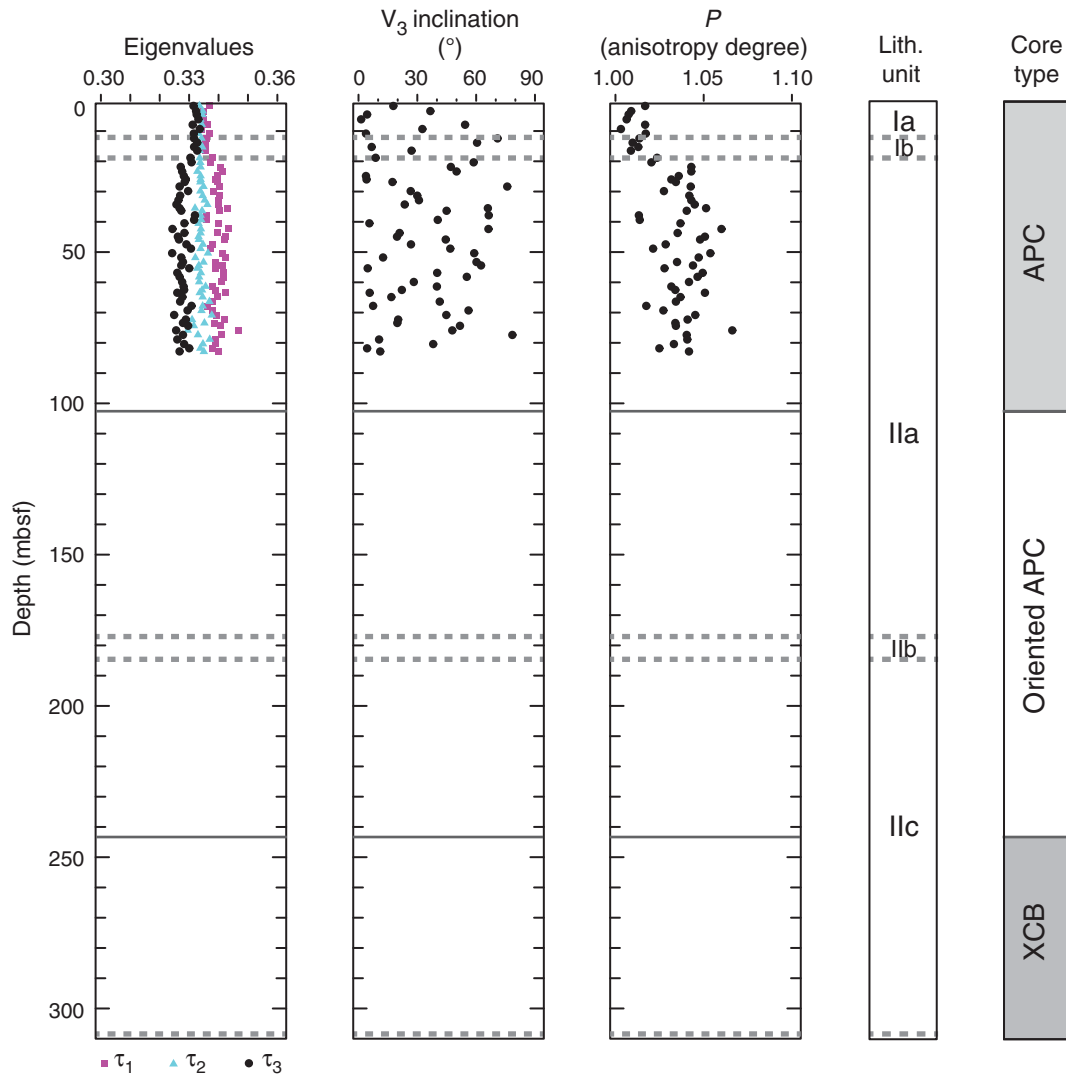


**Figure F30.** Plots of linear sedimentation rate (LSR), dry bulk density (DBD), carbonate content, and mass accumulation rate (MAR) at 200 k.y. time steps, Hole U1405A. Solid black diamonds show the inflection points in estimated LSR, DBD, and carbonate content. Geologic ages are shown on the GTS2012 timescale (Gradstein et al., 2012). CAR = carbonate mass accumulation rate, nCAR = noncarbonate mass accumulation rate.

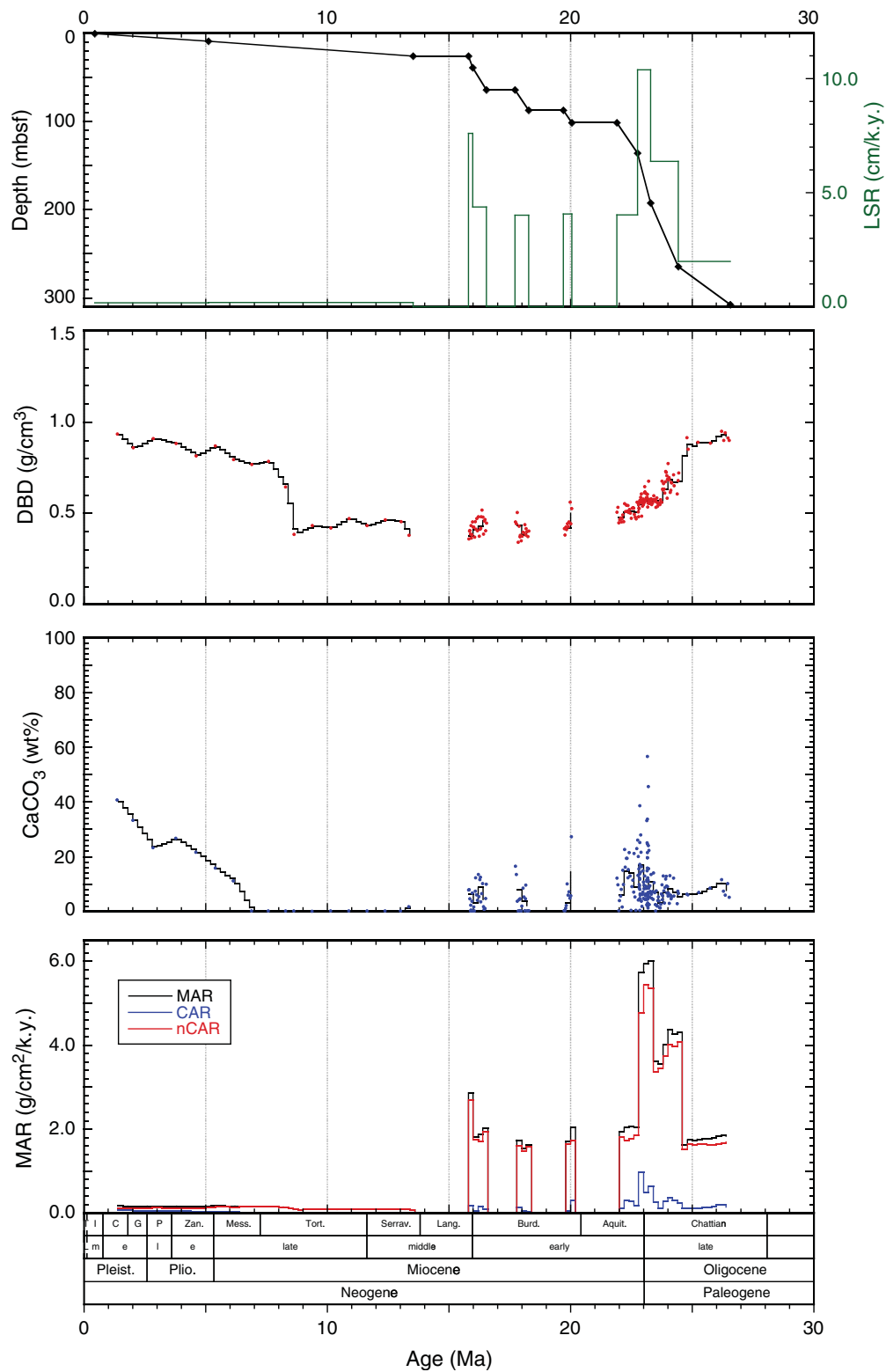


**Figure F31.** Plots of interstitial water constituent concentrations, Hole U1405A. See “[Lithostratigraphy](#)” for description of lithostratigraphic units. IC = ion chromatography.

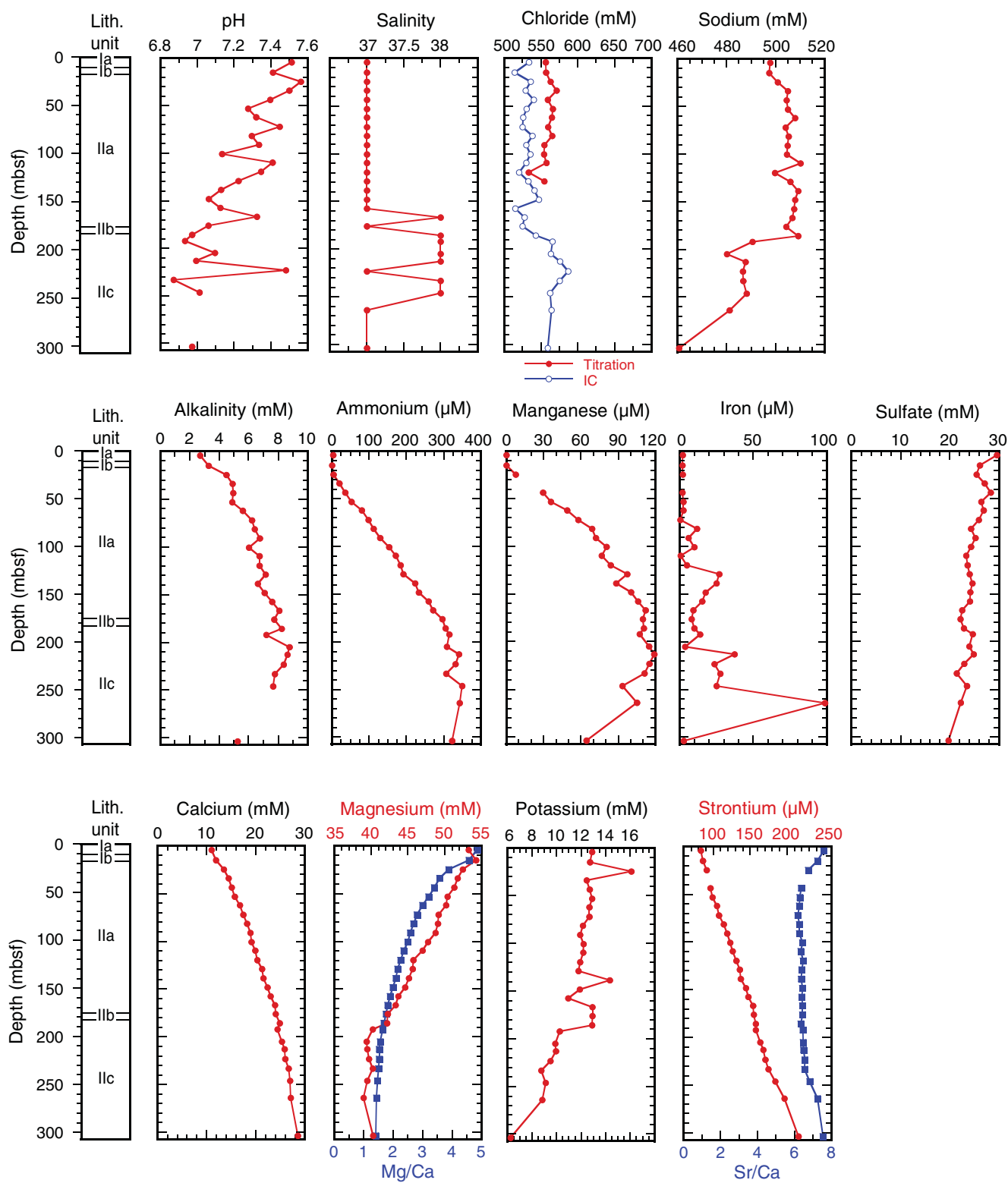


**Figure F32.** Plots of interstitial water calcium and magnesium concentrations and Mg/Ca ratios, Sites U1403–U1405. Distance to volcanic basement is estimated from seismic data.

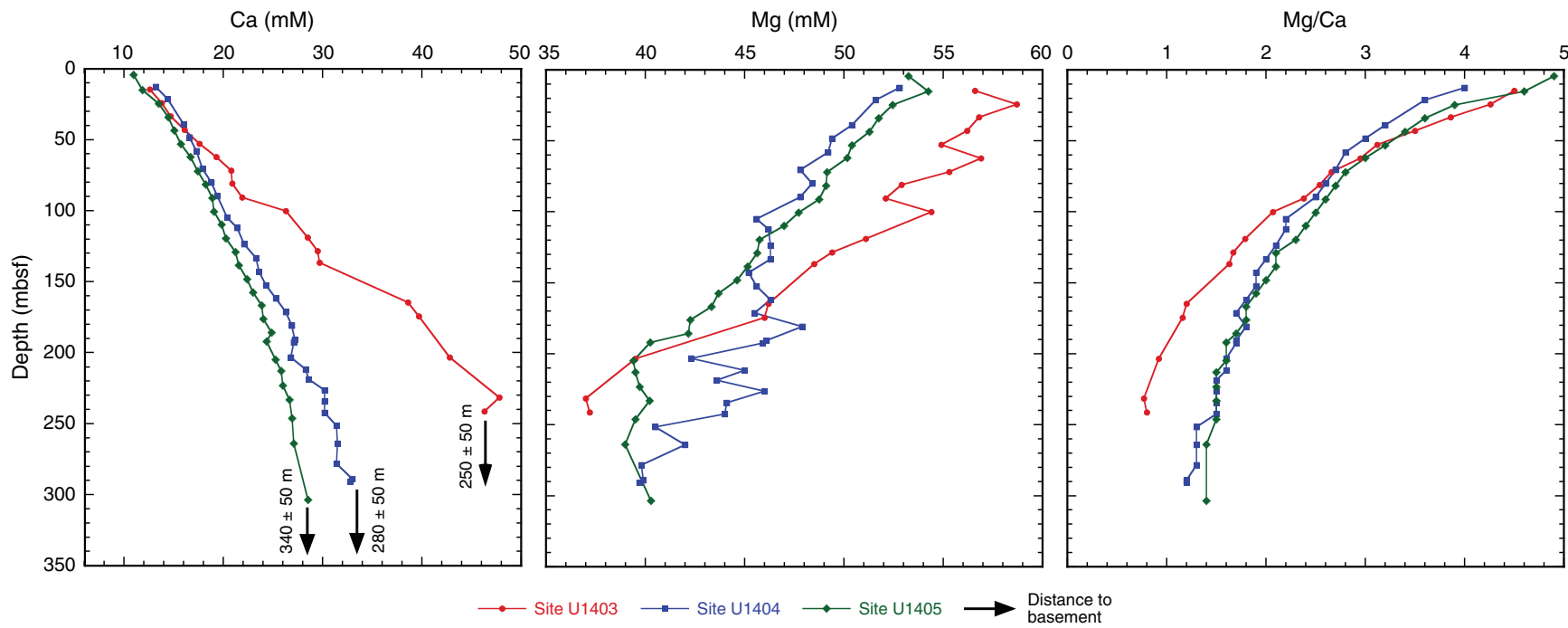


**Figure F33.** Plots of sedimentary carbonate, total organic carbon (TOC), and total nitrogen contents, Hole U1405A. Core recovery: black = recovered, white = not recovered, red = core overlap.

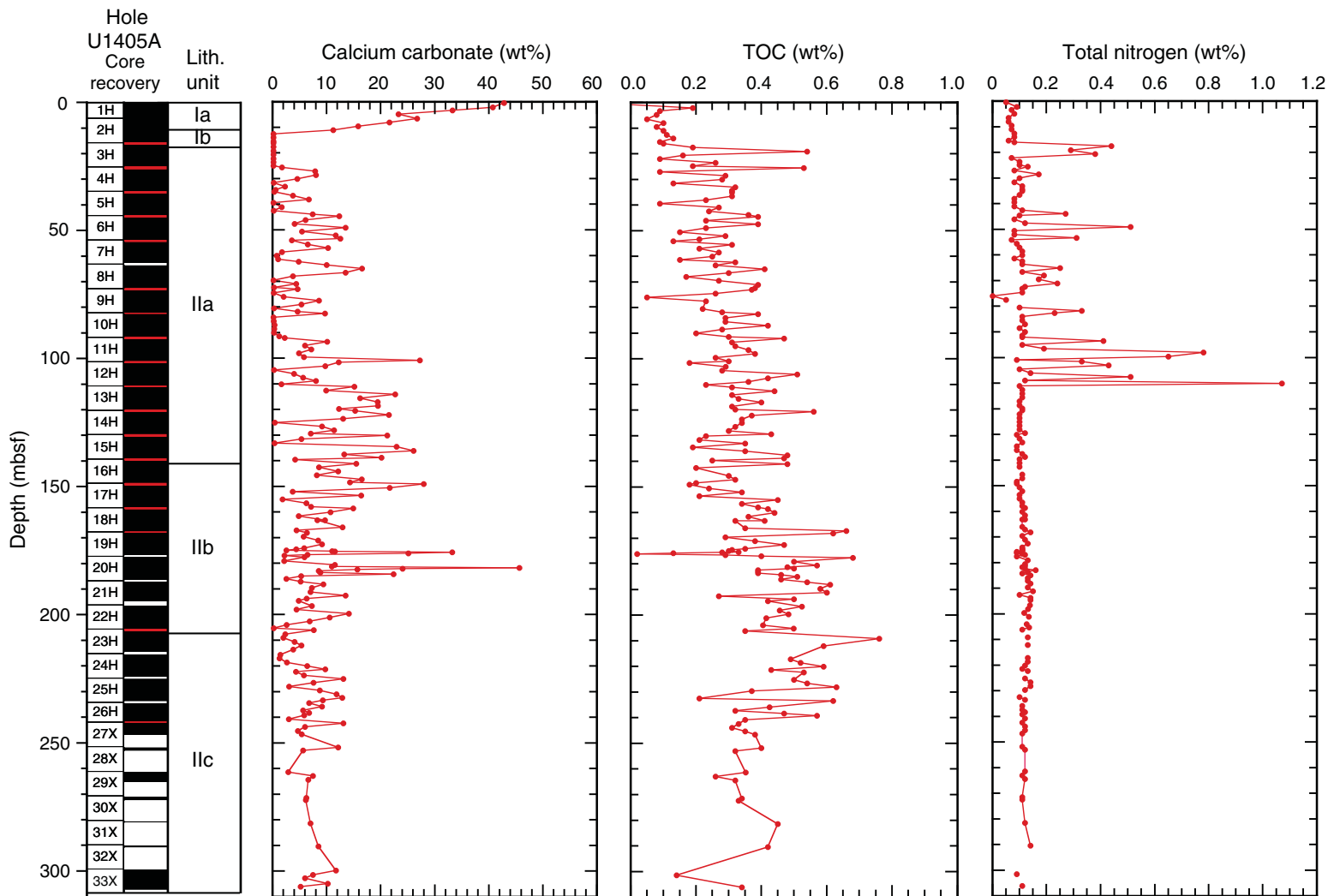


**Figure F34.** Plots of magnetic susceptibility (MS), bulk density (gray line = gamma ray attenuation density from Whole-Round Multisensor Logger, black circles = moisture and density analysis from discrete samples), water content, porosity, and grain density, Site U1405. Core recovery: black = recovered, white = not recovered, red = core overlap. Horizontal gray lines indicate lithostratigraphic unit boundaries (see “[Lithostratigraphy](#)”). APC = advanced piston corer, XCB = extended core barrel.

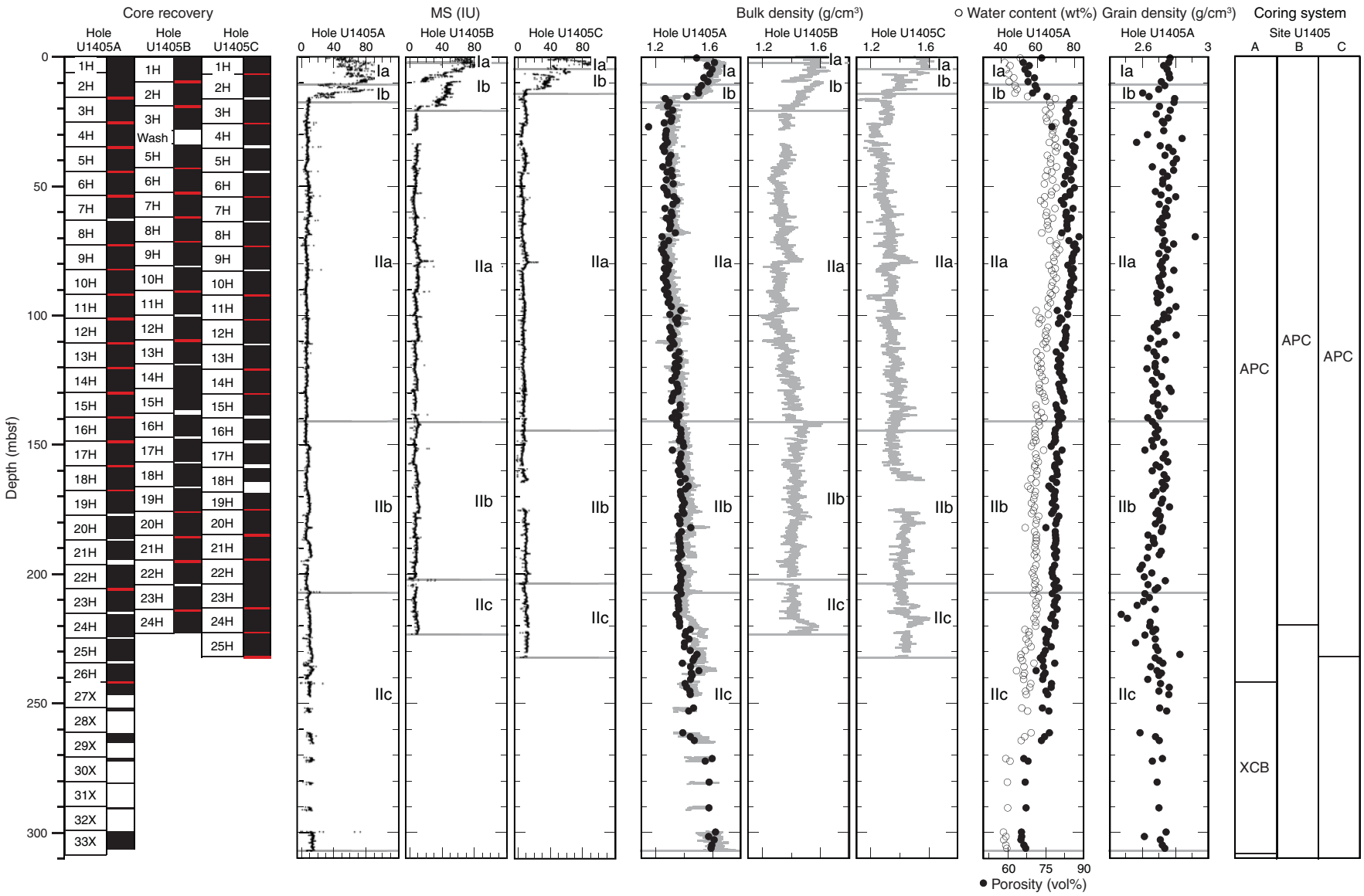




**Figure F35.** Plots of magnetic susceptibility (MS), *P*-wave velocity (gray line = *P*-wave logger data from whole-round sections, black circles = caliper probe data from working section halves), and natural gamma radiation (NGR), Site U1405. Core recovery: black = recovered, white = not recovered, red = core overlap. Horizontal gray lines indicate lithostratigraphic unit boundaries (see “[Lithostratigraphy](#)”). APC = advanced piston corer, XCB = extended core barrel.

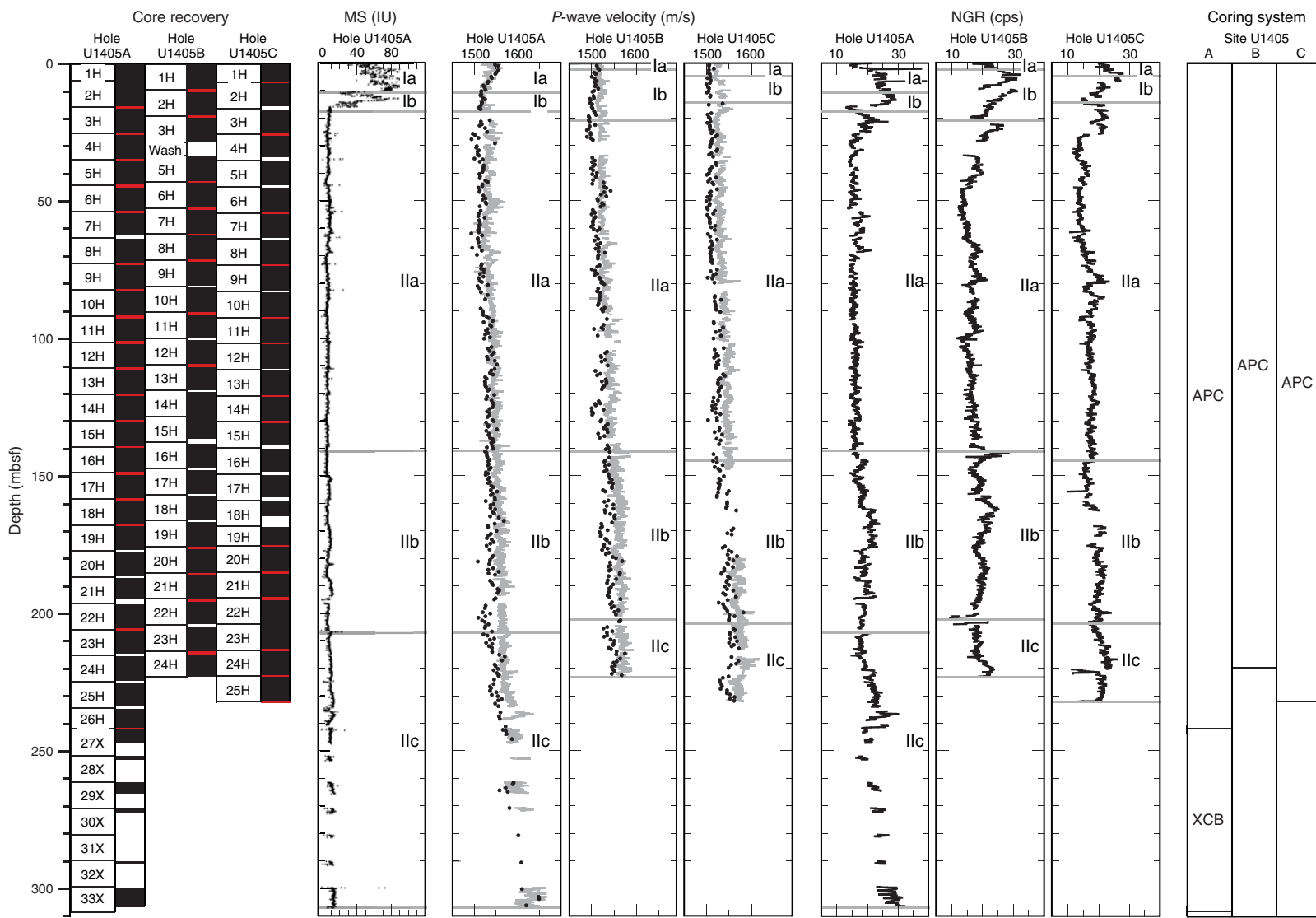


**Figure F36.** Plots of magnetic susceptibility (MS) and color reflectance ( $a^*$ ,  $b^*$ , and  $L^*$ ), Site U1405. Core recovery: black = recovered, white = not recovered, red = core overlap. Horizontal gray lines indicate lithostratigraphic unit boundaries (see “[Lithostratigraphy](#)”). APC = advanced piston corer, XCB = extended core barrel.

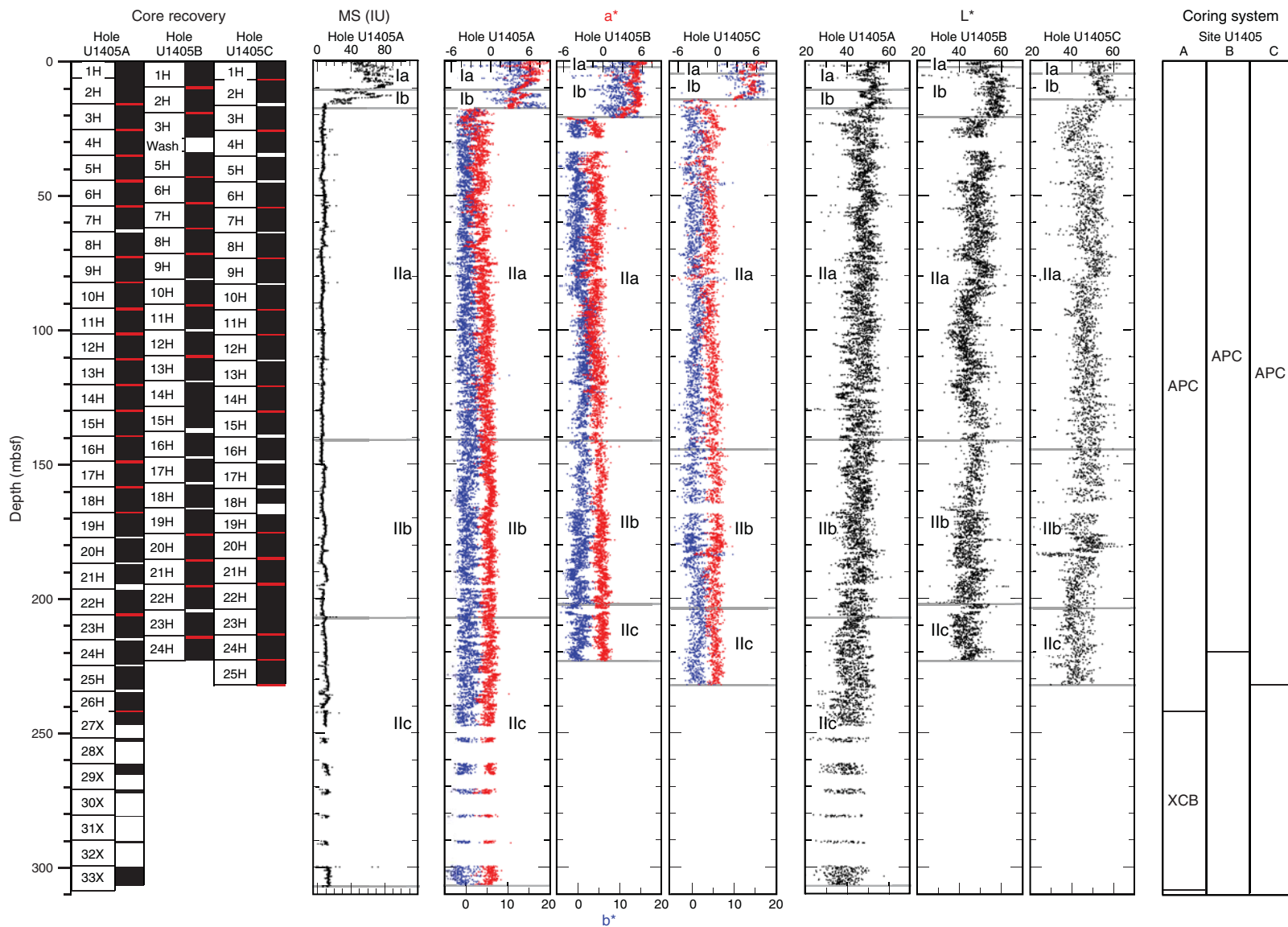


**Figure F37.** Plots of Fe/Ca from XRF core scanning, Site U1405. Top panels show the spliced section for each interval of the scanned splice. Bottom panels show all complete Fe/Ca records. Data from Holes U1405B and U1405C are offset by 20 and 40, respectively, to aid visualization. Open circles indicate core tops. A. 0–50 m CCSF. (Continued on next five pages.)

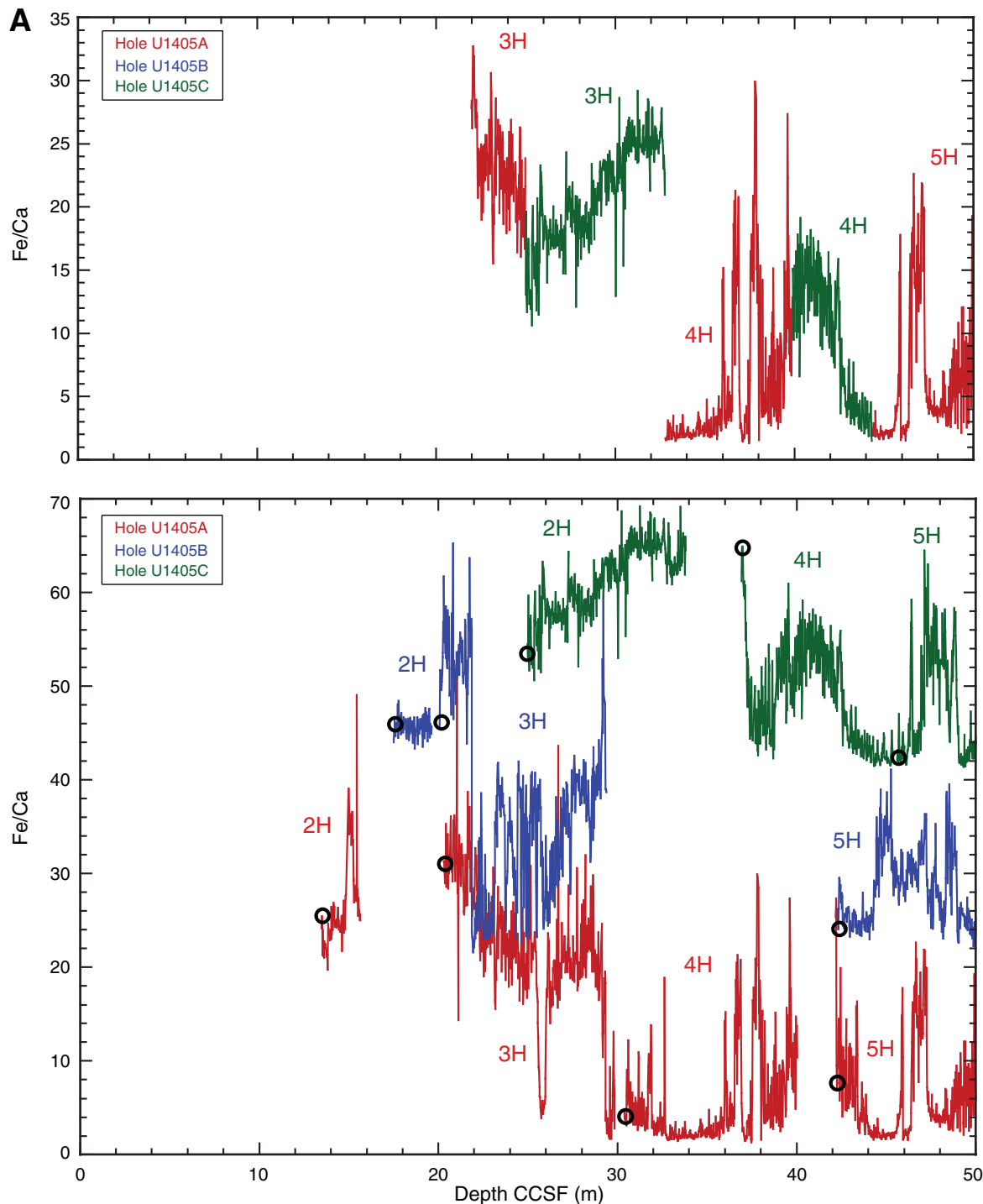


Figure F37 (continued). B. 50–100 m CCSF. (Continued on next page.)

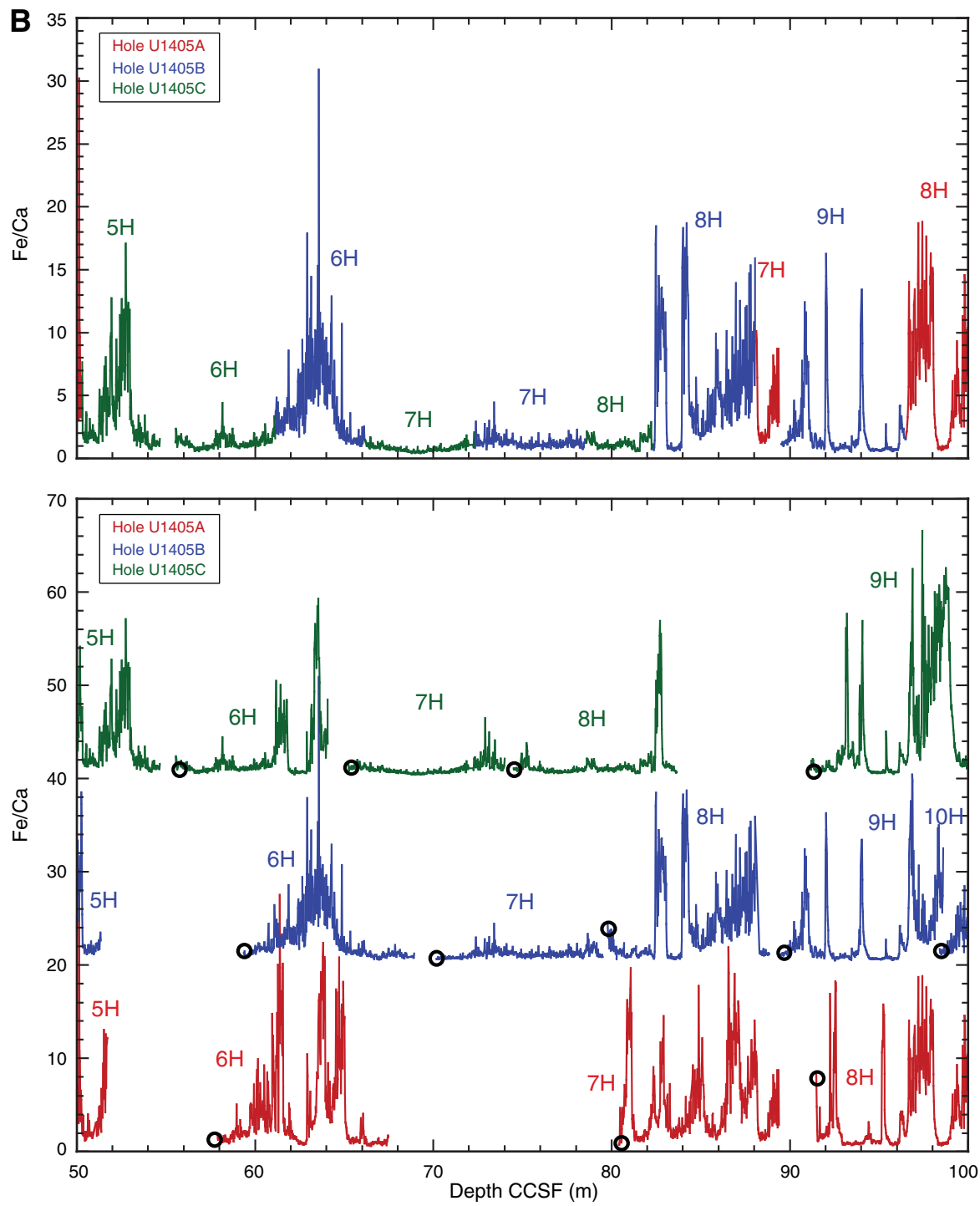


Figure F37 (continued). C. 100–150 m CCSF. (Continued on next page.)

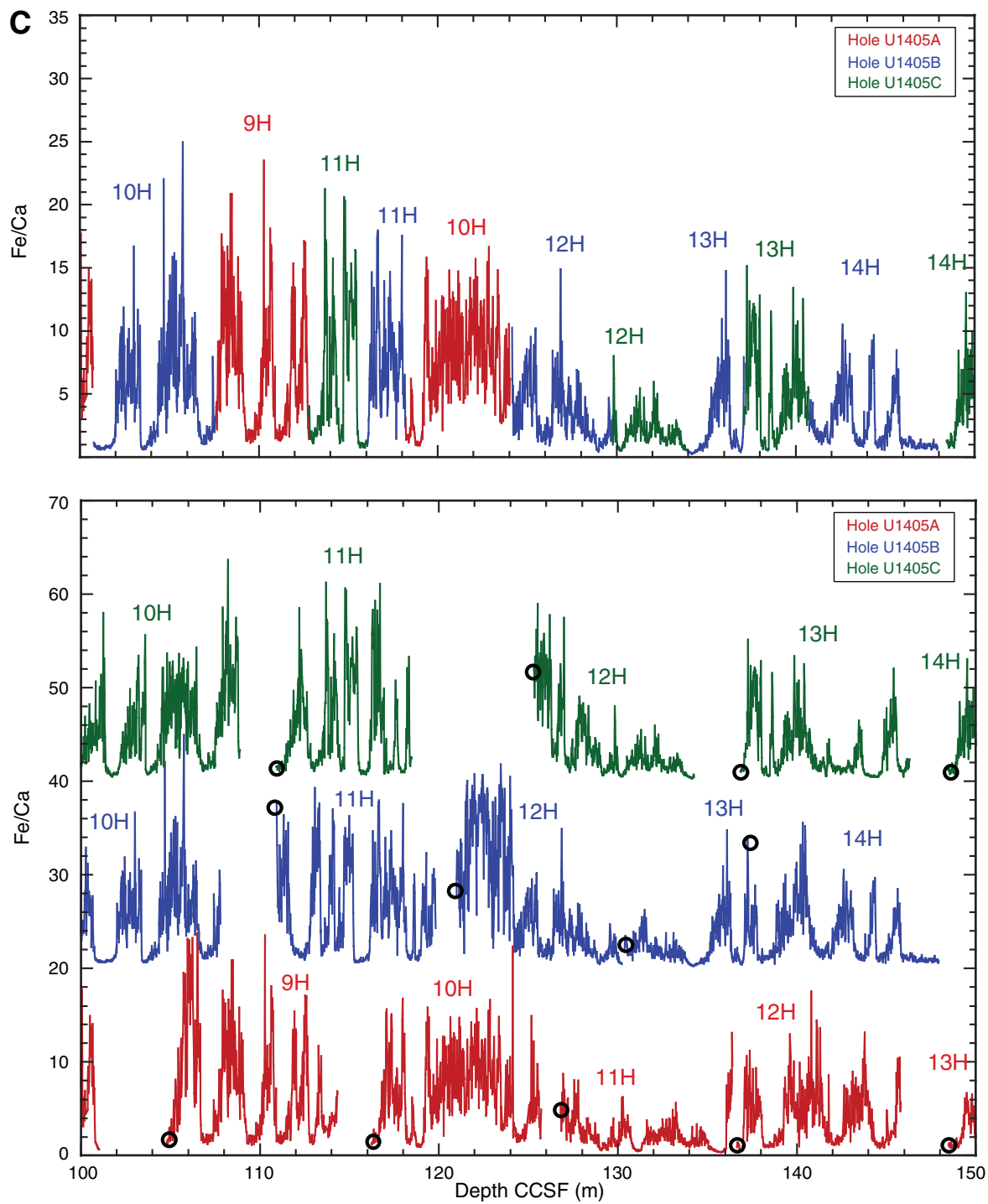


Figure F37 (continued). D. 150–200 m CCSF. (Continued on next page.)

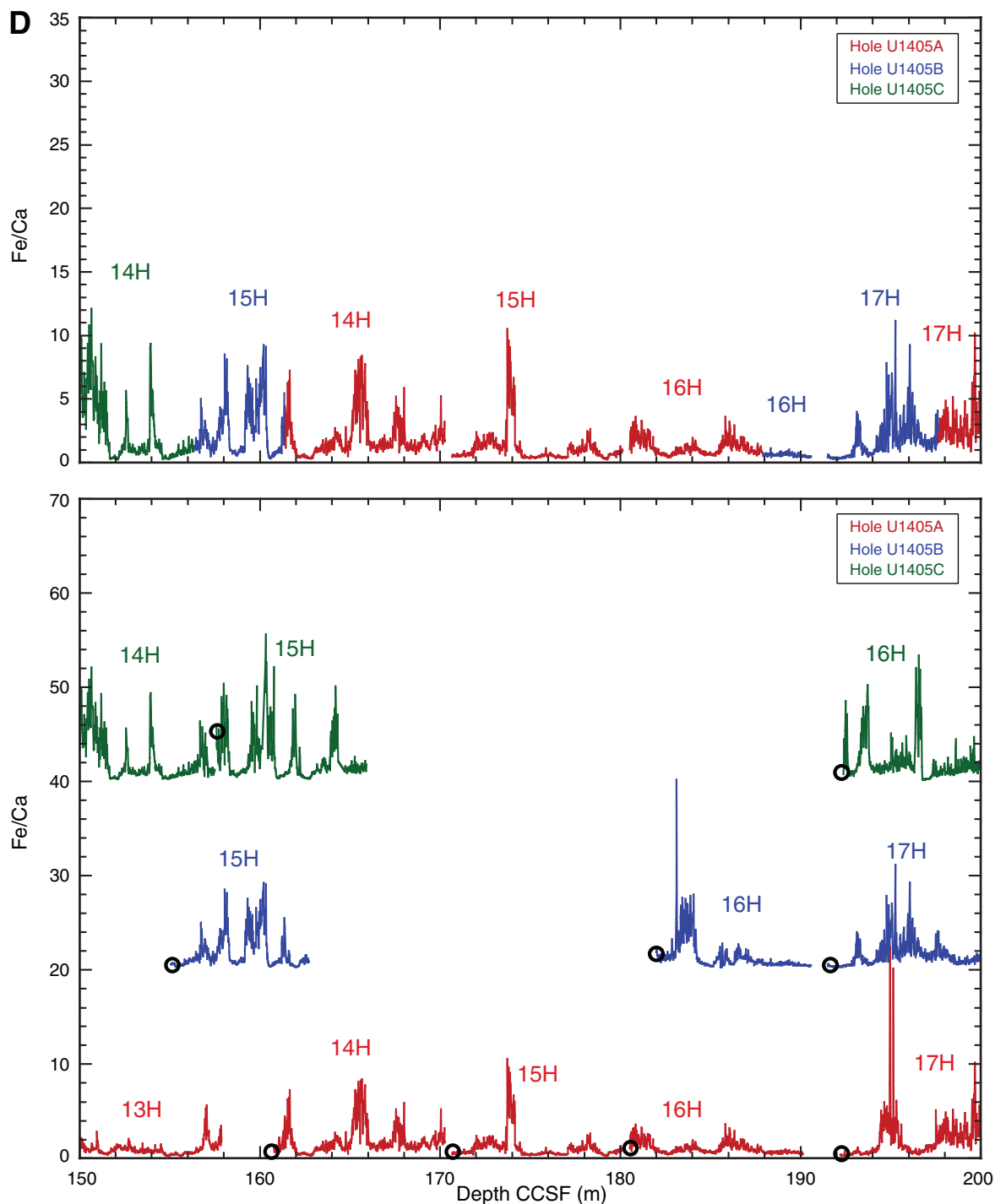


Figure F37 (continued). E. 200–250 m CCSF. (Continued on next page.)

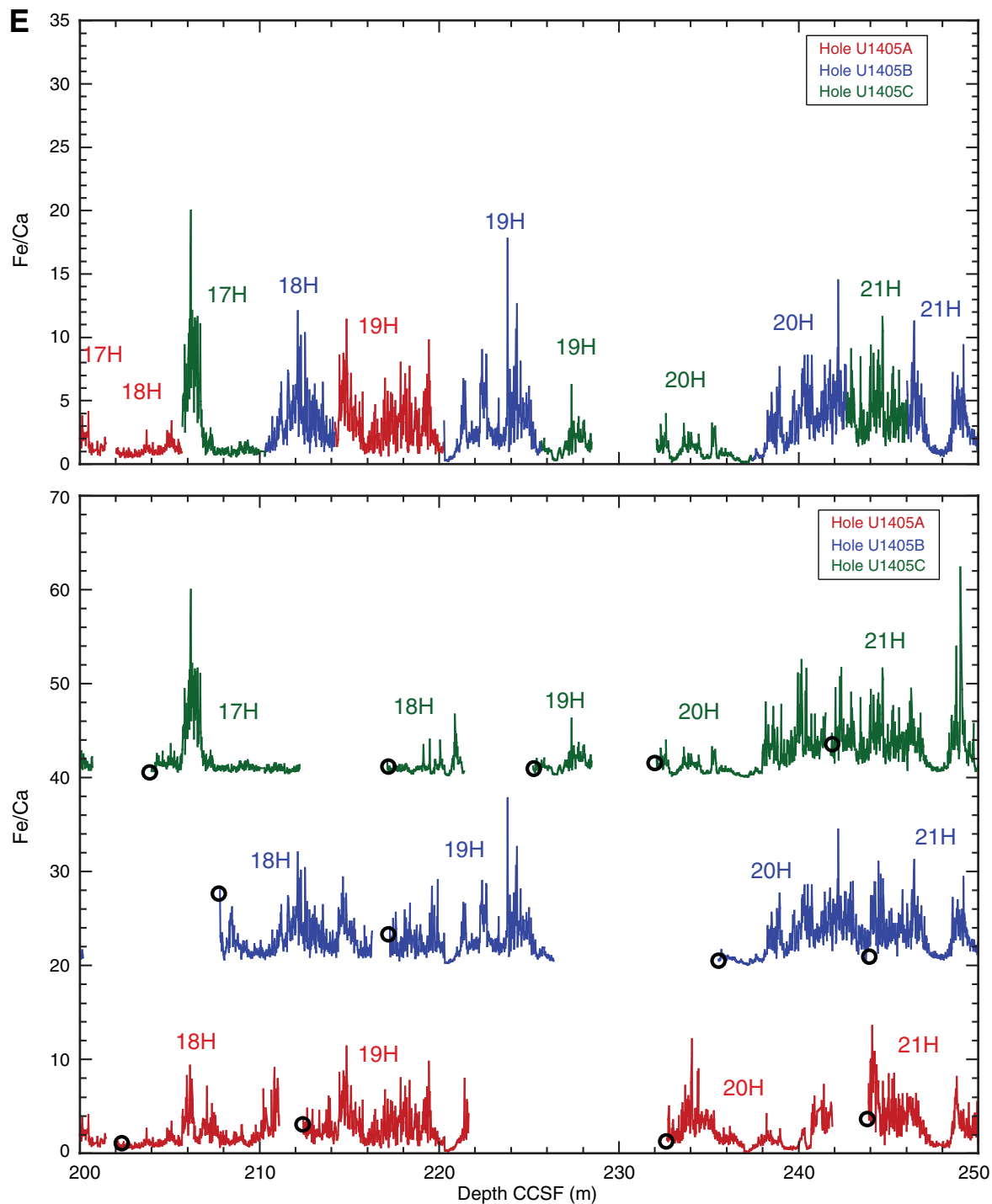
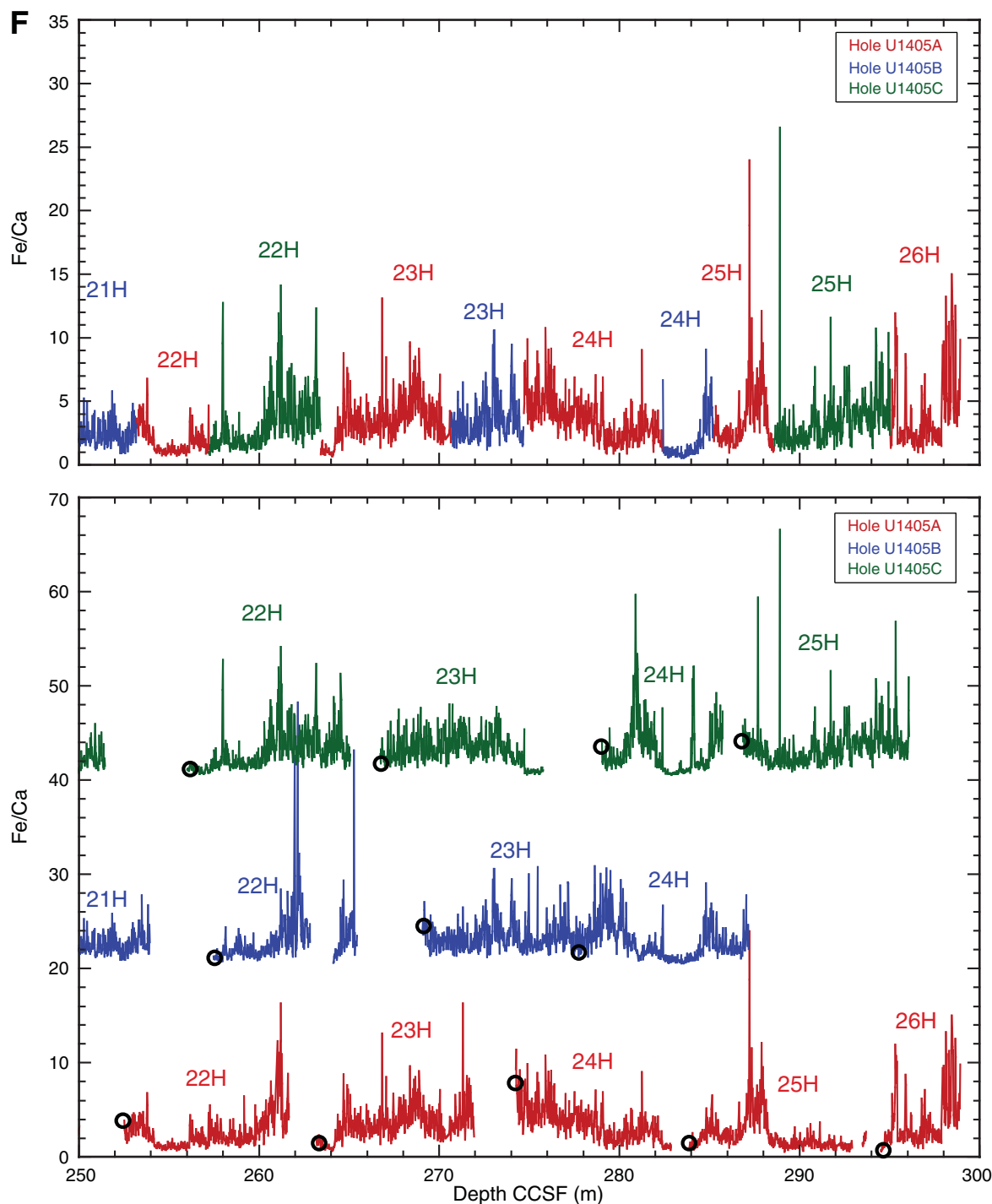


Figure F37 (continued). F. 250–300 m CCSF.



**Figure F38.** Plots of natural gamma radiation (NGR) data, Site U1405. Top panels show the spliced section for each interval of the splice. Bottom panels show all complete NGR records. Data from Holes U1405B and U1405C are offset by 10 and 20 cps, respectively, to aid visualization. Open circles indicate core tops. A. 0–50 m CCSF. (Continued on next six pages.)

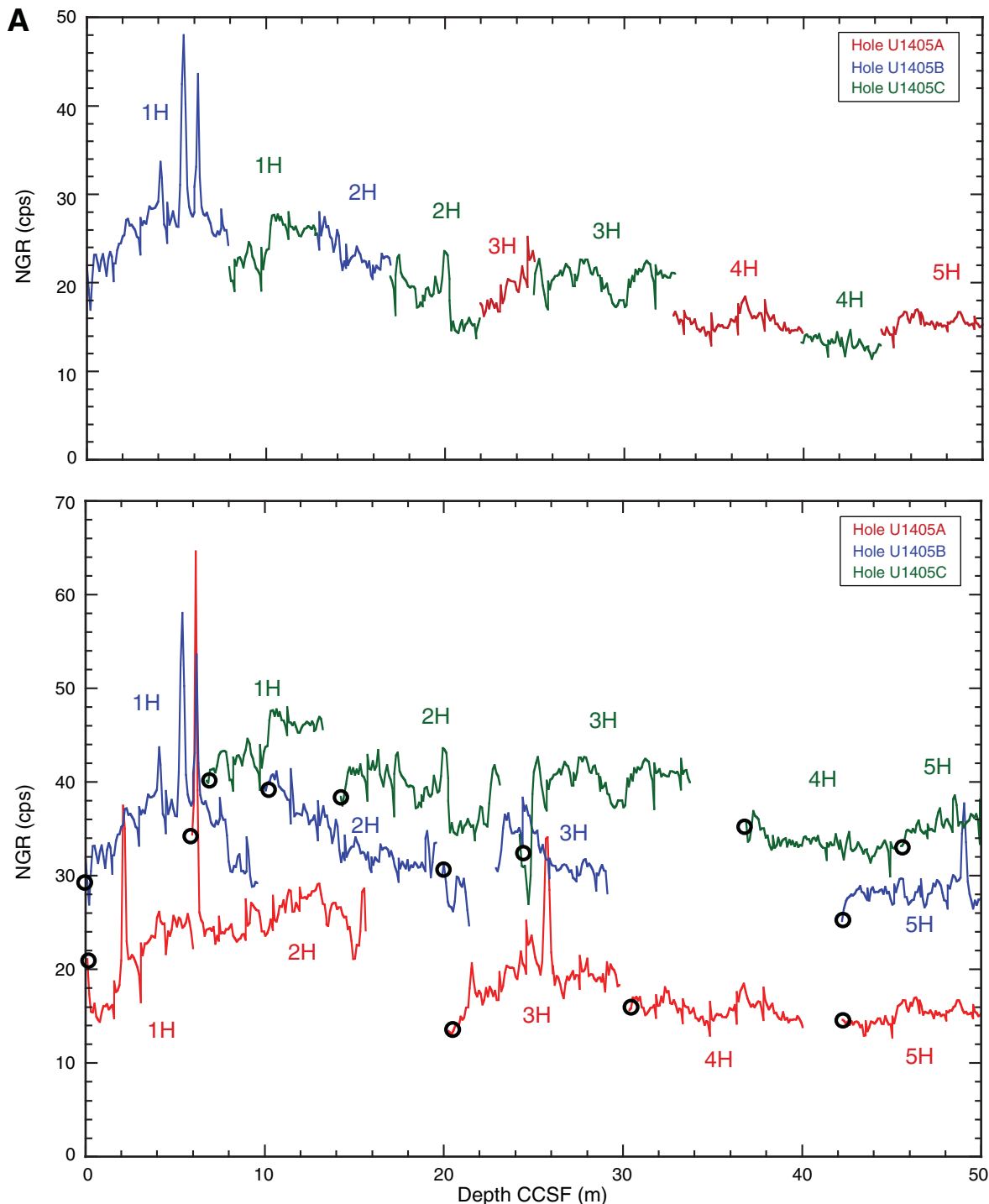


Figure F38 (continued). B. 50–100 m CCSF. (Continued on next page.)

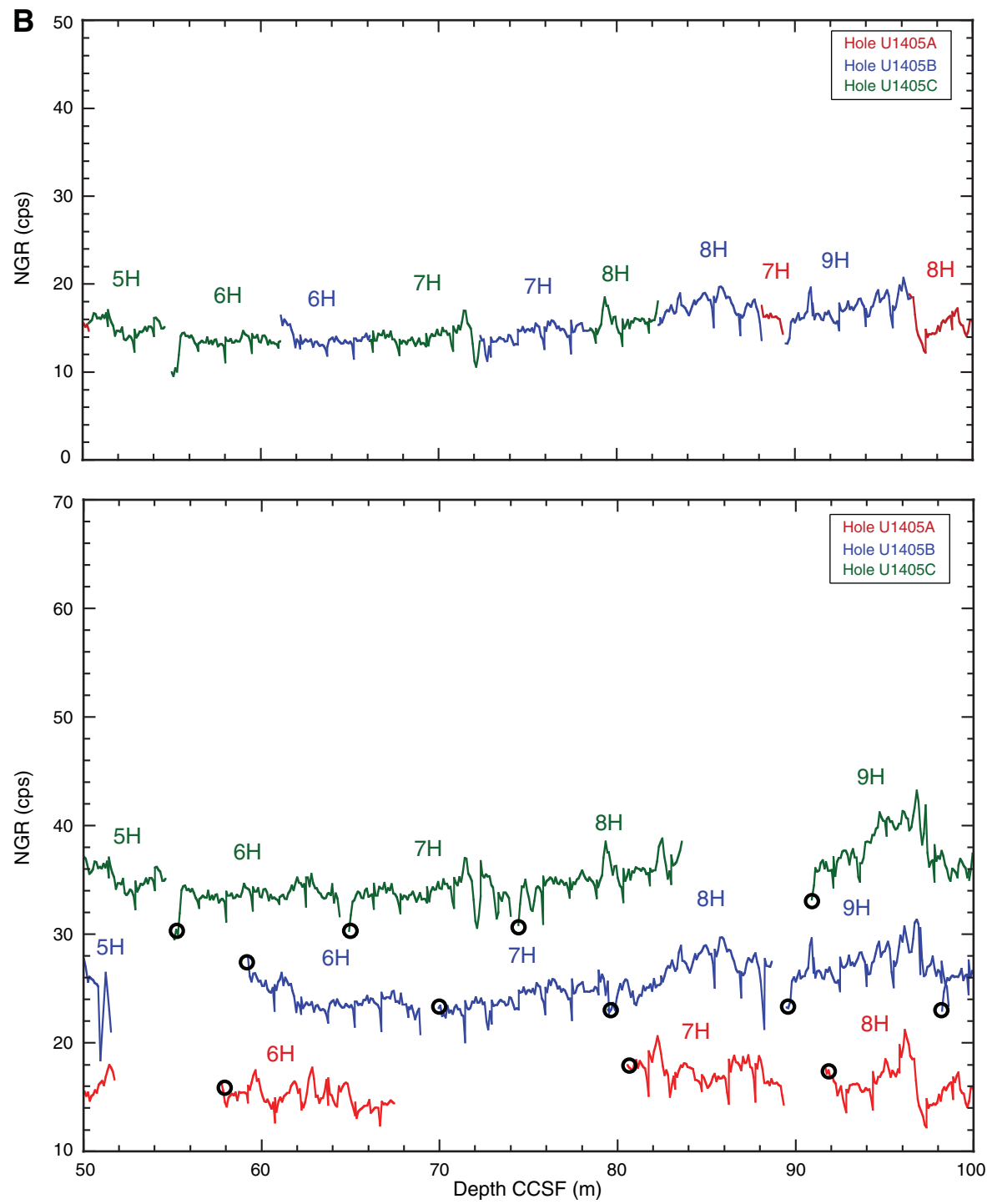


Figure F38 (continued). C. 100–150 m CCSF. (Continued on next page.)

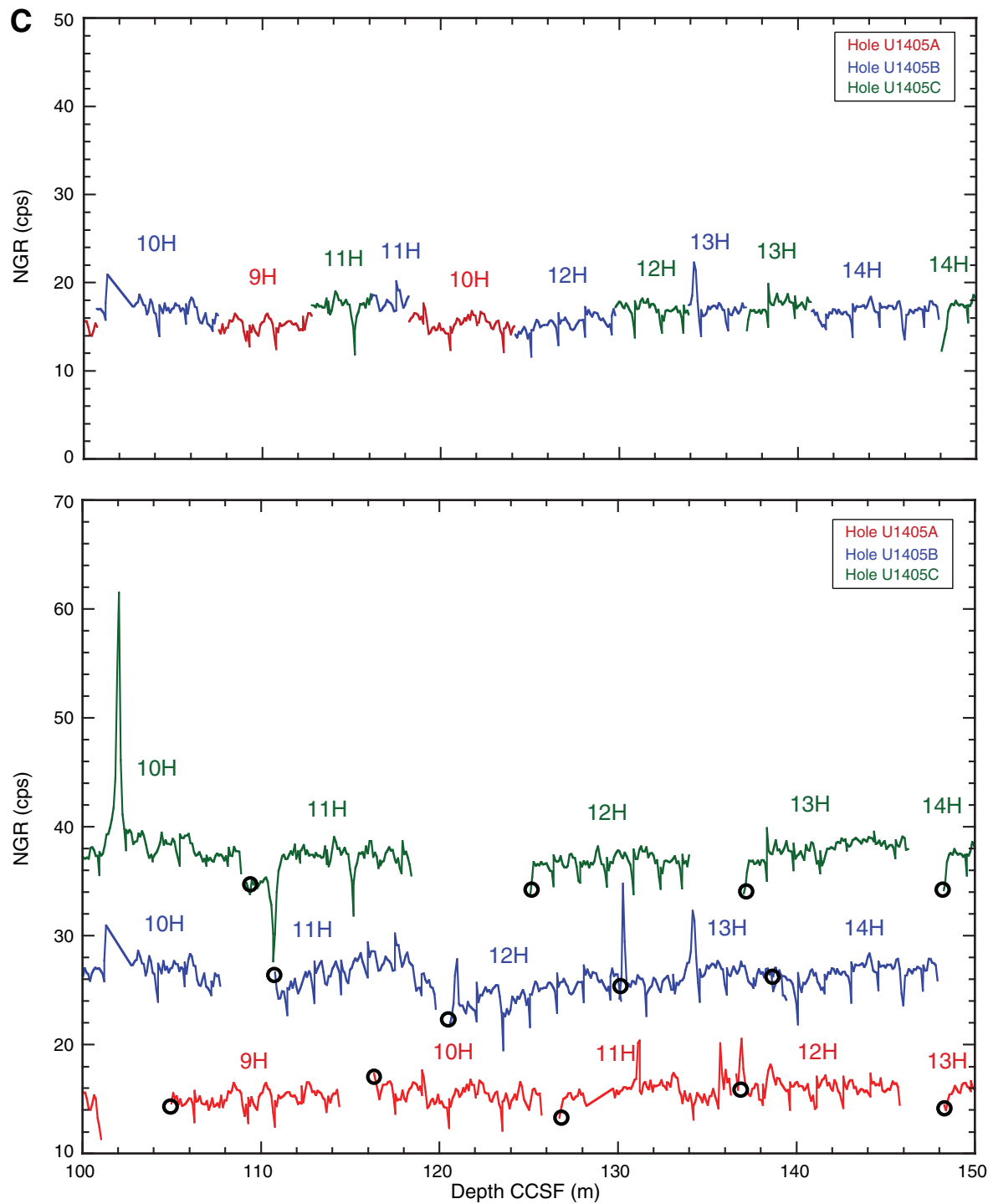


Figure F38 (continued). D. 150–200 m CCSF. (Continued on next page.)

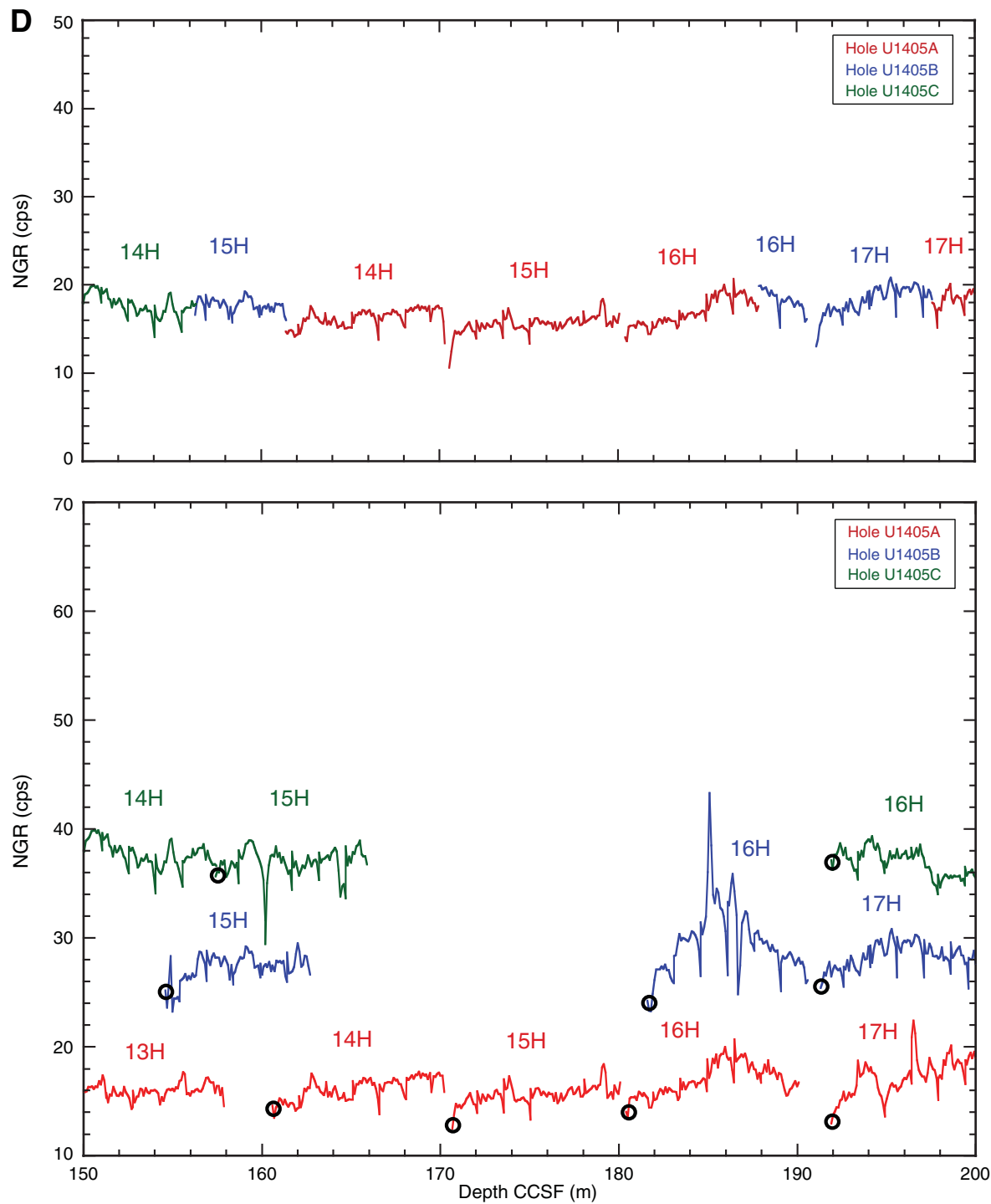


Figure F38 (continued). E. 200–250 m CCSF. (Continued on next page.)

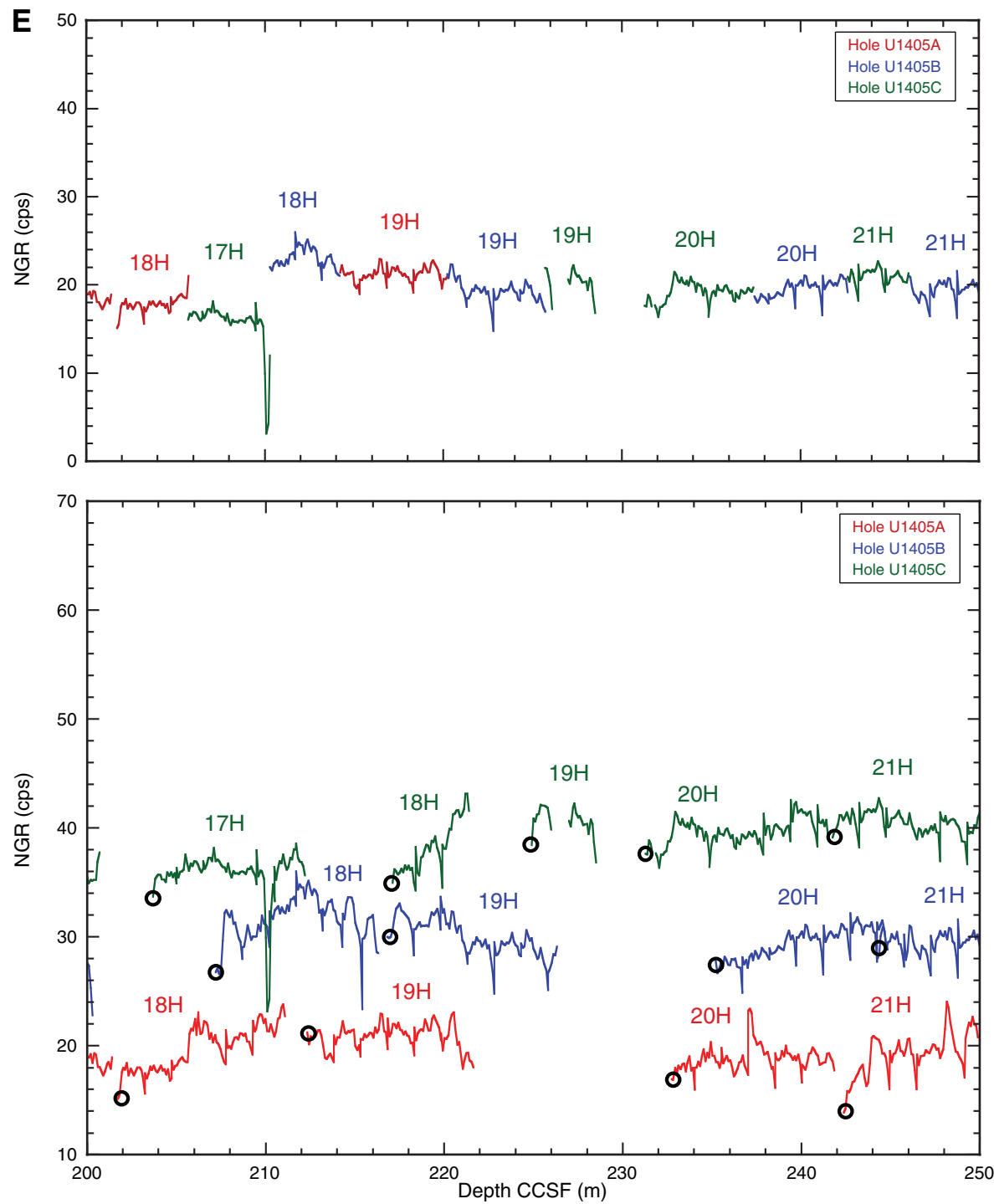
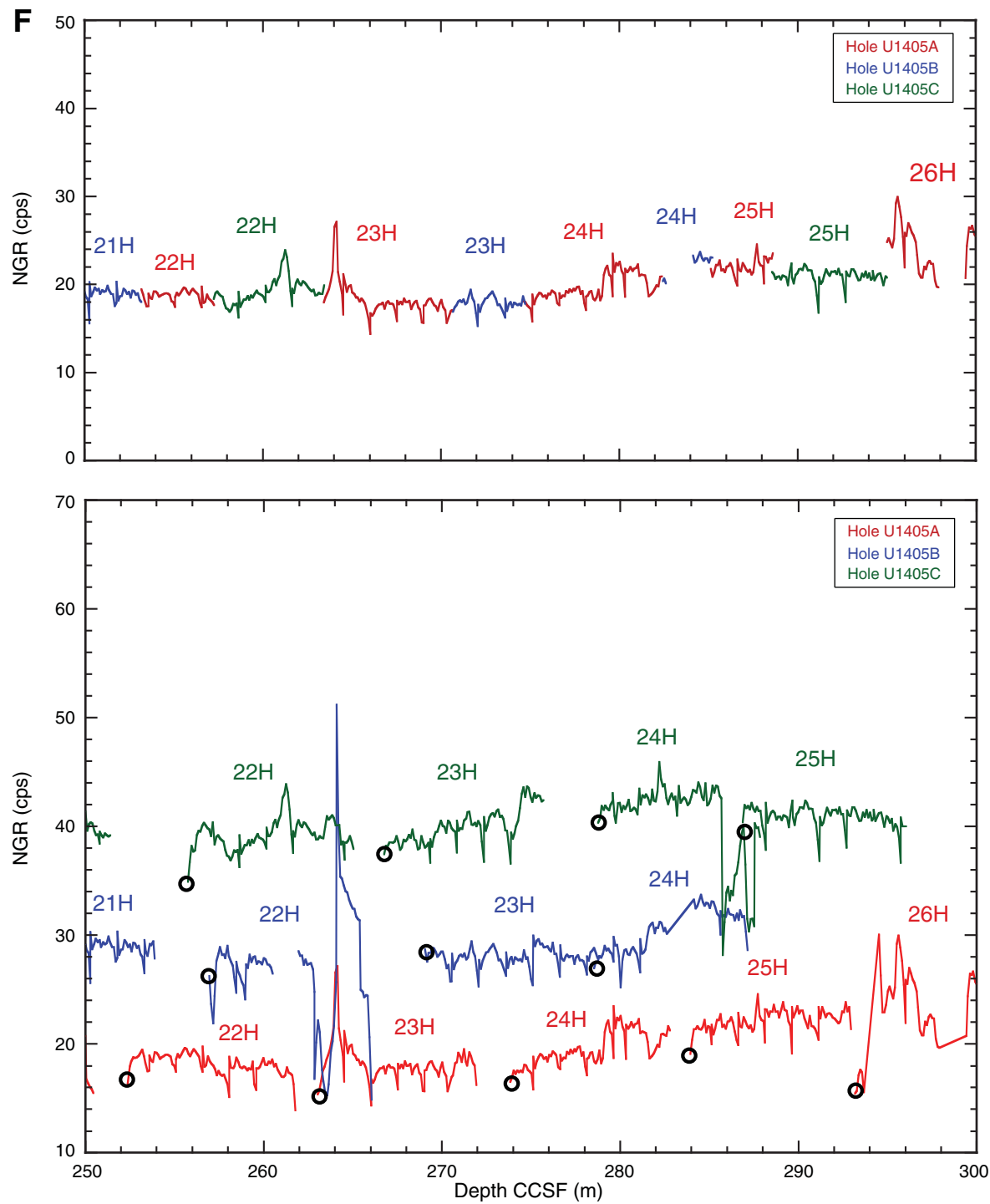
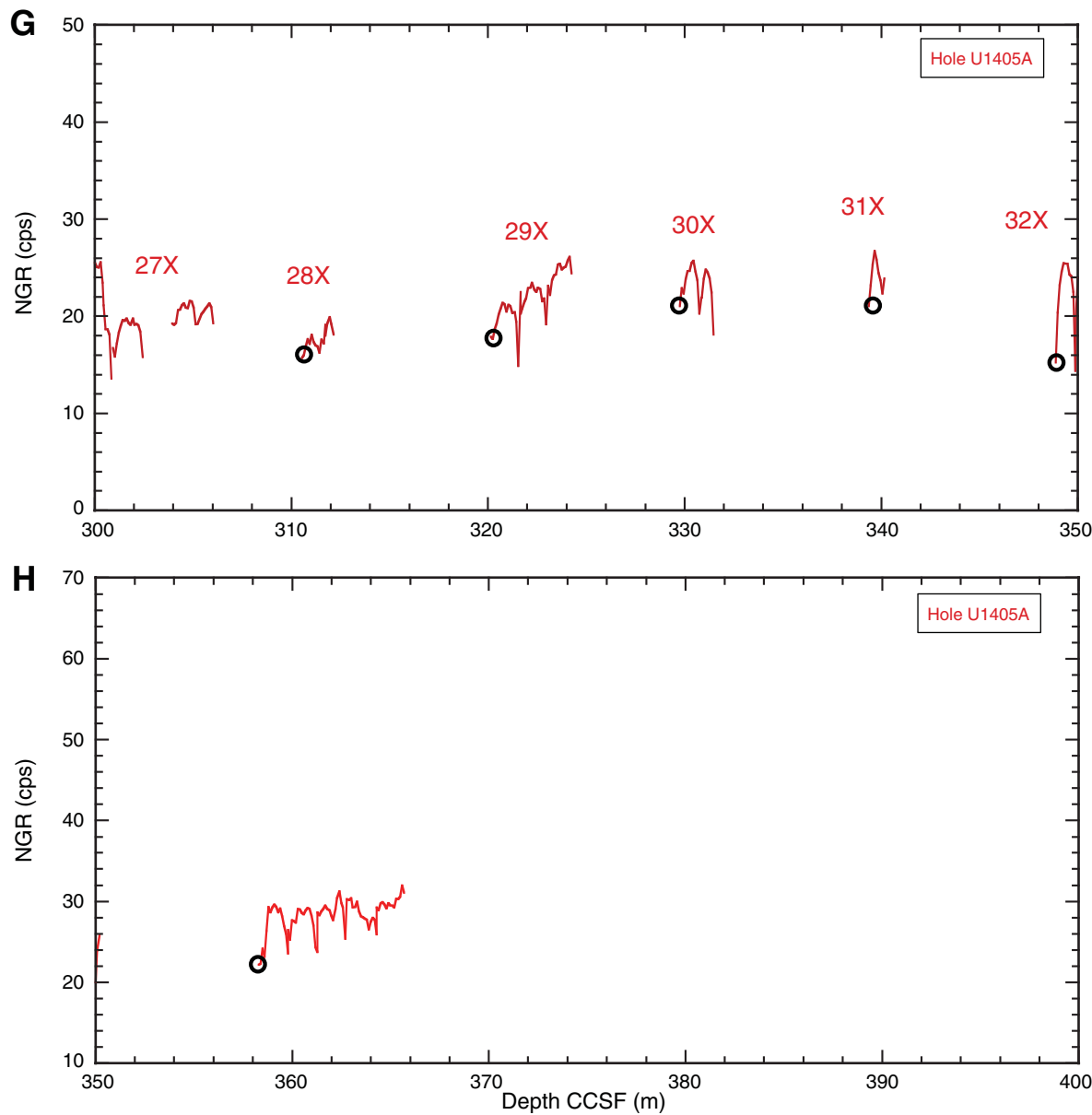
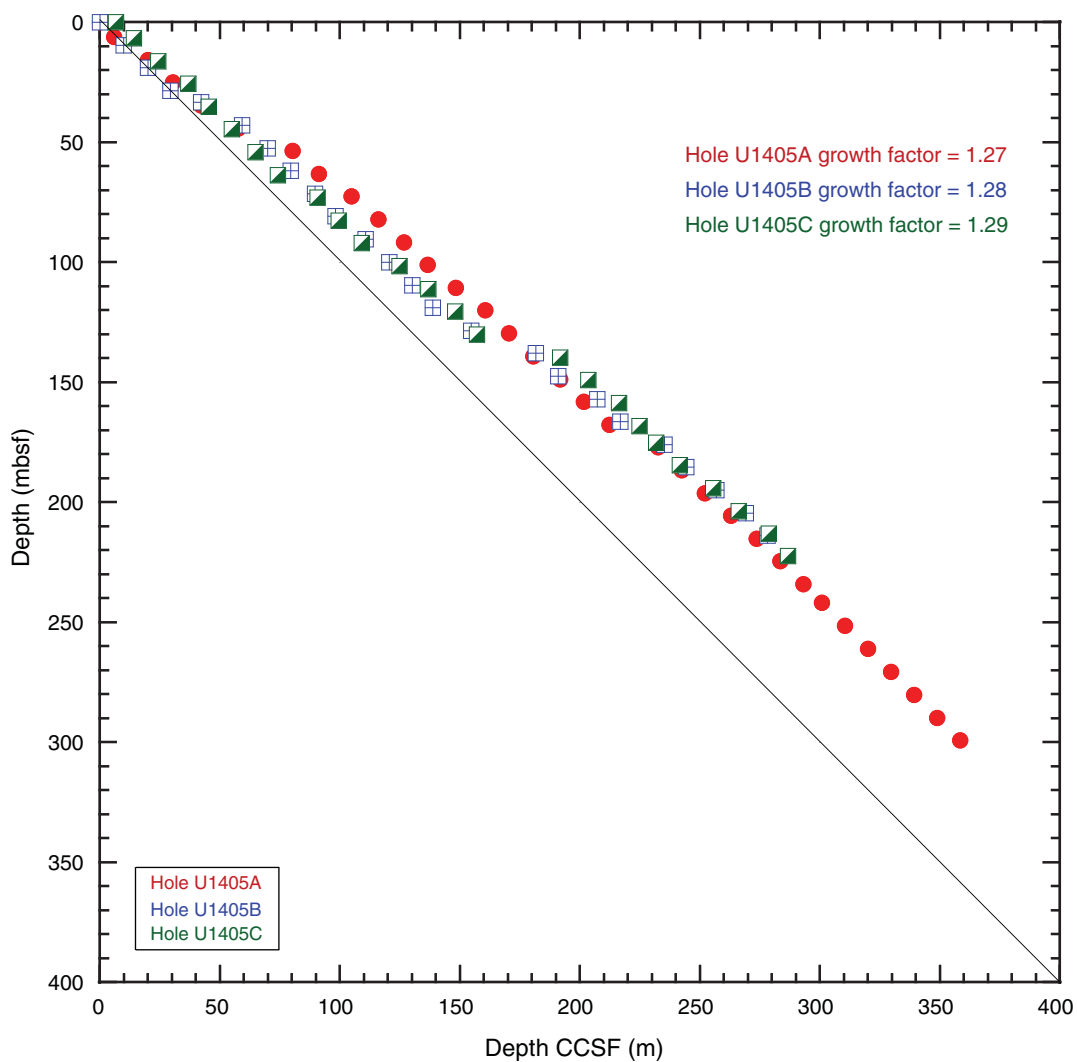


Figure F38 (continued). F. 250–300 m CCSF. (Continued on next page.)



**Figure F38 (continued). G. 300–350 m CCSF. H. 350–400 m CCSF.**

**Figure F39.** Plot of mbsf depth vs. CCSF depth, Site U1405. The growth factor is equal to the slope of the regression line.



**Figure F40.** Plot of identified chron reversal depths vs. age, Site U1405. The broad-scale correlation indicates that chron reversals are in general agreement between the three holes.

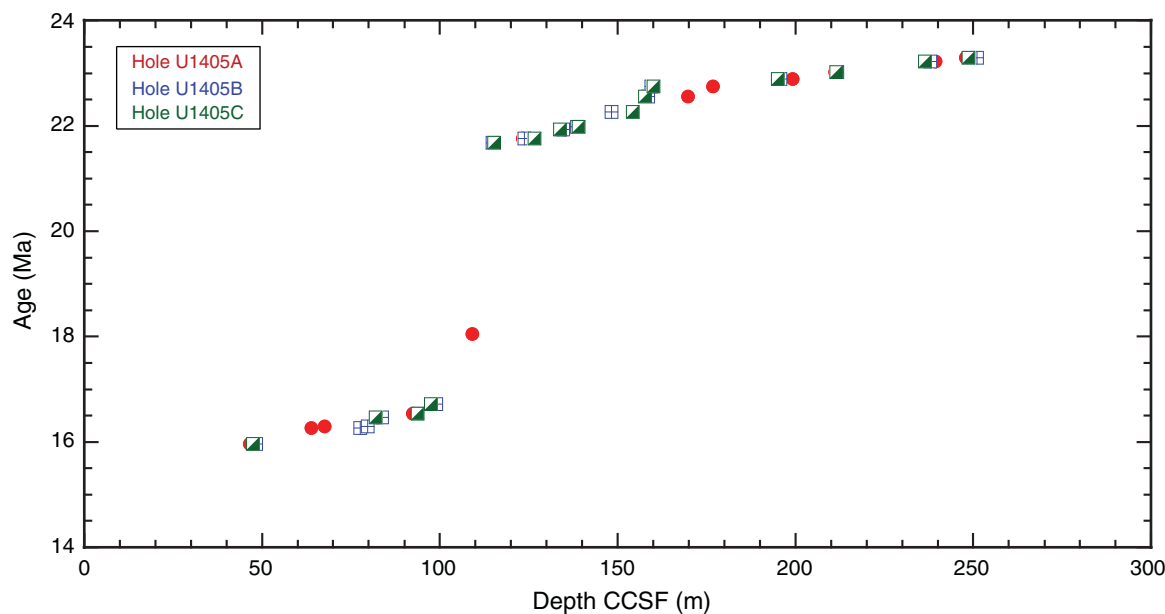


**Table T1.** Coring summary, Site U1405. (Continued on next page.)

Core	Date (2012)	Time UTC (h)	Depth DSF (m)				Depth CSF-A (m)			
			Top of cored interval	Bottom of cored interval	Interval cored (m)	Curated length (m)	Top of core	Bottom of core	Recovery (%)	Sections (N)
<b>342-U1405A-</b>										
1H	25 Jun	1430	0.0	6.2	6.2	6.20	0.00	6.20	100	5
2H	25 Jun	1545	6.2	15.7	9.5	9.95	6.20	16.15	105	8
3H	25 Jun	1650	15.7	25.2	9.5	10.04	15.70	25.74	106	8
4H	25 Jun	1820	25.2	34.7	9.5	10.11	25.20	35.31	106	8
5H	25 Jun	1920	34.7	44.2	9.5	9.97	34.70	44.67	105	8
6H	25 Jun	2020	44.2	53.7	9.5	9.96	44.20	54.16	105	8
7H	25 Jun	2130	53.7	63.2	9.5	9.19	53.70	62.89	97	8
8H	25 Jun	2235	63.2	72.7	9.5	9.84	63.20	73.04	104	8
9H	25 Jun	2335	72.7	82.2	9.5	9.61	72.70	82.31	101	8
10H	26 Jun	0055	82.2	91.7	9.5	10.01	82.20	92.21	105	8
11H	26 Jun	0200	91.7	101.2	9.5	9.95	91.70	101.65	105	8
12H	26 Jun	0300	101.2	110.7	9.5	9.67	101.20	110.87	102	8
13H	26 Jun	0400	110.7	120.2	9.5	9.81	110.70	120.51	103	8
14H	26 Jun	0500	120.2	129.7	9.5	9.97	120.20	130.17	105	8
15H	26 Jun	0600	129.7	139.2	9.5	9.84	129.70	139.54	104	8
16H	26 Jun	0655	139.2	148.7	9.5	10.05	139.20	149.25	106	8
17H	26 Jun	0755	148.7	158.2	9.5	9.81	148.70	158.51	103	8
18H	26 Jun	0855	158.2	167.7	9.5	9.56	158.20	167.76	101	8
19H	26 Jun	0955	167.7	177.2	9.5	9.37	167.70	177.07	99	8
20H	26 Jun	1100	177.2	186.7	9.5	9.45	177.20	186.65	99	8
21H	26 Jun	1155	186.7	196.2	9.5	8.25	186.70	194.95	87	7
22H	26 Jun	1315	196.2	205.7	9.5	9.94	196.20	206.14	105	8
23H	26 Jun	1415	205.7	215.2	9.5	9.15	205.70	214.85	96	7
24H	26 Jun	1515	215.2	224.7	9.5	9.41	215.20	224.61	99	8
25H	26 Jun	1615	224.7	234.2	9.5	9.37	224.70	234.07	99	7
26H	26 Jun	1720	234.2	241.9	7.7	7.74	234.20	241.94	101	8
27X	26 Jun	2055	241.9	251.5	9.6	5.27	241.90	247.17	55	5
28X	26 Jun	2255	251.5	261.1	9.6	1.93	251.50	253.43	20	3
29X	27 Jun	0110	261.1	270.7	9.6	4.49	261.10	265.59	47	4
30X	27 Jun	0400	270.7	280.3	9.6	2.06	270.70	272.76	21	3
31X	27 Jun	0635	280.3	289.8	9.5	1.15	280.30	281.45	12	2
32X	27 Jun	0930	289.8	299.2	9.4	1.39	289.80	291.19	15	2
33X	27 Jun	1140	299.2	308.6	9.4	7.83	299.20	307.03	83	6
Totals:			308.6	308.6	270.34			88	227	
<b>342-U1405B-</b>										
1H	27 Jun	1600	0.0	9.5	9.5	9.96	0.00	9.96	105	8
2H	27 Jun	1745	9.5	19.0	9.5	9.93	9.50	19.43	105	8
3H	27 Jun	2005	19.0	28.5	9.5	9.49	19.00	28.49	100	7
4H	27 Jun	2030					****Drilled from 28.5 to 33.5 m DSF****			
5H	27 Jun	2110	33.5	43.0	9.5	9.56	33.50	43.06	101	8
6H	27 Jun	2215	43.0	52.5	9.5	9.89	43.00	52.89	104	8
7H	27 Jun	2310	52.5	62.0	9.5	9.76	52.50	62.26	103	8
8H	28 Jun	0010	62.0	71.5	9.5	9.62	62.00	71.62	101	8
9H	28 Jun	0110	71.5	81.0	9.5	9.45	71.50	80.95	99	7
10H	28 Jun	0235	81.0	90.5	9.5	9.84	81.00	90.84	104	8
11H	28 Jun	0335	90.5	100.0	9.5	9.36	90.50	99.86	99	8
12H	28 Jun	425	100.0	109.5	9.5	9.93	100.00	109.93	105	8
13H	28 Jun	0520	109.5	119.0	9.5	9.47	109.50	118.97	100	8
14H	28 Jun	0615	119.0	128.5	9.5	9.50	119.00	128.5	100	8
15H	28 Jun	0715	128.5	138.0	9.5	8.33	128.50	136.83	88	7
16H	28 Jun	0805	138.0	147.5	9.5	9.13	138.00	147.13	96	7
17H	28 Jun	0910	147.5	157.0	9.5	9.31	147.50	156.81	98	8
18H	28 Jun	1005	157.0	166.5	9.5	9.34	157.00	166.34	98	8
19H	28 Jun	1100	166.5	176.0	9.5	9.63	166.50	176.13	101	7
20H	28 Jun	1200	176.0	185.5	9.5	9.80	176.00	185.80	103	8
21H	28 Jun	1255	185.5	195.0	9.5	9.93	185.50	195.43	105	8
22H	28 Jun	1400	195.0	204.5	9.5	9.09	195.00	204.09	96	8
23H	28 Jun	1550	204.5	214.0	9.5	9.96	204.50	214.46	105	8
24H	28 Jun	1645	214.0	223.5	9.5	9.33	214.00	223.33	98	7
Totals:			223.5	223.5	219.61			96	178	
<b>342-U1405C-</b>										
1H	28 Jun	2210	0.0	6.7	6.7	6.71	0.00	6.71	100	6
2H	28 Jun	2320	6.7	16.2	9.5	9.12	6.70	15.82	96	7
3H	29 Jun	0015	16.2	25.7	9.5	9.63	16.20	25.83	101	8
4H	29 Jun	0115	25.7	35.2	9.5	8.67	25.70	34.37	91	8

**Table T1 (continued).**

Core	Date (2012)	Time UTC (h)	Depth DSF (m)				Depth CSF-A (m)			
			Top of cored interval	Bottom of cored interval	Interval cored (m)	Curated length (m)	Top of core	Bottom of core	Recovery (%)	Sections (N)
5H	29 Jun	0215	35.2	44.7	9.5	9.23	35.20	44.43	97	8
6H	29 Jun	0310	44.7	54.2	9.5	9.54	44.70	54.24	100	8
7H	29 Jun	0400	54.2	63.7	9.5	9.42	54.20	63.62	99	8
8H	29 Jun	0455	63.7	73.2	9.5	9.60	63.70	73.30	101	8
9H	29 Jun	0550	73.2	82.7	9.5	9.49	73.20	82.69	100	8
10H	29 Jun	0650	82.7	92.2	9.5	9.73	82.70	92.43	102	8
11H	29 Jun	0745	92.2	101.7	9.5	9.61	92.20	101.81	101	8
12H	29 Jun	0855	101.7	111.2	9.5	9.48	101.70	111.18	100	7
13H	29 Jun	1005	111.2	120.7	9.5	9.76	111.20	120.96	103	8
14H	29 Jun	1110	120.7	130.2	9.5	9.75	120.70	130.45	103	8
15H	29 Jun	1215	130.2	139.7	9.5	8.92	130.20	139.12	94	7
16H	29 Jun	1315	139.7	149.2	9.5	8.87	139.70	148.57	93	6
17H	29 Jun	1455	149.2	158.7	9.5	8.81	149.20	158.01	93	8
18H	29 Jun	1605	158.7	168.2	9.5	6.05	158.70	164.75	64	6
19H	29 Jun	1815	168.2	175.2	7.0	7.04	168.20	175.24	101	6
20H	29 Jun	2020	175.2	184.7	9.5	9.99	175.20	185.19	105	8
21H	29 Jun	2120	184.7	194.2	9.5	9.99	184.70	194.69	105	8
22H	29 Jun	2225	194.2	203.7	9.5	9.50	194.20	203.70	100	7
23H	29 Jun	2320	203.7	213.2	9.5	9.70	203.70	213.40	102	8
24H	30 Jun	0040	213.2	222.5	9.3	9.31	213.20	222.51	100	9
25H	30 Jun	0230	222.5	232.0	9.5	9.85	222.50	232.35	104	8
Totals:				232	227.77				98	189
Site U1405 totals:				764.1	717.72				94	367

DSF = drilling depth below seafloor, CSF-A = core depth below seafloor, method A. H = advanced piston core, X = extended core barrel core, numeric core type = drilled interval.

**Table T2.** Lithostratigraphic unit intervals, Site U1405.

Lith. unit	Core, section, interval (cm)		Depth (mbsf)	
	Top	Bottom	Top	Bottom
	342-U1405A-	342-U1405A-		
Ia	1H-1, 0	2H-4, 0	0.00	10.70
Ib	2H-4, 0	3H-2, 30	10.70	17.51
IIa	3H-2, 30	16H-2, 20	17.51	140.98
IIb	16H-2, 20	23H-1, 150	140.98	207.20
IIc	23H-2, 0	33X-CC, 40*	207.20	307.03
	342-U1405B-	342-U1405B-		
Ia	1H-1, 0	1H-2, 75	0.00	2.25
Ib	1H-2, 75	3H-2, 24	2.25	20.74
IIa	3H-2, 24	16H-3, 20	20.74	141.20
IIb	16H-3, 20	22H-7, 7	141.20	202.20
IIc	22H-7, 7	24H-CC, 28*	202.20	223.30
	342-U1405C-	342-U1405C-		
Ia	1H-1, 0	1H-4, 16	0.00	4.66
Ib	1H-4, 16	2H-6, 14	4.66	14.34
IIa	2H-6, 13	16H-4, 34	14.34	144.54
IIb	16H-4, 34	22H-7, 60	144.54	203.70
IIc	23H-1, 0	25H-CC, 20	203.70	232.35

\* = end of hole.



**Table T3.** Calcareous nannofossil datums, Site U1405.

Hole, core, section, interval (cm)		Age	Zone	Marker species	Age (Ma)	Depth (mbsf)			
Top	Bottom					Top	Bottom	Mid-point	±
342-	342-								
		Pliocene–Pleistocene							
U1405A-1H-2, 107	U1405A-1H-1, 107	NN20	T <i>Pseudoemiliania lacunosa</i>	0.44	0.00	1.07	0.54	0.54	
U1405A-1H-3, 107	U1405A-1H-3, 108	NN19	T <i>Discoaster brouweri</i>	1.93	2.57	4.07	3.32	0.75	
U1405A-1H-4, 60	U1405A-1H-4, 60	NN18	T <i>Discoaster pentaradiatus</i>	2.39	4.07	5.10	4.59	0.51	
U1405A-1H-4, 60	U1405A-1H-4, 60	NN17	T <i>Discoaster surculus</i>	2.49	4.07	5.10	4.59	0.51	
U1405A-1H-4, 60	U1405A-1H-4, 120		T <i>Sphenolithus</i> spp.	3.54	5.10	5.70	5.40	0.30	
U1405A-1H-4, 60	U1405A-1H-4, 120	NN16	T <i>Reticulofenestra pseudoumbilicus</i>	3.70	5.10	5.70	5.40	0.30	
U1405A-1H-4, 120	U1405A-1H-CC		T <i>Amaurolithus</i> spp.	3.92	5.70	6.18	5.94	0.24	
U1405A-1H-CC	U1405A-2H-4, 120	NN13	B <i>Ceratolithus rugosus</i>	5.12	6.18	11.90	9.04	2.86	
		Miocene							
U1405A-3H-CC	U1405A-4H-1, 100	NN6	T <i>Sphenolithus heteromorphus</i>	13.53	25.72	26.20	25.96	0.24	
U1405A-3H-CC	U1405A-4H-1, 100		Tc <i>Discoaster deflandrei</i>	15.80	25.72	26.20	25.96	0.24	
U1405A-7H-CC	U1405A-8H-2 110		Bc <i>Sphenolithus heteromorphus</i>	17.71	62.88	65.83	64.36	1.47	
U1405A-7H-CC	U1405A-8H-2 110	NN4	Tc <i>Sphenolithus belemnos</i>	17.95	62.88	65.83	64.36	1.47	
U1405A-9H-CC	U1405A-10H-CC	NN3	T <i>Triquetrorhabdulus carinatus</i>	18.28	82.31	92.19	87.25	4.94	
U1405A-8H-CC	U1405A-9H-CC		B <i>Sphenolithus belemnos</i>	19.03	73.02	82.31	77.66	4.65	
U1405A-15H-CC	U1405A-16H-4, 100	NN2	B? <i>Sphenolithus disbelemnos</i>	22.76	139.50	144.74	142.12	2.62	
U1405A-17H-CC	U1405A-18H-4, 10*		B <i>Discoaster druggii</i>	22.82	158.48	162.83	160.66	2.18	
U1405A-19H-5, 80*	U1405A-19H-6, 16	Oligocene/Miocene boundary	T <i>Sphenolithus capricornutus</i>	22.97	174.50	175.36	174.93	0.43	
U1405A-19H-6, 16	U1405A-19H-6, 46		T <i>Sphenolithus delphix</i>	23.11	175.36	175.66	175.51	0.15	
U1405A-19H-6, 46	U1405A-19H-6, 56		T <i>Dictyococcites bisectus</i> (>10 µm)	23.13	175.66	176.76	176.21	0.55	
U1405A-22H-4, 110	U1405A-22H-CC	Oligocene	B <i>Sphenolithus delphix</i>	23.21	198.80	201.80	200.30	1.50	
U1405A-29H-2, 93	U1405A-29H-CC	NN1	T <i>Sphenolithus ciperoensis</i>	24.43	263.53	265.57	264.55	1.02	
U1405A-33H-CC	U1405A-33H-CC		Bc? <i>Triquetrorhabdulus carinatus</i>	26.57	307.14	307.14	307.14	0.00	

\* = barren sample. B = base, Bc = Base common, T = top, Tc = top common. ? = uncertainty.

**Table T4.** Nannofossil distribution, Site U1405. This table is available in an [oversized format](#).

**Table T5.** Radiolarian datums, Site U1405.

Core, section		Age	Zone	Marker species	Age (Ma)	Depth (mbsf)			
Top	Bottom					Top	Bottom	Mid-point	±
342-U1405A-	342-U1405A-								
		Miocene							
4H-CC				T <i>Carpocanopsis cingulata</i>	17.16	35.29		35.29	
4H-CC	6H-CC		RN4	B <i>Calocyctetta costata</i>	17.59	35.29	54.14	44.72	9.42
6H-CC	10H-CC			B <i>Dorcaspyris dentata</i>	18.22	54.14	92.19	73.17	19.03
6H-CC	10H-CC			X <i>Stichocorys delmontensis</i> – <i>Stichocorys wolffii</i>	18.64	54.14	92.19	73.17	19.03
6H-CC	10H-CC		RN3	T <i>Dorcaspyris ateuchus</i>	18.64	54.14	92.19	73.17	19.03
10H-CC	12H-CC		RN2	T <i>Theocyrtis annosa</i>	20.05	92.19	110.82	101.51	9.31
17H-CC	19H-CC			B <i>Calocyctetta virginis</i>	21.82	158.48	177.05	167.77	9.29
17H-CC	19H-CC		RN1	B <i>Cyrtocapsella tetrapera</i>	21.82	158.48	177.05	167.77	9.29
		Miocene–Oligocene							
22H-CC	24H-CC			B <i>Eucyrtidium diaphanes</i>	23	206.11	224.59	215.35	9.24
20H-CC	22H-CC			T <i>Dorcaspyris papilio</i>	23.59	186.61	206.11	196.36	9.75
24H-CC			RP22	B <i>Lychnocanoma elongata</i>	24.18	224.59		224.59	

B = base, T = top, X = faunal crossover (>50% descendent).



**Table T6.** Radiolarian distribution, Site U1405.

Core, section	Depth (mbsf)	Age (Ma)	Zone		Preservation	Abundance	Diatoms	Forams	Gastropods	Bivalves	Conchostrids	Copepods	Crustaceans	Echinoderm tests	Fish scales	Forams	Gastropods	Invertebrates	Large forams	Molluscs	Nematodes	Opisthontes	Ostracodes	Planktonic forams	Radiolarians	Silicoflagellates	Spiralines	Trilobites	Vibracines	Vertebrates	Whole forams
342-U1405A-4H-CC	35.29	early Miocene	RN4		G	A	R	x	x	x	x	x	x	x	x	x	x	x	x	x	x	x	x	x	x	x	x	x	x	x	
6H-CC	54.14	early Miocene	RN3		G	A	R	x	x	x	x	x	x	x	x	x	x	x	x	x	x	x	x	x	x	x	x	x	x		
10H-CC	92.19	early Miocene	RN2		G	A	R	x	x	x	x	x	x	x	x	x	x	x	x	x	x	x	x	x	x	x	x	x	x		
12H-CC	110.85	early Miocene	RN2		G	A	R	x	x	x	x	x	x	x	x	x	x	x	x	x	x	x	x	x	x	x	x	x	x		
15H-CC	139.50	early Miocene	RN1		G	A	A	x	x	x	x	x	x	x	x	x	x	x	x	x	x	x	x	x	x	x	x	x	x		
17H-CC	158.48	early Miocene	RN1		G	A	A	x	x	?	x	x	x	x	x	x	x	x	x	x	x	x	x	x	x	x	x	x	x		
19H-CC	177.05	Miocene–Oligocene	RP22		G	C	A	x	x	x	x	x	x	x	x	x	x	x	x	x	x	x	x	x	x	x	x	x	x		
20H-CC	186.61	Miocene–Oligocene	RP22		G	A	C	x	x	x	x	x	x	x	x	x	x	x	x	x	x	x	x	x	x	x	x	x	x		
22H-CC	206.11	Miocene–Oligocene	RP22		G	A	F	x	x	x	x	x	x	x	x	x	x	x	x	x	x	x	x	x	x	x	x	x	x		
24H-CC	224.59	Miocene–Oligocene	RP22		G	A	F	x				x	x	x	x	x		x	x	x	x	x	x	x	x	x	x	x	x		

Preservation: G = good. Abundance: A = abundant, C = common, F = few, R = rare. See “[Biostratigraphy](#)” in the “Methods” chapter (Norris et al., 2014a) for preservation and abundance definitions.

Core, section	Depth (mbsf)	Age (Ma)	Zone		Preservation	Abundance	Diatoms	Forams	Gastropods	Bivalves	Conchostrids	Copepods	Crustaceans	Echinoderm tests	Fish scales	Forams	Gastropods	Invertebrates	Large forams	Molluscs	Nematodes	Opisthontes	Ostracodes	Planktonic forams	Radiolarians	Silicoflagellates	Spiralines	Trilobites	Vibracines	Vertebrates	Whole forams
342-U1405A-4H-CC	35.29	early Miocene	RN4		G	A	R	x	x	x	x	x	x	x	x	x	x	x	x	x	x	x	x	x	x	x	x	x	x		
6H-CC	54.14	early Miocene	RN3		G	A	R	x	x	x	x	x	x	x	x	x	x	x	x	x	x	x	x	x	x	x	x	x	x		
10H-CC	92.19	early Miocene	RN2		G	A	R	x	x	x	x	x	x	x	x	x	x	x	x	x	x	x	x	x	x	x	x	x	x		
12H-CC	110.85	early Miocene	RN2		G	A	R	x	x	x	x	x	x	x	x	x	x	x	x	x	x	x	x	x	x	x	x	x	x		
15H-CC	139.50	early Miocene	RN1		G	A	A	x	x	x	x	x	x	x	x	x	x	x	x	x	x	x	x	x	x	x	x	x	x		
17H-CC	158.48	early Miocene	RN1		G	A	A	x	x	x	x	x	x	x	x	x	x	x	x	x	x	x	x	x	x	x	x	x	x		
19H-CC	177.05	Miocene–Oligocene	RP22		G	C	A	x	x	x	x	x	x	x	x	x	x	x	x	x	x	x	x	x	x	x	x	x	x		
20H-CC	186.61	Miocene–Oligocene	RP22		G	A	C	x	x	x	x	x	x	x	x	x	x	x	x	x	x	x	x	x	x	x	x	x	x		
22H-CC	206.11	Miocene–Oligocene	RP22		G	A	F	x	x	x	x	x	x	x	x	x	x	x	x	x	x	x	x	x	x	x	x	x	x		
24H-CC	224.59	Miocene–Oligocene	RP22		G	A	F	x				x	x	x	x	x		x	x	x	x	x	x	x	x	x	x	x	x		

**Table T7.** Planktonic foraminifer datums, Site U1405.

Core, section, interval (cm)	Top	Bottom	Age	Zone/ Subzone	Marker event	Age (Ma)	Depth (mbsf)			
							Top	Bottom	Mid-point	±
342-U1405A-										
5H-6, 110–112	5H-CC		early Miocene	M4b/M5	B <i>Praeorbulina sicana</i>	16.38	43.30	44.62	43.96	0.66
7H-4, 110–112	7H-5, 110–115		early Miocene	M4a/M4b	B <i>Fosella birnagae</i>	16.69	59.30	60.80	60.05	0.75
8H-6, 110–112	8H-CC		early Miocene	M3/M4a	T <i>Catapsydrax dissimilis</i>	17.54	71.80	72.99	72.40	0.59
12H-1, 100–102	12H-3, 100–102		early Miocene	M1b/M2	T <i>Paragloborotalia kugleri</i>	21.12	102.20	105.20	103.70	1.50
17H-CC	18H-2, 110–112		early Miocene	M1a/M1b	B <i>Globoquadrina dehiscens</i>	22.44	158.45	160.80	159.63	1.18
18H-4, 110–112	18H-6, 110–112		early Miocene	O7/M1a	B <i>Paragloborotalia kugleri</i>	22.96	163.83	166.61	165.22	1.39
26H-4, 5–7	26H-CC		late Oligocene	O6/O7	B <i>Paragloborotalia pseudokugleri</i>	25.21	237.09	241.89	239.49	2.40
27X-CC	28X-CC		late Oligocene	O6	B <i>Globigerinoides primordius</i>	26.12	241.89	247.16	244.53	2.64

T = top, B = base.

**Table T8.** Planktonic foraminifer distribution, Hole U1405A. This table is available in an [oversized format](#).**Table T9.** Benthic foraminifer distribution, Site U1405. This table is available in an [oversized format](#).**Table T10.** Benthic foraminifer morphotype distribution, Site U1405.

Core, section, interval (cm)	Depth (mbsf)	Preservation	Abundance	Planktonic Foraminifera	Agglutinated Foraminifera	Trochospira
342-U1405A-						
1H-2, 110–111	2.60	G	P	P P F D P		
1H-4, 116–117	5.67	M	P	P P F D R		
1H-4, 60–61	5.10	G	R	R P R D B		
2H-5, 100–101	13.20	M	P	B P B P B		

Preservation: G = good, M = moderate. Abundance: D = dominant, F = few, R = rare, P = present, B = barren. See “[Biostratigraphy](#)” in the “Methods” chapter (Norris et al., 2014a) for definitions of preservation and abundance.

**Table T11.** Core orientation data, Site U1405.

Hole U1405A		Hole U1405B		Hole U1405C	
Core	MTF (°)	Core	MTF (°)	Core	MTF (°)
342-U1405A-		342-U1405B-		342-U1405C-	
1H	—	1H	320	1H	81
2H	—	2H	88	2H	271
3H	—	3H	274	3H	36
4H	—	4H	33	4H	319
5H	—	5H	110	5H	183
6H	—	6H	160	6H	323
7H	—	7H	82	7H	349
8H	—	8H	82	8H	195
9H	—	9H	64	9H	65
10H	—	10H	209	10H	332
11H	—	11H	205	11H	16
12H	86	12H	152	12H	350
13H	111	13H	137	13H	57
14H	150	14H	248	14H	341
15H	61	15H	197	15H	-21
16H	86	16H	288	16H	38
17H	0	17H	224	17H	300
18H	197	18H	177	18H	313
19H	224	19H	139	19H	40
20H	27	20H	202	20H	356
21H	219	21H	147	21H	88
22H	90	22H	139	22H	140
23H	87	23H	265	23H	227
24H	71	24H	307	24H	198
25H	58			25H	223
26H	289				

MTF = magnetic tool face orientation from geomagnetic north, — = no tool data.

**Table T12.** Summary of AF demagnetization results for discrete samples, Hole U1405A. (Continued on next two pages.)

Core, section, interval (cm)	Depth (mbsf)	Declination 20 mT or PCA (°)	Inclination 20 mT or PCA (°)	PCA MAD (°)	PCA range (mT)	NRM 20 mT (A/m)	Measurement error (%)
342-U1405A-							
1H-2W, 99–101	2.50	120.7	58.4			2.15E-02	5.1
1H-3W, 69–71	3.70	-13.2	-34.5			3.81E-03	6.5
1H-4W, 74–76	5.25	64.6	75.2			4.19E-03	4.0
2H-2W, 74–76	8.45	42.6	33.3			4.65E-03	3.0
2H-4W, 78–80	11.49	210.1	52.4	8.5	20–60	2.69E-03	4.2
2H-6W, 69–71	14.40	36.6	4.0			9.68E-04	3.4
3H-1W, 74–76	16.45	91.0	-49.9			3.58E-05	34.3
3H-3W, 74–76	19.50	146.7	-56.9	19.0	20–60	9.46E-05	9.7
3H-5W, 69–71	22.45	47.9	-13.0			1.73E-05	68.4
4H-2W, 74–76	27.45	84.5	-59.5			1.07E-04	10.4
4H-4W, 74–76	30.45	43.5	-60.7	22.2	10–60	9.21E-05	14.2
4H-6W, 69–71	33.40	141.3	-26.0			1.07E-04	5.8
5H-2W, 75–77	36.96	100.1	-5.6			1.48E-04	1.6
5H-3W, 75–77	38.46	67.8	-9.1			1.14E-04	5.6
5H-4W, 45–47	39.66	149.9	41.0			3.25E-05	33.3
5H-6W, 60–62	42.81	160.4	35.5			3.36E-05	34.4
6H-2W, 85–87	46.56	178.2	45.2			1.31E-04	6.2
6H-4W, 75–77	49.46	216.0	31.9			1.97E-05	64.2
6H-6W, 75–77	52.46	-41.2	-64.5			9.55E-05	16.4
7H-1W, 75–77	54.46	268.1	57.3			3.33E-05	42.2
7H-2W, 75–77	55.96	54.4	-60.1			7.22E-05	16.9
7H-4W, 75–77	58.96	29.9	-45.4			5.73E-05	28.3
7H-6W, 45–47	61.66	45.3	-64.7			9.34E-05	12.9
8H-1W, 75–77	63.96	68.9	3.3			9.01E-05	13.6
8H-2W, 75–77	65.46	63.7	16.5			4.94E-05	20.1
8H-4W, 75–77	68.46	-69.9	44.6			6.58E-05	33.6
8H-5W, 75–77	69.96	69.9	-33.2			8.08E-05	11.4

**Table T12 (continued).** (Continued on next page.)

Core, section, interval (cm)	Depth (mbfs)	Declination 20 mT or PCA (°)	Inclination 20 mT or PCA (°)	PCA MAD (°)	PCA range (mT)	NRM 20 mT (A/m)	Measurement error (%)
8H-6W, 75–77	71.46	58.5	-38.9			4.38E-05	24.1
9H-2W, 75–77	74.96	118.2	-49.4			4.29E-05	19.3
9H-3W, 75–77	76.46	136.3	-27.4			7.17E-06	181.8
9H-4W, 75–77	77.96	-39.9	0.3			1.92E-05	59.9
9H-6W, 70–72	80.91	-38.7	13.9			3.79E-05	35.4
10H-2W, 75–77	84.46	27.5	27.8			4.84E-05	23.5
10H-4W, 75–77	87.46	219.0	-83.0			7.79E-05	18.9
10H-5W, 75–77	88.96	-35.3	-47.8			5.20E-05	35.7
10H-6W, 65–67	90.36	11.5	50.6			6.43E-05	25.1
11H-2W, 75–77	93.96	-52.4	56.9			3.33E-05	54.4
11H-4W, 75–77	96.96	-87.1	60.0			5.14E-05	27.0
11H-6W, 75–77	99.96	-13.6	-11.7			3.47E-06	356.1
11H-7W, 35–37	101.06	25.7	-46.7			7.26E-05	19.3
12H-2W, 74–76	103.45	54.9	19.0			2.70E-05	62.9
12H-4W, 74–76	106.45	43.4	32.4			1.42E-05	103.4
12H-6W, 58–60	109.29	50.1	2.8			1.03E-05	147.6
13H-2W, 74–76	112.95	34.1	31.0			2.78E-05	49.8
13H-4W, 74–76	115.95	33.4	76.5			3.19E-05	53.2
13H-5W, 74–76	117.45	140.0	-50.9			6.60E-05	29.3
14H-1W, 74–76	120.95	139.7	-19.0			5.15E-05	19.4
14H-2W, 74–76	122.45	138.1	-42.5			9.39E-05	18.0
14H-3W, 74–76	123.96	142.8	-47.0			4.67E-05	18.9
14H-4W, 74–76	125.46	145.0	-40.3			5.74E-05	27.1
14H-6W, 74–76	128.48	137.5	-50.8			4.59E-05	31.2
15H-2W, 74–76	131.95	20.0	5.0			3.67E-05	44.5
15H-4W, 74–76	134.95	-15.9	41.6			5.19E-05	25.9
15H-5W, 74–76	136.45	163.7	-16.1			4.36E-05	22.1
15H-6W, 74–76	137.95	123.6	-31.9			5.24E-05	22.0
16H-1W, 74–76	139.95	92.2	-23.4			3.35E-05	48.8
16H-2W, 74–76	141.45	107.2	-47.8			7.75E-05	17.6
16H-3W, 74–76	142.97	68.9	-58.2			6.77E-05	23.3
16H-4W, 74–76	144.49	96.2	-34.2			3.08E-05	44.1
16H-5W, 74–76	146.01	110.2	-21.6			4.70E-05	27.5
16H-6W, 71–73	147.49	86.9	-33.8			4.54E-05	33.7
17H-1W, 74–76	149.45	58.6	-66.2			3.57E-05	37.0
17H-2W, 74–76	150.95	10.2	18.9			2.62E-05	51.7
17H-3W, 74–76	152.45	75.8	-59.3			3.68E-05	32.2
17H-4W, 74–76	153.95	9.9	-43.8			2.18E-05	61.6
17H-5W, 74–76	155.45	45.8	-47.3			5.10E-05	21.2
17H-6W, 74–76	156.95	6.2	-12.3			2.57E-05	44.3
18H-2W, 74–76	160.45	192.7	-8.5			1.49E-05	80.6
18H-3W, 74–76	161.96	242.0	-1.6			7.36E-06	161.1
18H-4W, 74–76	163.48	222.8	46.1			2.72E-05	42.7
18H-6W, 55–57	166.31	169.9	55.3			1.81E-05	71.5
19H-1W, 75–77	168.46	158.8	-68.9			1.98E-05	62.6
19H-2W, 75–77	169.96	204.9	-28.1			2.42E-05	65.1
19H-3W, 75–77	171.46	144.8	-37.6			3.51E-05	44.7
19H-4W, 75–77	172.96	211.8	-46.9			3.05E-05	44.5
19H-5W, 75–77	174.46	179.3	-20.7			3.85E-05	29.8
19H-6W, 54–56	175.75	212.5	0.2			2.90E-05	49.8
19H-7W, 30–32	176.71	162.9	-36.5			4.35E-05	38.1
20H-2W, 75–77	179.46	78.7	-53.4			3.05E-05	40.1
20H-4W, 75–77	182.46	17.5	-41.1			1.76E-05	69.0
20H-6W, 50–52	185.21	49.7	-4.1			1.66E-05	83.3
21H-2W, 75–77	188.53	-71.4	61.0			8.12E-05	13.8
21H-4W, 75–77	191.56	247.8	58.9			5.54E-05	23.4
21H-6W, 40–42	193.93	256.0	-57.0			3.35E-05	43.4
22H-1W, 75–77	196.96	96.9	-19.3			3.28E-05	45.5
22H-2W, 75–77	198.46	102.3	-7.9			3.41E-05	46.2
22H-3W, 75–77	199.96	140.1	-37.4			8.81E-05	10.9
22H-4W, 75–77	201.46	101.7	-46.7			4.59E-05	28.2
22H-5W, 75–77	202.96	84.3	-31.7			2.25E-05	68.8
22H-6W, 75–77	204.46	126.3	-20.3			8.87E-05	13.4
23H-2W, 75–77	207.96	117.9	-56.8			9.53E-05	17.6
23H-3W, 75–77	209.46	99.3	-47.2			4.34E-05	29.2
23H-4W, 75–77	210.96	136.7	-48.1			6.83E-05	20.8
23H-5W, 75–77	212.46	154.6	-20.9			5.94E-05	10.3
23H-6W, 75–77	213.96	106.4	-54.6			3.47E-05	44.8

**Table T12 (continued).**

Core, section, interval (cm)	Depth (mbsf)	Declination 20 mT or PCA (°)	Inclination 20 mT or PCA (°)	PCA MAD (°)	PCA range (mT)	NRM 20 mT (A/m)	Measurement error (%)
24H-2W, 75–77	217.46	101.3	-42.2			3.64E-05	40.1
24H-4W, 75–77	220.46	142.9	-53.5	27.9	20–60	4.96E-05	26.3
23H-5W, 75–77	221.56	134.2	-54.8			4.96E-05	26.3
24H-6W, 75–77	222.67	73.6	-4.8			2.61E-05	55.2
25H-2W, 74–76	226.95	107.8	-65.8			6.04E-05	21.6
25H-3W, 74–76	228.45	111.7	-44.8			4.93E-05	20.4
25H-4W, 74–76	229.95	63.0	-31.4			5.39E-05	30.1
25H-6W, 44–46	232.65	100.8	-37.8			4.99E-05	26.8
26H-1W, 39–41	234.60	265.6	-16.9			3.71E-05	43.2
26H-3W, 74–76	236.28	-76.4	24.5			5.69E-05	23.8
26H-5W, 44–46	238.48	250.2	-25.0			4.86E-05	27.8
27X-1W, 69–71	242.60	46.7	49.4			2.87E-05	28.3
27X-3W, 60–62	245.51	17.6	-19.0			2.55E-05	49.4
28X-2W, 11–13	252.82	-21.1	-10.9			2.54E-05	65.8
30X-2W, 41–43	272.23	31.7	-13.8			6.19E-05	22.2
31X-1W, 50–52	280.81	-24.1	20.8			4.16E-05	37.7
32X-1W, 39–41	290.20	205.1	47.4	7.7	10–60	1.00E-04	15.8
33X-2W, 115–117	301.86	73.2	43.9			4.53E-05	25.9
33X-4W, 76–78	304.47	82.7	32.7			8.64E-05	10.0

Declinations for Cores 12H to 26H are corrected into geographical coordinates using FlexIT orientation data. PCA = principal component analysis, MAD = maximum angle of deviation, NRM = natural remanent magnetism.

**Table T13.** Magnetostratigraphic tie points, Site U1405. (Continued on next page.)

Chron boundary	Age (Ma)	Hole U1405A						Hole U1405B					
		Top		Bottom		Mid-point (mbsf)	Top		Bottom		Mid-point (mbsf)		
		Core, section, interval (cm)	Depth (mbsf)	Core, section, interval (cm)	Depth (mbsf)		Core, section, interval (cm)	Depth (mbsf)	Core, section, interval (cm)	Depth (mbsf)			
C5Br/C5Cn.1n	15.974	342-U1405A-5H-3, 140.0	39.10	342-U1405A-5H-4, 10.0	39.30	39.20	342-U1405B-5H-4, 125.0	39.25	342-U1405B-5H-5, 42.5	39.93	39.59		
C5Cn.1n/C5Cn.1r	16.268	6H-4, 140.0	50.10	6H-5, 10.0	50.30	50.20	7H-5, 140.0	59.90	7H-6, 20.0	60.20	60.05		
C5Cn.1r/C5Cn.2n	16.303	6H-7, 62.5	53.83	7H-1, 40.0	54.10	53.97	7H-7, 50.0	62.00	8H-1, 25.0	62.25	62.13		
C5Cn.2n/C5Cn.2r	16.472	7H-2, 40.0	55.60	7H-2, 95.0	56.15	55.88	8H-3, 10.0	65.10	8H-4, 70.0	67.20	66.15		
C5Cn.2r/C5Cn.3n	16.543	8H-1, 90.0	64.10	8H-1, 97.5	64.18	64.14	9H-3, 112.5	75.63	9H-4, 10.0	76.10	75.86		
C5Cn.3n/C5Cr	16.721	NI	NI	NI	NI	NI	9H-7, 30.0	80.50	10H-1, 27.5	81.28	80.89		
C5Cr/C5Dn	17.235	NI	NI	NI	NI	NI	NI	NI	NI	NI	NI		
C5Dn/C5Dr.1r	17.533	NI	NI	NI	NI	NI	NI	NI	NI	NI	NI		
C5Dr.1r/C5Dr.1n	17.717	NI	NI	NI	NI	NI	NI	NI	NI	NI	NI		
C5Dr.1n/C5Dr.2r	17.740	NI	NI	NI	NI	NI	NI	NI	NI	NI	NI		
C5Dr.2r/C5En	18.056	9H-3, 87.5	76.58	9H-4, 100.0	77.30	76.94	NI	NI	NI	NI	NI		
C5En/C5Er	18.524	NI	NI	NI	NI	NI	NI	NI	NI	NI	NI		
C5Er/C6n	18.748	10H-5, 92.5	89.13	10H-6, 10.0	89.80	89.47	NI	NI	NI	NI	NI		
C6n/C6r	19.722	NI	NI	NI	NI	NI	NI	NI	NI	NI	NI		
C6r/C6An.1n	20.040	NI	NI	NI	NI	NI	NI	NI	NI	NI	NI		
C6An.1n/C6An.1r	20.213	NI	NI	NI	NI	NI	NI	NI	NI	NI	NI		
C6An.1r/C6An.2n	20.439	NI	NI	NI	NI	NI	NI	NI	NI	NI	NI		
C6An.2n/C6Ar	20.709	NI	NI	NI	NI	NI	NI	NI	NI	NI	NI		
C6Ar/C6AAn	21.083	NI	NI	NI	NI	NI	NI	NI	NI	NI	NI		
C6AAn/C6AAr.1r	21.159	NI	NI	NI	NI	NI	NI	NI	NI	NI	NI		
C6AAr.1r/C6AAr.1n	21.403	NI	NI	NI	NI	NI	NI	NI	NI	NI	NI		
C6AAr.1n/C6AAr.2r	21.483	NI	NI	NI	NI	NI	NI	NI	NI	NI	NI		
C6AAr.2r/C6AAr.2n	21.659	NI	NI	NI	NI	NI	NI	NI	NI	NI	NI		
C6AAr.2n/C6AAr.3r	21.688	NI	NI	NI	NI	NI	11H-4, 15.0	94.36	11H-4, 30	94.51	94.44		
C6AAr.3r/C6Bn.1n	21.767	NI	NI	NI	NI	NI	12H-2, 140.0	102.90	12H-3, 32.5	103.33	103.11		
C6Bn.1n/C6Bn.1r	21.936	NI	NI	NI	NI	NI	13H-3, 117.5	113.68	13H-4, 35.0	114.35	114.01		
C6Bn.1r/C6Bn.2n	21.992	NI	NI	NI	NI	NI	13H-6, 77.5	117.78	13H-6, 100.0	118.00	117.89		
C6Bn.2n/C6Br	22.268	13H-4, 100	116.20	13H-5, 40	117.10	116.65	14H-7, 75.0	128.27	15H-1, 50.0	129.00	128.64		
C6Br/C6Cn.1n	22.564	14H-6, 132.5	129.05	14H-7, 35.0	129.58	129.32	15H-3, 87.5	131.69	15H-4, 82.5	133.14	132.41		
C6Cn.1n/C6Cn.1r	22.754	15H-4, 140.0	135.60	15H-5, 62.5	136.33	135.96	15H-4, 82.5	133.14	15H-4, 107.5	133.39	133.26		
C6Cn.1r/C6Cn.2n	22.902	17H-5, 100.0	155.70	17H-5, 135.0	156.05	155.88	17H-3, 140.0	151.90	17H-4, 20.0	152.20	152.05		
C6Cn.2n/C6Cn.2r	23.030	18H-7, 22.5	167.19	19H-1, 12.5	167.83	167.51	18H-3, 120.0	161.20	18H-4, 22.5	161.73	161.46		
C6Cn.2r/C6Cn.3n	23.233	20H-5, 40.0	183.60	20H-5, 115	184.35	183.98	20H-2, 55.0	178.05	20H-3, 15.0	179.16	178.61		
C6Cn.3n/C6Cr	23.295	21H-4, 117.5	191.975	21H-5, 10.0	192.37	192.17	21H-4, 137.5	191.40	21H-6, 10	193.14	192.27		

Ages from Gradstein et al. (2012). NI = not identified.



Table T13 (continued).

Chron boundary	Age (Ma)	Hole U1405C				
		Top		Bottom		
		Core, section, interval (cm)	Depth (mbsf)	Core, section, interval (cm)	Depth (mbsf)	Mid-point (mbsf)
		342-U1405C-		342-U1405C-		
C5Br/C5Cn.1n	15.974	5H-1, 122.5	36.43	5H-2, 102.5	37.725	37.08
C5Cn.1n/C5Cn.1r	16.268	NI	NI	NI	NI	NI
C5Cn.1r/C5Cn.2n	16.303	NI	NI	NI	NI	NI
C5Cn.2n/C5Cn.2r	16.472	8H-5, 122.5	70.93	8H-6, 22.5	71.425	71.18
C5Cn.2r/C5Cn.3n	16.543	9H-2, 107.5	75.78	9H-3, 40.0	76.600	76.19
C5Cn.3n/C5Cr	16.721	9H-5, 55.0	79.43	9H-6, 10.0	80.480	79.96
C5Cr/C5Dn	17.235	NI	NI	NI	NI	NI
C5Dn/C5Dr.1r	17.533	NI	NI	NI	NI	NI
C5Dr.1r/C5Dr.1n	17.717	NI	NI	NI	NI	NI
C5Dr.1n/C5Dr.2r	17.740	NI	NI	NI	NI	NI
C5Dr.2r/C5En	18.056	NI	NI	NI	NI	NI
C5En/C5Er	18.524	NI	NI	NI	NI	NI
C5Er/C6n	18.748	NI	NI	NI	NI	NI
C6n/C6r	19.722	NI	NI	NI	NI	NI
C6r/C6An.1n	20.040	NI	NI	NI	NI	NI
C6An.1n/C6An.1r	20.213	NI	NI	NI	NI	NI
C6An.1r/C6An.2n	20.439	NI	NI	NI	NI	NI
C6An.2n/C6Ar	20.709	NI	NI	NI	NI	NI
C6Ar/C6AAn	21.083	NI	NI	NI	NI	NI
C6AAn/C6AAr.1r	21.159	NI	NI	NI	NI	NI
C6AAr.1r/C6AAr.1n	21.403	NI	NI	NI	NI	NI
C6AAr.1n/A6AAr.2r	21.483	NI	NI	NI	NI	NI
C6AAr.2r/C6AAr.2n	21.659	NI	NI	NI	NI	NI
C6AAr.2n/C6AAr.3r	21.688	11H-4, 127.5	97.98	12H-5, 35.0	98.55	98.26
C6AAr.3r/C6Bn.1n	21.767	12H-1, 140.0	103.10	12H-2, 40.0	103.60	103.35
C6Bn.1n/C6Bn.1r	21.936	12H-6, 92.5	110.13	12H-7, 50.0	110.91	110.52
C6Bn.1r/C6Bn.2n	21.992	13H-2, 60.0	113.30	13H-2, 80.0	113.50	113.40
C6Bn.2n/C6Br	22.268	14H-4, 100.0	126.20	14H-5, 77.5	127.48	126.84
C6Br/C6Cn.1n	22.564	14H-7, 67.5	130.09	15H-1, 20.0	130.40	130.24
C6Cn.1n/C6Cn.1r	22.754	15H-2, 97.5	132.68	15H-3, 22.5	133.43	133.05
C6Cn.1r/C6Cn.2n	22.902	16H-2, 125.0	142.45	16H-3, 35.0	143.05	142.75
C6Cn.2n/C6Cn.2r	23.030	17H-6, 80.0	156.99	17H-6, 105.0	157.24	157.12
C6Cn.2r/C6Cn.3n	23.233	20H-2, 140.0	178.10	20H-5, 10.0	181.34	179.72
C6Cn.3n/C6Cr	23.295	21H-3, 112.5	188.84	21H-7, 45.0	194.20	191.52



**Table T14.** Summary of anisotropy of magnetic susceptibility of discrete samples, Hole U1405A. (Continued on next page.)

Core, section, interval (cm)	Depth (mbsf)	$\tau_3$	$V_3$ ( $^{\circ}$ )		$V_2$ ( $^{\circ}$ )		$V_1$ ( $^{\circ}$ )		Bulk susceptibility (SI)	Anisotropy (%)	$P$	$L$	$F$		
			Declination	Inclination	Declination	Inclination	Declination	Inclination							
342-U1405A-															
1H-1W, 75-77	0.76	0.3309	188.9	16.9	0.3329	98.3	1.9	0.3362	2.1	73.0	2.97E-04	0.5	1.016	1.010	1.006
1H-2W, 99-101	2.50	0.3317	211.7	35.8	0.3340	10.8	52.3	0.3343	114.3	10.2	5.13E-04	0.3	1.008	1.001	1.007
1H-3W, 69-71	3.70	0.3320	238.0	3.5	0.3339	344.9	78.1	0.3341	147.3	11.4	3.11E-04	0.2	1.006	1.001	1.006
1H-4W, 74-76	5.25	0.3325	333.0	0.4	0.3332	242.9	10.8	0.3343	64.9	79.2	4.48E-04	0.2	1.005	1.003	1.002
2H-1W, 74-76	6.95	0.3306	11.3	53.5	0.3337	227.1	31.0	0.3358	126.3	17.4	3.04E-04	0.5	1.016	1.006	1.009
2H-2W, 74-78	8.45	0.3330	247.0	31.7	0.3332	146.0	17.3	0.3337	31.7	52.9	5.58E-04	0.1	1.002	1.002	1.001
2H-3W, 74-76	9.95	0.3310	290.1	3.0	0.3326	198.8	24.4	0.3363	26.7	65.4	4.18E-04	0.5	1.016	1.011	1.005
2H-4W, 78-80	11.49	0.3311	210.2	70.0	0.3336	48.0	19.1	0.3353	316.1	5.7	3.33E-04	0.4	1.012	1.005	1.008
2H-5W, 74-76	12.95	0.3321	198.7	59.5	0.3329	99.2	5.5	0.3350	6.0	29.9	4.37E-04	0.3	1.009	1.006	1.002
2H-6W, 69-71	14.40	0.3311	98.8	5.8	0.3339	1.8	50.6	0.3350	193.5	38.8	1.91E-04	0.4	1.012	1.003	1.009
2H-7W, 36-38	15.57	0.3322	242.2	26.2	0.3330	135.9	29.7	0.3348	5.9	48.5	2.38E-04	0.3	1.008	1.005	1.002
3H-2W, 74-76	17.96	0.3298	135.0	7.8	0.3330	30.8	60.9	0.3372	229.1	27.9	3.00E-05	0.7	1.023	1.013	1.010
3H-3W, 74-76	19.50	0.3302	331.8	57.8	0.3332	117.2	27.4	0.3366	215.6	15.6	3.56E-05	0.6	1.019	1.010	1.009
3H-4W, 74-76	21.00	0.3265	220.8	46.1	0.3333	60.3	42.2	0.3402	321.2	9.9	4.59E-05	1.4	1.042	1.020	1.021
3H-6W, 66-68	22.45	0.3270	276.8	49.0	0.3322	32.0	20.3	0.3408	136.3	33.9	5.22E-05	1.4	1.042	1.026	1.016
3H-7W, 36-38	23.92	0.3276	147.9	2.8	0.3333	262.0	83.3	0.3390	57.6	6.2	5.15E-05	1.1	1.035	1.017	1.017
4H-1W, 74-76	25.12	0.3283	67.1	3.2	0.3333	335.6	25.8	0.3384	163.8	64.0	4.51E-05	1.0	1.031	1.015	1.015
4H-2W, 74-76	25.95	0.3279	82.1	16.4	0.3332	348.0	13.9	0.3389	219.6	68.3	5.20E-05	1.1	1.033	1.017	1.016
4H-3W, 74-76	27.45	0.3261	297.8	75.0	0.3343	184.6	6.0	0.3397	93.1	13.7	4.22E-05	1.4	1.042	1.016	1.025
4H-4W, 74-76	28.95	0.3290	240.5	25.7	0.3332	146.4	8.4	0.3378	39.6	62.8	4.21E-05	0.9	1.027	1.014	1.013
4H-5W, 74-76	30.45	0.3264	94.9	29.1	0.3340	248.1	58.0	0.3397	358.1	12.0	4.80E-05	1.3	1.041	1.017	1.023
4H-6W, 69-71	31.95	0.3258	312.1	29.8	0.3347	218.3	6.5	0.3395	117.3	59.3	4.34E-05	1.4	1.042	1.014	1.028
4H-1W, 74-76	33.40	0.3251	217.4	22.7	0.3356	122.5	11.7	0.3393	7.2	64.2	3.61E-05	1.4	1.044	1.011	1.032
4H-7W, 38-40	34.59	0.3261	309.7	65.0	0.3314	175.1	18.1	0.3425	79.5	16.6	4.45E-05	1.6	1.050	1.033	1.016
5H-1W, 75-77	35.46	0.3267	283.5	44.0	0.3338	17.2	3.8	0.3396	111.1	45.8	4.22E-05	1.3	1.039	1.017	1.022
5H-2W, 75-77	36.96	0.3313	69.1	65.5	0.3333	297.5	16.9	0.3354	202.1	17.3	4.45E-05	0.4	1.012	1.006	1.006
5H-3W, 75-77	38.46	0.3311	48.6	39.4	0.3335	282.4	35.8	0.3354	167.4	30.4	5.95E-05	0.4	1.013	1.006	1.007
5H-4W, 45-47	39.66	0.3278	75.2	4.6	0.3326	344.0	14.3	0.3395	182.4	75.0	4.60E-05	1.2	1.036	1.021	1.015
5H-5W, 75-77	41.46	0.3237	319.7	65.3	0.3334	80.2	13.1	0.3429	175.2	20.5	4.39E-05	1.9	1.059	1.028	1.030
5H-6W, 60-62	42.81	0.3278	257.5	20.0	0.3333	354.0	17.2	0.3390	121.6	63.1	4.14E-05	1.1	1.034	1.017	1.017
5H-7W, 30-32	44.01	0.3256	125.2	18.7	0.3326	0.5	59.2	0.3418	223.7	23.5	5.17E-05	1.6	1.050	1.028	1.021
6H-1W, 75-77	44.96	0.3260	297.7	43.6	0.3327	207.6	0.0	0.3413	117.6	46.4	3.93E-05	1.5	1.047	1.026	1.021
6H-2W, 85-87	46.56	0.3285	106.1	25.9	0.3341	265.7	62.6	0.3375	12.1	8.3	4.50E-05	0.9	1.027	1.010	1.017
6H-3W, 75-77	47.96	0.3300	232.8	45.8	0.3333	82.9	40.1	0.3367	339.4	15.5	4.53E-05	0.7	1.020	1.010	1.010
6H-4W, 75-77	49.46	0.3236	204.1	58.0	0.3358	91.4	13.6	0.3406	353.9	28.4	4.67E-05	1.7	1.053	1.014	1.038
6H-5W, 75-77	50.96	0.3267	351.5	11.7	0.3315	106.8	64.1	0.3418	256.5	22.8	5.00E-05	1.5	1.046	1.031	1.015
6H-6W, 75-77	52.46	0.3273	188.3	59.2	0.3343	38.5	27.3	0.3384	301.5	13.2	5.12E-05	1.1	1.034	1.012	1.021
6H-7W, 35-37	53.56	0.3267	278.9	61.6	0.3327	177.0	6.4	0.3407	83.7	27.6	3.90E-05	1.4	1.043	1.024	1.018
7H-1W, 75-77	54.46	0.3295	284.7	3.8	0.3322	191.7	38.5	0.3383	19.4	51.2	5.30E-05	0.9	1.027	1.018	1.008
7H-2W, 75-77	55.96	0.3254	223.0	39.3	0.3334	117.1	18.5	0.3412	7.6	44.9	5.34E-05	1.6	1.048	1.023	1.025
7H-3W, 65-67	57.36	0.3262	352.6	54.4	0.3328	96.6	9.9	0.3410	193.3	33.8	4.58E-05	1.5	1.046	1.025	1.020
7H-4W, 75-77	58.96	0.3270	233.0	27.2	0.3328	72.6	61.4	0.3403	327.3	8.2	4.77E-05	1.3	1.041	1.023	1.018
7H-5W, 75-77	60.46	0.3275	350.1	39.1	0.3350	231.7	30.3	0.3375	116.5	36.1	6.07E-05	1.0	1.031	1.007	1.023
7H-6W, 45-47	61.66	0.3277	33.8	21.3	0.3338	160.6	56.9	0.3385	293.8	24.0	5.39E-05	1.1	1.033	1.014	1.019
7H-7W, 33-35	62.54	0.3254	260.2	4.8	0.3330	355.9	50.4	0.3416	166.3	39.2	3.93E-05	1.6	1.050	1.026	1.023
8H-1W, 75-77	63.96	0.3271	228.0	15.8	0.3340	79.6	71.6	0.3389	320.6	9.2	4.31E-05	1.2	1.036	1.015	1.021
8H-2W, 75-77	65.46	0.3264	230.9	40.5	0.3363	23.9	46.2	0.3373	128.8	13.9	3.61E-05	1.1	1.033	1.003	1.030
8H-3W, 75-77	66.96	0.3302	109.1	6.5	0.3340	203.5	34.3	0.3357	9.8	54.9	4.45E-05	0.5	1.017	1.005	1.011
8H-4W, 75-77	68.46	0.3289	102.6	55.3	0.3336	232.0	23.7	0.3375	333.1	23.8	6.11E-05	0.9	1.026	1.012	1.014

**Table T14 (continued).**

Core, section, interval (cm)	Depth (mbsf)	$\tau_3$	$V_3$ ( $^{\circ}$ )		$V_2$ ( $^{\circ}$ )		$V_1$ ( $^{\circ}$ )		Bulk susceptibility (SI)	Anisotropy (%)	$P$	$L$	$F$		
			Declination	Inclination	Declination	Inclination	Declination	Inclination							
8H-6W, 75–77	69.96	0.3243	310.9	43.8	0.3371	129.9	46.2	0.3386	220.5	0.5	3.39E-05	1.4	1.044	1.004	1.040
8H-5W, 75–77	71.46	0.3283	240.4	19.3	0.3304	143.5	18.8	0.3414	12.7	62.5	3.73E-05	1.3	1.040	1.033	1.006
8H-7W, 35–37	72.56	0.3273	309.2	18.8	0.3346	190.5	54.8	0.3381	49.9	28.6	3.71E-05	1.1	1.033	1.010	1.022
9H-1W, 75–77	73.46	0.3290	246.9	50.9	0.3310	60.5	38.9	0.3400	153.1	3.1	3.65E-05	1.1	1.033	1.027	1.006
9H-2W, 75–77	74.96	0.3250	36.5	46.9	0.3289	298.1	7.8	0.3461	201.1	42.1	3.07E-05	2.1	1.065	1.052	1.012
9H-3W, 75–77	76.46	0.3273	121.2	77.5	0.3324	314.3	12.2	0.3403	223.7	2.8	3.90E-05	1.3	1.039	1.024	1.015
9H-4W, 75–77	77.96	0.3253	277.0	9.5	0.3364	175.7	49.3	0.3382	14.8	39.1	3.50E-05	1.3	1.040	1.005	1.034
9H-5W, 75–77	79.46	0.3277	302.6	37.1	0.3341	46.7	17.9	0.3382	157.2	47.4	3.69E-05	1.1	1.032	1.012	1.020
9H-6W, 70–72	80.91	0.3295	203.8	3.4	0.3332	296.3	36.3	0.3373	109.2	53.5	4.04E-05	0.8	1.024	1.013	1.011
9H-7W, 30–32	82.01	0.3262	222.5	10.1	0.3344	130.3	12.2	0.3394	351.1	74.0	3.92E-05	1.3	1.041	1.015	1.025

$\tau_1$ ,  $\tau_2$ , and  $\tau_3$  are eigenvalues, and  $V_3$ ,  $V_2$ , and  $V_1$  are eigenvectors associated with the minimum, intermediate, and maximum susceptibility, respectively. Measurement field = 300 A/m, sample volume = 7 cm<sup>3</sup>.  $P$  = anisotropy degree,  $L$  = lineation,  $F$  = foliation.



**Table T15.** Biostratigraphic and magnetostratigraphic datums, Hole U1405A.

Datum tie point	Datum	Datum type	Zone/Subzone	Age (Ma)	Depth (mbsf)		
					Top	Bottom	Mid-point
D01	T <i>Pseudoemiliania lacunosa</i>	Calcareous nannofossil	NN20	0.44	0.00	1.07	0.54
	T <i>Discoaster brouweri</i>	Calcareous nannofossil	NN19	1.93	2.57	4.07	3.32
	T <i>Discoaster pentaradiatus</i>	Calcareous nannofossil	NN18	2.39	4.07	5.10	4.59
	T <i>Discoaster surculus</i>	Calcareous nannofossil	NN17	2.49	4.07	5.10	4.59
	T <i>Sphenolithus</i> spp.	Calcareous nannofossil		3.54	5.10	5.70	5.40
	T <i>Reticulofenestra pseudoumbilicus</i>	Calcareous nannofossil	NN16	3.70	5.10	5.70	5.40
	T <i>Amaurolithus</i> spp.	Calcareous nannofossil		3.92	5.70	6.18	5.94
	B <i>Ceratolithus rugosus</i>	Calcareous nannofossil	NN13	5.12	6.18	11.90	9.04
D03	T <i>Sphenolithus heteromorphus</i>	Calcareous nannofossil	NN6	13.53	25.72	26.20	25.96
D04	Tc <i>Discoaster deflandrei</i>	Calcareous nannofossil		15.80	25.72	26.20	25.96
D07	Bc <i>Sphenolithus heteromorphus</i>	Calcareous nannofossil		17.71	62.88	65.83	64.36
D08	Tc <i>Sphenolithus belemnos</i>	Calcareous nannofossil	NN4	17.95	62.88	65.83	64.36
	T <i>Triquetrorhabdulus carinatus</i>	Calcareous nannofossil	NN3	18.28	82.31	92.19	87.25
	B <i>Sphenolithus belemnos</i>	Calcareous nannofossil		19.03	73.02	82.31	77.66
	B? <i>Sphenolithus disbelemnos</i>	Calcareous nannofossil		22.76	139.50	144.74	142.12
	B <i>Discoaster drugaii</i>	Calcareous nannofossil	NN2	22.82	158.48	162.83	160.66
	T <i>Sphenolithus capricornutus</i>	Calcareous nannofossil		22.97	174.50	175.36	174.93
	T <i>Sphenolithus delphix</i>	Calcareous nannofossil		23.11	175.36	175.66	175.51
	T <i>Dictyococcites bisectus</i> (>10 µm)	Calcareous nannofossil		23.13	175.66	176.76	176.21
	B <i>Sphenolithus delphix</i>	Calcareous nannofossil		23.21	198.80	201.80	200.30
D15	T <i>Sphenolithus ciperoensis</i>	Calcareous nannofossil	NN1	24.43	263.53	265.57	264.55
D15	Bc? <i>Triquetrorhabdulus carinatus</i>	Calcareous nannofossil		26.57	307.14	307.14	307.14
	T <i>Carpocanopsis cingulata</i>	Radiolarian	Lower RN4	17.16	35.29		35.29
	B <i>Calocyctella costata</i>	Radiolarian	Base RN4	17.59		35.29	35.29
	B <i>Dorcadopryris dentata</i>	Radiolarian	RN3	18.22	54.14	92.19	73.17
	X <i>Stichocorys delmontensis</i> – S. <i>wolffii</i>	Radiolarian	Base RN3	18.64	54.14	92.19	73.17
	T <i>Dorcadopryris ateuchis</i>	Radiolarian	Top RN2	18.64	54.14	92.19	73.17
D10	T <i>Theocyrtis annosa</i>	Radiolarian	Base RN2	20.05	92.19	110.82	101.51
	B <i>Calocyctella virginis</i>	Radiolarian	Base RN1	21.82	158.48	177.05	167.77
	B <i>Cyrtocapsella tetrapera</i>	Radiolarian	Base RN1	21.82	158.48	177.05	167.77
	T <i>Artophormis gracilis</i>	Radiolarian	RP22	22.41	158.48	177.05	167.77
	B <i>Eucyrtidium diaphanes</i>	Radiolarian	Mid-RP22	23.00	206.11	224.59	215.35
	T <i>Dorcadopryris papilio</i>	Radiolarian	Low RP22	23.59	186.61	206.11	196.36
	B <i>Lynchocanoma elongata</i>	Radiolarian	Base RP22	24.18	206.11	224.59	215.35
	B <i>Calocyctella robusta</i>	Radiolarian	Lower RP21	25.97		224.59	224.59
	B <i>Dorcadopryris ateuchis</i>	Radiolarian	Base RP21	28.64		224.59	224.59
	B <i>Praeorbulina sicana</i>	Planktonic foraminifer	M4b/M5	16.38	43.30	44.62	43.96
	B <i>Fohsella birnacea</i>	Planktonic foraminifer	M4a/M4b	16.69	59.30	60.80	60.05
	T <i>Catapsydrax dissimilis</i>	Planktonic foraminifer	M3/M4a	17.54	71.80	72.99	72.40
	T <i>Paragloborotalia kugleri</i>	Planktonic foraminifer	M1b/M2	21.12	102.20	105.20	103.70
	B <i>Globoquadrina dehiscens</i>	Planktonic foraminifer	M1a/M1b	22.44	158.45	160.80	159.63
	B <i>Paragloborotalia kugleri</i>	Planktonic foraminifer	O7/M1a	22.96	163.83	166.61	165.22
	B <i>Paragloborotalia pseudokugleri</i>	Planktonic foraminifer	O6/O7	25.21	237.09	241.89	239.49
	B <i>Globigerinoides primordius</i>	Planktonic foraminifer	O6	26.12	241.89	247.16	244.53
D05	C5Br/C5Cn.1n	Chron boundary		15.97		39.20	
	C5Cn.1n/C5Cn.1r	Chron boundary		16.27		50.20	
	C5Cn.1r/C5Cn.2n	Chron boundary		16.30		53.97	
	C5Cn.2n/C5Cn.2r	Chron boundary		16.47		55.88	
D06	C5Cn.2r/C5Cn.3n	Chron boundary		16.54		64.14	
	C5Dr.2r/C5En	Chron boundary		18.06		76.94	
	C5Er/C6n	Chron boundary		18.75		89.47	
	C6Bn.2n/C6Br	Chron boundary		22.27		116.65	
	C6Br/C6Cn.1n	Chron boundary		22.56		129.32	
	C6Cn.1n/C6Cn.1r	Chron boundary		22.75		135.96	
D12	C6Cn.1r/C6Cn.2n	Chron boundary		22.90		155.88	
	C6Cn.2n/C6Cn.2r	Chron boundary		23.03		167.51	
	C6Cn.2r/C6Cn.3n	Chron boundary		23.23		183.98	
D13	C6Cn.3n/C6Cr	Chron boundary		23.30		192.17	

T = top, Tc = top common, B = base, Bc = base common, X = faunal crossover. ? = uncertainty.



**Table T16.** Datum tie points, Hole U1405A.

Datum tie point	Datum	Datum type	Zone	Age (Ma)	Mid-point depth (mbsf)	Distance (m)	Duration (Ma)	LSR (cm/k.y.)	Notes
D01	T <i>Pseudoemiliania lacunosa</i>	Calcareous nannofossil	NN20	0.44	0.54				
D02	B <i>Ceratolithus rugosus</i>	Calcareous nannofossil	NN13	5.12	9.04	8.51	4.68	0.18	Average rate = 0.19 cm/k.y.
D03	T <i>Sphenolithus heteromorphus</i>	Calcareous nannofossil	NN6	13.53	25.96	16.92	8.41	0.20	
D04	Tc <i>Discoaster deflandrei</i>	Calcareous nannofossil		15.80	25.96	0.00	2.27	0.00	Hiatus
D05	C5Br/C5Cn.1n	Chron boundary		15.97	39.20	13.24	0.17	7.61	Average rate = 6.00 cm/k.y.
D06	C5Cn.2r/C5Cn.3n	Chron boundary		16.54	64.14	24.94	0.57	4.38	
D07	Bc <i>Sphenolithus heteromorphus</i>	Calcareous nannofossil		17.71	64.36	0.22	1.17	0.02	Hiatus
D08	T <i>Triquetrorhabdulus carinatus</i>	Calcareous nannofossil	NN3	18.28	87.25	22.89	0.57	4.02	
D09	Inferred hiatus			19.70	87.25	0.00	1.42	0.00	Hiatus
D10	T <i>Thecocystis annosa</i>	Radiolarian		20.05	101.51	14.26	0.35	4.07	
D11	Inferred hiatus			21.90	101.51	0.01	1.85	0.00	Hiatus
D12	C6Cn.1n/C6Cn.1r	Chron boundary		22.76	135.96	34.45	0.85	4.03	
D13	C6Cn.3n/C6Cr	Chron boundary		23.30	192.17	56.21	0.54	10.39	
D14	T <i>Sphenolithus ciperoensis</i>	Calcareous nannofossil	NN1	24.43	264.55	72.38	1.13	6.38	
D15	Bc? <i>Triquetrorhabdulus carinatus</i>	Calcareous nannofossil		26.57	307.14	42.59	2.14	1.99	

LSR = linear sedimentation rate. T = top, Tc = top common, B = base, Bc = base common. ? = uncertainty.

**Table T17.** Carbonate content and accumulation rates, Site U1405. (Continued on next two pages.)

Age (Ma)	LSR (cm/k.y.)	Dry density (g/cm <sup>3</sup> )	CaCO <sub>3</sub> (wt%)	MAR (g/cm <sup>2</sup> /k.y.)	CAR (g/cm <sup>2</sup> /k.y.)	nCAR (g/cm <sup>2</sup> /k.y.)
1.4	0.18	0.93	40.22	0.17	0.07	0.10
1.6	0.18	0.91	37.93	0.17	0.06	0.10
1.8	0.18	0.88	35.64	0.16	0.06	0.10
2.0	0.18	0.86	33.33	0.16	0.05	0.10
2.2	0.18	0.87	30.93	0.16	0.05	0.11
2.4	0.18	0.88	28.51	0.16	0.05	0.11
2.6	0.18	0.90	26.09	0.16	0.04	0.12
2.8	0.18	0.91	23.86	0.16	0.04	0.13
3.0	0.18	0.91	23.92	0.16	0.04	0.13
3.2	0.18	0.90	24.65	0.16	0.04	0.12
3.4	0.18	0.89	25.39	0.16	0.04	0.12
3.6	0.18	0.89	26.12	0.16	0.04	0.12
3.8	0.18	0.88	26.42	0.16	0.04	0.12
4.0	0.18	0.87	25.28	0.16	0.04	0.12
4.2	0.18	0.85	24.04	0.15	0.04	0.12
4.4	0.18	0.83	22.80	0.15	0.03	0.12
4.6	0.18	0.82	21.52	0.15	0.03	0.12
4.8	0.18	0.83	20.10	0.15	0.03	0.12
5.0	0.18	0.84	18.66	0.15	0.03	0.12
5.2	0.20	0.86	17.21	0.17	0.03	0.14
5.4	0.20	0.87	15.80	0.17	0.03	0.15
5.6	0.20	0.85	14.54	0.17	0.02	0.15
5.8	0.20	0.83	13.30	0.17	0.02	0.14
6.0	0.20	0.81	12.06	0.16	0.02	0.14
6.2	0.20	0.79	10.22	0.16	0.02	0.14
6.4	0.20	0.79	7.28	0.16	0.01	0.15
6.6	0.20	0.78	4.31	0.16	0.01	0.15
6.8	0.20	0.77	1.36	0.16	0.00	0.15
7.0	0.20	0.77	0.17	0.16	0.00	0.16
7.2	0.20	0.78	0.17	0.16	0.00	0.16
7.4	0.20	0.78	0.18	0.16	0.00	0.16
7.6	0.20	0.78	0.18	0.16	0.00	0.16
7.8	0.20	0.74	0.18	0.15	0.00	0.15
8.0	0.20	0.70	0.18	0.14	0.00	0.14
8.2	0.20	0.66	0.17	0.13	0.00	0.13
8.4	0.20	0.55	0.17	0.11	0.00	0.11
8.6	0.20	0.42	0.17	0.08	0.00	0.08
8.8	0.20	0.40	0.17	0.08	0.00	0.08
9.0	0.20	0.41	0.16	0.08	0.00	0.08
9.2	0.20	0.42	0.16	0.08	0.00	0.08
9.4	0.20	0.43	0.15	0.09	0.00	0.09
9.6	0.20	0.43	0.16	0.09	0.00	0.09



**Table T17 (continued).** (Continued on next page.)

Age (Ma)	LSR (cm/k.y.)	Dry density (g/cm <sup>3</sup> )	CaCO <sub>3</sub> (wt%)	MAR (g/cm <sup>2</sup> /k.y.)	CAR (g/cm <sup>2</sup> /k.y.)	nCAR (g/cm <sup>2</sup> /k.y.)
9.8	0.20	0.43	0.16	0.09	0.00	0.09
10.0	0.20	0.42	0.16	0.09	0.00	0.09
10.2	0.20	0.43	0.16	0.09	0.00	0.09
10.4	0.20	0.44	0.17	0.09	0.00	0.09
10.6	0.20	0.45	0.18	0.09	0.00	0.09
10.8	0.20	0.47	0.19	0.09	0.00	0.09
11.0	0.20	0.47	0.19	0.09	0.00	0.09
11.2	0.20	0.46	0.19	0.09	0.00	0.09
11.4	0.20	0.45	0.19	0.09	0.00	0.09
11.6	0.20	0.44	0.19	0.09	0.00	0.09
11.8	0.20	0.44	0.19	0.09	0.00	0.09
12.0	0.20	0.45	0.19	0.09	0.00	0.09
12.2	0.20	0.46	0.19	0.09	0.00	0.09
12.4	0.20	0.46	0.19	0.09	0.00	0.09
12.6	0.20	0.46	0.19	0.09	0.00	0.09
12.8	0.20	0.46	0.18	0.09	0.00	0.09
13.0	0.20	0.45	0.27	0.09	0.00	0.09
13.2	0.20	0.41	1.08	0.08	0.00	0.08
13.4	0.20	0.38	1.90	0.08	0.00	0.08
13.6	0.00	0.38	2.40	0.00	0.00	0.00
13.8	0.00	0.38	2.90	0.00	0.00	0.00
14.0	0.00	0.38	3.40	0.00	0.00	0.00
14.2	0.00	0.37	3.89	0.00	0.00	0.00
14.4	0.00	0.37	4.39	0.00	0.00	0.00
14.6	0.00	0.37	4.89	0.00	0.00	0.00
14.8	0.00	0.37	5.38	0.00	0.00	0.00
15.0	0.00	0.37	5.88	0.00	0.00	0.00
15.2	0.00	0.37	6.38	0.00	0.00	0.00
15.4	0.00	0.36	6.87	0.00	0.00	0.00
15.6	0.00	0.36	7.37	0.00	0.00	0.00
15.8	7.61	0.38	6.28	2.87	0.18	2.69
16.0	4.38	0.41	3.08	1.81	0.06	1.75
16.2	4.38	0.43	8.81	1.88	0.17	1.71
16.4	4.38	0.46	4.42	2.02	0.09	1.93
16.6	0.02	0.44	9.96	0.01	0.00	0.01
16.8	0.02	0.45	11.46	0.01	0.00	0.01
17.0	0.02	0.45	12.55	0.01	0.00	0.01
17.2	0.02	0.45	13.64	0.01	0.00	0.01
17.4	0.02	0.45	14.73	0.01	0.00	0.01
17.6	0.02	0.45	15.82	0.01	0.00	0.01
17.8	4.02	0.43	7.85	1.74	0.14	1.60
18.0	4.02	0.38	3.65	1.53	0.06	1.48
18.2	4.02	0.40	2.19	1.61	0.04	1.58
18.4	0.00	0.41	0.35	0.00	0.00	0.00
18.6	0.00	0.41	0.35	0.00	0.00	0.00
18.8	0.00	0.41	0.34	0.00	0.00	0.00
19.0	0.00	0.41	0.34	0.00	0.00	0.00
19.2	0.00	0.41	0.34	0.00	0.00	0.00
19.4	0.00	0.42	0.33	0.00	0.00	0.00
19.6	0.00	0.42	0.33	0.00	0.00	0.00
19.8	4.07	0.42	3.25	1.70	0.06	1.65
20.0	4.07	0.50	14.55	2.04	0.30	1.74
20.2	0.00	0.53	25.94	0.00	0.00	0.00
20.4	0.00	0.52	24.33	0.00	0.00	0.00
20.6	0.00	0.52	22.72	0.00	0.00	0.00
20.8	0.00	0.52	21.11	0.00	0.00	0.00
21.0	0.00	0.52	19.50	0.00	0.00	0.00
21.2	0.00	0.51	17.89	0.00	0.00	0.00
21.4	0.00	0.51	16.28	0.00	0.00	0.00
21.6	0.00	0.51	14.67	0.00	0.00	0.00
21.8	0.00	0.51	13.06	0.00	0.00	0.00
22.0	4.03	0.48	6.01	1.94	0.12	1.82
22.2	4.03	0.51	14.85	2.04	0.30	1.74
22.4	4.03	0.51	14.09	2.06	0.29	1.77
22.6	4.03	0.51	8.82	2.04	0.18	1.86
22.8	10.39	0.55	16.89	5.73	0.97	4.76
23.0	10.39	0.57	8.38	5.94	0.50	5.44
23.2	10.39	0.58	10.73	6.01	0.64	5.36
23.4	6.38	0.57	7.19	3.62	0.26	3.36



**Table T17 (continued).**

Age (Ma)	LSR (cm/k.y.)	Dry density (g/cm <sup>3</sup> )	CaCO <sub>3</sub> (wt%)	MAR (g/cm <sup>2</sup> /k.y.)	CAR (g/cm <sup>2</sup> /k.y.)	nCAR (g/cm <sup>2</sup> /k.y.)
23.6	6.38	0.56	3.23	3.55	0.11	3.44
23.8	6.38	0.63	7.01	4.02	0.28	3.74
24.0	6.38	0.69	8.27	4.37	0.36	4.01
24.2	6.38	0.67	7.00	4.26	0.30	3.96
24.4	6.38	0.68	5.32	4.32	0.23	4.09
24.6	1.99	0.82	6.45	1.63	0.11	1.52
24.8	1.99	0.88	6.27	1.75	0.11	1.64
25.0	1.99	0.87	6.51	1.73	0.11	1.62
25.2	1.99	0.89	6.88	1.76	0.12	1.64
25.4	1.99	0.89	7.43	1.77	0.13	1.64
25.6	1.99	0.89	8.09	1.77	0.14	1.62
25.8	1.99	0.90	9.01	1.78	0.16	1.62
26.0	1.99	0.92	10.37	1.84	0.19	1.65
26.2	1.99	0.93	10.30	1.86	0.19	1.66
26.4	1.99	0.92	7.75	1.84	0.14	1.69

LSR = linear sedimentation rate, MAR = mass accumulation rate, CAR = carbonate accumulation rate, nCAR = noncarbonate accumulation rate.

**Table T18.** Headspace gas sample geochemistry, Hole U1405A.

Core, section, interval (cm)	Depth (mbsf)	Methane (ppmv)
342-U1405A-		
1H-4, 0–5	4.50	1.59
2H-7, 0–5	15.20	1.65
3H-7, 0–5	24.75	1.82
4H-7, 0–5	34.20	2.13
5H-7, 0–5	43.70	2.25
6H-7, 0–5	53.20	2.29
7H-7, 0–5	62.20	2.53
8H-7, 0–5	72.20	2.42
9H-7, 0–5	81.70	2.96
10H-7, 0–5	91.20	2.48
11H-7, 0–5	100.70	2.64
12H-7, 0–5	109.96	2.70
13H-7, 0–5	119.70	2.95
14H-7, 0–5	129.23	3.20
15H-7, 0–5	138.71	2.95
16H-7, 0–5	148.27	3.45
17H-7, 0–5	157.70	2.35
18H-7, 0–5	166.96	2.57
19H-7, 0–5	176.40	2.57
20H-7, 0–5	185.92	2.88
21H-5, 0–5	192.27	2.89
22H-7, 0–5	205.12	2.99
23H-6, 0–5	213.20	2.68
24H-7, 0–5	223.37	2.96
25H-7, 0–5	233.32	3.12
26H-4, 94–99	237.98	3.32
27X-4, 0–5	246.40	3.49
28X-2, 0–5	252.70	3.07
29X-3, 0–5	264.10	2.59
30X-2, 0–5	271.81	2.54
31X-1, 0–5	280.30	2.43
32X-1, 0–5	289.80	2.43
33X-4, 0–5	303.70	3.01



**Table T19.** Interstitial water constituents, Hole U1405A.

Core, section, interval (cm)	Depth (mbsf)	pH	Alkalinity (mM)	Ammonium ( $\mu\text{M}$ )	Salinity	$\text{Cl}^-$ (mM)*	$\text{Cl}^-$ (mM)†	$\text{Na}^+$ (mM)	$\text{SO}_4^{2-}$ (mM)	$\text{HPO}_4^{2-}$ ( $\mu\text{M}$ )	$\text{Mn}^{2+}$ ( $\mu\text{M}$ )	$\text{Fe}^{2+}$ ( $\mu\text{M}$ )	$\text{Ca}^{2+}$ (mM)	$\text{Mg}^{2+}$ (mM)	$\text{Sr}^{2+}$ ( $\mu\text{M}$ )	$\text{K}^+$ (mM)	Sr/Ca	Mg/Ca
342-U1405A-																		
1H-3, 145–150	4.45	7.5	2.7	4	37	556.65	533.73	497.85	29.56	BDL	0.10	2.21	10.97	53.26	83.21	12.89	7.6	4.9
2H-6, 145–150	15.15	7.4	3.3	1	37	556.92	514.29	497.38	26.15	BDL	BDL	1.79	11.87	54.25	86.13	12.73	7.3	4.6
3H-6, 145–150	24.70	7.6	4.5	5	37	563.20	536.31	500.84	25.45	BDL	7.49	2.18	13.50	52.46	91.19	16.07	6.8	3.9
4H-6, 145–150	34.15	7.5	4.9	20	37	571.46	529.21	504.97	27.12	BDL	ND	ND	14.47	51.76	ND	12.45	ND	3.6
5H-6, 145–150	43.65	7.4	5.0	36	37	559.11	540.54	504.49	28.35	BDL	29.57	1.82	15.07	51.30	96.08	12.69	6.4	3.4
6H-6, 145–150	53.15	7.3	4.9	53	37	566.44	530.59	504.95	26.37	BDL	35.84	2.55	15.73	50.40	99.15	12.90	6.3	3.2
7H-6, 95–100	62.15	7.3	5.6	81	37	564.79	525.85	507.93	26.85	BDL	48.93	2.68	16.71	50.18	104.88	12.66	6.3	3.0
8H-6, 145–150	72.15	7.4	6.2	98	37	559.59	524.95	503.99	25.92	BDL	57.73	0.41	17.45	49.16	107.95	12.66	6.2	2.8
9H-6, 145–150	81.65	7.3	6.4	112	37	565.29	538.45	505.33	24.31	BDL	68.94	11.78	18.23	49.10	114.40	12.16	6.3	2.7
10H-6, 145–150	91.15	7.3	6.8	130	37	554.87	530.31	504.90	25.25	BDL	72.04	5.95	18.93	48.76	118.88	11.92	6.3	2.6
11H-6, 145–150	100.65	7.1	6.0	154	37	554.30	535.92	504.53	24.35	BDL	80.64	9.88	19.08	47.72	122.89	12.21	6.4	2.5
12H-6, 121–126	109.91	7.4	6.7	171	37	557.25	530.13	510.11	23.35	BDL	76.81	0.61	19.84	46.98	126.12	12.16	6.4	2.4
13H-6, 145–150	119.65	7.3	6.7	184	37	533.42	520.30	499.68	23.58	BDL	83.98	4.81	20.26	45.75	131.48	11.93	6.5	2.3
14H-6, 145–150	129.18	7.2	7.1	192	37	554.85	532.73	506.05	24.06	BDL	97.24	26.92	21.23	45.63	136.04	11.77	6.4	2.1
15H-6, 146–151	138.66	7.1	6.6	223	37	ND	541.23	509.24	24.60	BDL	88.46	25.13	21.57	45.15	137.34	14.33	6.4	2.1
16H-6, 146–151	148.23	7.1	7.1	233	37	ND	547.43	507.99	24.20	BDL	100.40	17.67	22.39	44.62	144.36	11.90	6.4	2.0
17H-6, 140–150	157.60	7.1	7.6	259	37	ND	515.53	507.56	24.11	BDL	105.93	15.36	23.00	43.69	147.44	10.95	6.4	1.9
18H-6, 111–121	166.86	7.3	8.1	271	38	ND	527.65	506.78	22.54	BDL	112.08	9.23	23.87	43.33	153.93	12.92	6.4	1.8
19H-6, 110–120	176.30	7.1	7.7	296	37	ND	525.06	504.30	22.13	BDL	109.79	8.14	24.05	42.27	155.01	12.92	6.4	1.8
20H-6, 112–122	185.82	7.0	8.2	305	38	ND	543.01	509.17	22.86	BDL	110.59	10.04	24.87	42.16	157.81	12.89	6.3	1.7
21H-4, 137–147	192.17	6.9	7.2	315	38	ND	565.84	490.56	24.68	BDL	107.33	13.89	24.39	40.25	157.72	10.25	6.5	1.6
22H-6, 132–142	205.02	7.1	8.8	308	38	ND	563.69	480.19	23.94	BDL	114.72	3.70	25.27	39.41	163.73	9.88	6.5	1.6
23H-5, 132–142	213.02	7.0	8.6	341	38	ND	575.78	487.84	24.84	BDL	119.01	37.19	25.83	39.50	167.89	9.95	6.5	1.5
24H-6, 136–146	223.27	7.5	8.4	332	37	ND	587.11	486.66	22.94	BDL	115.00	23.57	25.99	39.72	170.79	9.49	6.6	1.5
25H-6, 102–112	233.22	6.9	7.8	307	38	ND	575.55	486.81	21.37	BDL	111.19	27.57	26.67	40.22	175.00	8.74	6.6	1.5
27X-3, 140–150	246.30	7.0	7.7	349	38	ND	562.44	488.26	23.48	BDL	93.48	24.92	26.92	39.51	184.23	9.12	6.8	1.5
29X-2, 140–150	264.00	ND	ND	343	37	ND	564.35	481.26	22.26	BDL	104.93	98.70	27.10	38.99	196.75	8.83	7.3	1.4
33X-3, 140–150	303.60	7.0	5.3	322	37	ND	559.42	460.64	19.74	BDL	64.50	2.83	28.54	40.28	215.76	6.26	7.6	1.4

\* = manual titration. † = ion chromatograph. BDL = below detection limit ( $\text{HPO}_4^{2-} = 0.2 \mu\text{M}$  and  $\text{Mn}^{2+} = 0.1 \mu\text{M}$ ) calculated as three times the standard deviation of multiple measures of a blank. ND = not determined.

**Table T20.** Sedimentary sample and bulk elemental geochemistry, Site U1405. (Continued on next three pages.)

Core, section, interval (cm)	Depth (mbsf)	CaCO <sub>3</sub> (wt%)	IC (wt%)	Corrected TC (wt%)	TN (wt%)	Corrected TOC (wt%)
342-U1405A-						
1H-1, 46–47	0.46	42.79	5.13	5.07	0.05	ND
1H-2, 70–71	2.20	40.72	4.88	5.07	0.09	0.19
1H-3, 38–39	3.38	33.28	3.99	4.08	0.07	0.09
1H-4, 38–39	4.88	23.29	2.79	2.87	0.08	0.08
2H-1, 38–39	6.58	26.74	3.21	3.26	0.06	0.05
2H-2, 38–39	8.08	21.61	2.59	2.69	0.06	0.10
2H-3, 38–39	9.58	15.85	1.90	1.98	0.07	0.08
2H-4, 38–39	11.08	11.23	1.35	1.45	0.07	0.10
2H-5, 38–39	12.58	0.17	0.02	0.13	0.08	0.11
2H-6, 27–28	13.97	0.18	0.02	0.15	0.08	0.13
2H-7, 19–20	15.39	0.17	0.02	0.11	0.06	0.09
3H-1, 38–39	16.08	0.17	0.02	0.12	0.08	0.10
3H-2, 38–39	17.59	0.15	0.02	0.21	0.44	0.19
3H-3, 38–39	19.13	0.16	0.02	0.56	0.29	0.54
3H-4, 38–39	20.63	0.19	0.02	0.18	0.38	0.16
3H-5, 38–39	22.13	0.19	0.02	0.11	0.07	0.09
3H-6, 38–39	23.63	0.19	0.02	0.28	0.10	0.26
3H-7, 17–18	24.92	0.18	0.02	0.21	0.10	0.19
4H-1, 38–39	25.58	1.76	0.21	0.74	0.13	0.53
4H-2, 38–39	27.08	7.90	0.95	1.04	0.08	0.09
4H-3, 38–39	28.58	8.02	0.96	1.25	0.17	0.29
4H-4, 38–39	30.08	4.60	0.55	0.83	0.10	0.28
4H-5, 38–39	31.58	0.20	0.02	0.15	0.08	0.13
4H-6, 38–39	33.08	2.28	0.27	0.59	0.11	0.32
4H-7, 20–21	34.40	0.56	0.07	0.38	0.11	0.31
5H-1, 39–40	35.09	0.34	0.04	0.35	0.11	0.31
5H-2, 38–39	36.58	3.79	0.45	0.76	0.10	0.31
5H-3, 38–39	38.08	6.71	0.80	1.03	0.08	0.23
5H-4, 22–23	39.42	0.19	0.02	0.11	0.08	0.09
5H-5, 36–37	41.06	1.68	0.20	0.47	0.08	0.27
5H-6, 30–31	42.50	0.22	0.03	0.27	0.11	0.24
5H-7, 15–16	43.85	7.45	0.89	1.25	0.27	0.36
6H-1, 38–39	44.58	12.35	1.48	1.87	0.10	0.39
6H-2, 42–43	46.12	6.13	0.74	0.97	0.08	0.23
6H-3, 38–39	47.58	4.10	0.49	0.88	0.12	0.39
6H-4, 38–39	49.08	13.49	1.62	1.85	0.51	0.23
6H-5, 38–39	50.58	5.43	0.65	0.80	0.08	0.15
6H-6, 38–39	52.08	11.69	1.40	1.69	0.08	0.29
6H-7, 18–19	53.38	12.53	1.50	1.71	0.31	0.21
7H-1, 38–39	54.08	3.60	0.43	0.56	0.07	0.13
7H-2, 38–39	55.58	6.51	0.78	1.09	0.09	0.31
7H-3, 33–34	57.03	10.22	1.23	1.44	0.10	0.21
7H-4, 38–39	58.58	1.75	0.21	0.48	0.11	0.27
7H-5, 38–39	60.08	0.80	0.10	0.35	0.11	0.25
7H-6, 24–25	61.44	1.03	0.12	0.27	0.08	0.15
7H-7, 16–17	62.36	4.82	0.58	0.90	0.11	0.32
8H-1, 38–39	63.58	9.99	1.20	1.46	0.11	0.26
8H-2, 38–39	65.08	16.52	1.98	2.39	0.25	0.41
8H-3, 38–39	66.58	13.52	1.62	1.92	0.11	0.30
8H-4, 38–39	68.08	3.77	0.45	0.62	0.19	0.17
8H-5, 38–39	69.58	0.18	0.02	0.29	0.17	0.27
8H-6, 38–39	71.08	4.34	0.52	0.91	0.24	0.39
8H-7, 19–20	72.39	0.27	0.03	0.41	0.12	0.38
9H-1, 37–38	73.07	4.64	0.56	0.93	0.11	0.37
9H-2, 38–39	74.58	0.22	0.03	0.29	0.11	0.26
9H-3, 38–39	76.08	2.05	0.25	0.30	0.00	0.05
9H-4, 38–39	77.58	8.58	1.03	1.26	0.05	0.23
9H-5, 38–39	79.08	5.36	0.64	ND	ND	ND
9H-6, 36–37	80.56	0.29	0.04	0.25	0.10	0.22
9H-7, 15–16	81.85	4.63	0.56	0.84	0.33	0.28
10H-1, 38–39	82.58	9.71	1.17	1.55	0.23	0.39
10H-2, 38–39	84.08	0.18	0.02	0.31	0.11	0.29
10H-3, 38–39	85.58	0.22	0.03	0.32	0.11	0.29
10H-4, 38–39	87.08	0.35	0.04	0.46	0.12	0.42
10H-5, 38–39	88.58	0.33	0.04	0.32	0.10	0.28
10H-6, 33–34	90.03	0.29	0.04	0.23	0.12	0.20

**Table T20 (continued).** (Continued on next page.)

Core, section, interval (cm)	Depth (mbsf)	CaCO <sub>3</sub> (wt%)	IC (wt%)	Corrected TC (wt%)	TN (wt%)	Corrected TOC (wt%)
10H-7, 17–18	91.37	1.27	0.15	0.45	0.11	0.30
11H-1, 38–39	92.08	2.25	0.27	0.74	0.11	0.47
11H-2, 38–39	93.58	10.11	1.21	1.52	0.41	0.31
11H-3, 38–39	95.08	6.01	0.72	1.04	0.11	0.32
11H-4, 38–39	96.58	7.18	0.86	1.22	0.19	0.36
11H-5, 38–39	98.08	4.91	0.59	0.97	0.78	0.38
11H-6, 38–39	99.58	5.78	0.69	0.95	0.65	0.26
11H-7, 17–18	100.87	27.27	3.27	3.57	0.09	0.30
12H-1, 38–39	101.58	12.24	1.47	1.65	0.33	0.18
12H-2, 38–39	103.08	9.75	1.17	1.46	0.43	0.29
12H-3, 38–39	104.58	0.28	0.03	0.31	0.10	0.28
12H-4, 38–39	106.08	3.98	0.48	0.99	0.14	0.51
12H-5, 38–39	107.58	5.63	0.68	1.09	0.51	0.42
12H-6, 18–19	108.88	8.03	0.96	1.32	0.12	0.36
12H-7, 15–16	110.11	1.63	0.20	0.43	1.07	0.23
13H-1, 38–39	111.08	15.12	1.81	2.12	0.10	0.31
13H-2, 38–39	112.58	9.91	1.19	1.63	0.11	0.44
13H-3, 38–39	114.08	22.68	2.72	3.03	0.11	0.31
13H-4, 38–39	115.58	16.19	1.94	2.27	0.11	0.33
13H-5, 38–39	117.08	19.46	2.33	2.73	0.10	0.40
13H-6, 38–39	118.58	19.48	2.34	2.65	0.10	0.31
13H-7, 15–16	119.85	12.27	1.47	1.79	0.11	0.32
14H-1, 38–39	120.58	15.29	1.83	2.39	0.11	0.56
14H-2, 38–39	122.08	21.54	2.58	2.95	0.10	0.37
14H-3, 38–39	123.59	13.06	1.57	1.91	0.10	0.34
14H-4, 38–39	125.09	0.44	0.05	0.39	0.10	0.34
14H-5, 38–39	126.59	9.15	1.10	1.42	0.10	0.32
14H-6, 38–39	128.11	11.38	1.36	1.66	0.10	0.30
14H-7, 15–16	129.38	7.06	0.85	1.28	0.12	0.43
15H-1, 38–39	130.08	21.24	2.55	2.78	0.09	0.23
15H-2, 38–39	131.58	5.34	0.64	0.85	0.10	0.21
15H-3, 38–39	133.08	0.36	0.04	0.39	0.11	0.35
15H-4, 38–39	134.58	22.95	2.75	2.94	0.09	0.19
15H-5, 38–39	136.08	26.06	3.13	3.47	0.09	0.35
15H-6, 38–39	137.58	13.26	1.59	2.07	0.11	0.48
15H-7, 13–14	138.84	20.13	2.41	2.88	0.12	0.47
16H-1, 38–39	139.58	4.18	0.50	0.75	0.10	0.25
16H-2, 38–39	141.08	15.49	1.86	2.34	0.10	0.48
16H-3, 38–39	142.60	8.59	1.03	1.23	0.10	0.20
16H-4, 38–39	144.12	12.15	1.46	ND	ND	ND
16H-5, 38–39	145.64	8.15	0.98	1.28	0.11	0.30
16H-6, 38–39	147.15	16.51	1.98	2.30	0.11	0.32
16H-7, 15–16	148.42	14.29	1.71	1.91	0.09	0.20
17H-1, 38–39	149.08	27.94	3.35	3.53	0.09	0.18
17H-2, 38–39	150.58	21.69	2.60	2.84	0.10	0.24
17H-3, 38–39	152.08	3.73	0.45	0.79	0.11	0.34
17H-4, 38–39	153.58	16.38	1.96	2.17	0.10	0.21
17H-5, 38–39	155.08	1.82	0.22	0.67	0.10	0.45
17H-6, 38–39	156.58	6.23	0.75	1.09	0.11	0.34
17H-7, 26–27	157.96	7.13	0.86	1.25	0.11	0.39
18H-1, 39–39	158.59	14.91	1.79	2.21	0.12	0.42
18H-2, 39–39	160.09	10.70	1.28	1.72	0.11	0.44
18H-3, 39–40	161.60	4.83	0.58	0.94	0.12	0.36
18H-4, 39–40	163.12	9.71	1.16	1.57	0.12	0.41
18H-4, 40–41	163.13	8.29	0.99	1.31	0.11	0.32
18H-6, 25–26	166.00	12.96	1.55	1.90	0.11	0.35
18H-7, 15–16	167.11	4.45	0.53	1.19	0.12	0.66
19H-1, 38–39	168.08	6.35	0.76	1.38	0.14	0.62
19H-2, 38–39	169.58	5.73	0.69	0.98	0.11	0.29
19H-3, 38–39	171.08	8.45	1.01	1.39	0.12	0.38
19H-4, 38–39	172.58	9.17	1.10	1.57	0.13	0.47
19H-5, 38–39	174.08	5.86	0.70	1.05	0.11	0.35
19H-5, 80–81	174.50	4.40	0.53	0.84	0.11	0.31
19H-5, 120–121	174.90	2.57	0.31	0.61	0.11	0.30
19H-6, 10–11	175.30	11.05	1.33	1.66	0.11	0.33
19H-6, 20–21	175.40	11.50	1.38	1.66	0.11	0.28
19H-6, 50–51	175.70	33.24	3.99	4.11	0.09	0.13
19H-6, 90–91	176.10	25.09	3.01	3.03	0.09	0.02
19H-7, 16–17	176.56	6.42	0.77	1.06	0.11	0.29

**Table T20 (continued).** (Continued on next page.)

Core, section, interval (cm)	Depth (mbsf)	CaCO <sub>3</sub> (wt%)	IC (wt%)	Corrected TC (wt%)	TN (wt%)	Corrected TOC (wt%)
19H-7, 50–51	176.90	2.19	0.26	0.66	0.12	0.40
20H-1, 38–39	177.58	5.89	0.71	1.39	0.09	0.68
20H-2, 38–39	179.08	2.18	0.26	0.76	0.13	0.50
20H-3, 38–39	180.58	11.52	1.38	1.95	0.12	0.57
20H-3, 110–111	181.30	10.98	1.32	1.80	0.12	0.48
20H-4, 10–11	181.80	45.65	5.47	5.97	0.11	0.50
20H-4, 38–39	182.08	24.06	2.89	ND	ND	ND
20H-4, 70–71	182.40	15.68	1.88	2.27	0.12	0.39
20H-4, 130–131	183.00	8.56	1.03	1.42	0.16	0.39
20H-5, 38–39	183.58	8.86	1.06	1.45	0.13	0.39
20H-5, 100–101	184.20	22.37	2.68	3.14	0.11	0.46
20H-6, 25–26	184.95	5.29	0.63	1.14	0.14	0.51
20H-7, 15–16	186.07	2.56	0.31	0.77	0.13	0.46
21H-1, 38–39	187.08	5.15	0.62	1.16	0.13	0.54
21H-2, 38–39	188.15	9.39	1.13	1.74	0.14	0.61
21H-3, 38–39	189.66	7.29	0.87	1.45	0.13	0.58
21H-4, 38–39	191.18	7.00	0.84	1.44	0.15	0.60
21H-5, 26–27	192.53	13.52	1.62	1.89	0.10	0.27
21H-6, 20–21	193.72	6.34	0.76	1.26	0.14	0.50
21H-CC, 20–21	194.58	4.87	0.58	1.00	0.14	0.42
22H-1, 38–39	196.58	7.28	0.87	1.40	0.14	0.52
22H-2, 38–39	198.08	4.44	0.53	0.99	0.13	0.46
22H-3, 38–39	199.58	14.10	1.69	2.18	0.12	0.48
22H-4, 38–39	201.08	10.54	1.27	1.68	0.14	0.41
22H-5, 38–39	202.58	6.85	0.82	ND	ND	ND
22H-6, 22–23	203.92	2.58	0.31	0.71	0.13	0.41
22H-7, 15–16	205.27	0.21	0.03	0.52	0.14	0.50
23H-1, 38–39	206.08	7.61	0.91	1.26	0.11	0.35
23H-2, 38–39	207.58	2.36	0.28	ND	ND	ND
23H-3, 38–39	209.08	1.97	0.24	1.00	0.13	0.76
23H-4, 38–39	210.58	4.04	0.48	ND	ND	ND
23H-5, 38–39	212.08	5.36	0.64	1.23	0.13	0.59
23H-6, 38–39	213.58	3.82	0.46	ND	ND	ND
24H-1, 38–39	215.58	1.45	0.17	ND	ND	ND
24H-2, 38–39	217.08	1.30	0.16	0.65	0.13	0.49
24H-3, 38–39	218.58	2.65	0.32	0.84	0.13	0.52
24H-4, 38–39	220.08	6.39	0.77	1.36	0.12	0.59
24H-5, 17–18	221.37	9.75	1.17	1.60	0.11	0.43
24H-6, 38–39	222.29	4.32	0.52	1.05	0.13	0.53
24H-7, 27–28	223.64	5.81	0.70	ND	ND	ND
25H-1, 38–39	225.08	13.06	1.57	2.07	0.12	0.50
25H-2, 38–39	226.58	7.58	0.91	1.45	0.14	0.54
25H-3, 38–39	228.08	3.05	0.37	1.00	0.14	0.63
25H-4, 38–39	229.58	8.75	1.05	1.42	0.12	0.37
25H-5, 38–39	231.08	11.85	1.42	ND	ND	ND
25H-6, 22–23	232.42	12.89	1.55	1.76	0.10	0.21
25H-7, 15–16	233.47	9.31	1.12	1.74	0.12	0.62
26H-1, 27–28	234.47	6.74	0.81	ND	ND	ND
26H-3, 30–31	235.83	9.13	1.10	1.52	0.11	0.43
26H-4, 30–31	237.34	5.65	0.68	1.00	0.11	0.32
26H-5, 30–31	238.33	6.74	0.81	1.28	0.12	0.47
26H-6, 30–31	239.23	5.87	0.70	1.27	0.11	0.57
26H-7, 30–31	240.73	3.03	0.36	0.71	0.12	0.35
27X-1, 42–43	242.32	13.10	1.57	1.90	0.11	0.33
27X-2, 40–41	243.80	6.03	0.72	1.03	0.12	0.31
27X-3, 40–41	245.30	4.70	0.56	0.91	0.12	0.35
27X-4, 20–21	246.60	5.39	0.65	1.03	0.11	0.38
28X-1, 30–31	251.80	12.15	1.46	1.86	0.11	0.40
28X-2, 22–23	252.92	5.65	0.68	1.00	0.12	0.32
29X-1, 29–30	261.39	2.90	0.35	0.70	0.12	0.35
29X-2, 29–30	262.89	7.46	0.89	1.15	0.11	0.26
29X-3, 29–30	264.39	6.59	0.79	1.11	0.12	0.32
30X-1, 71–72	271.41	6.30	0.76	1.09	0.11	0.34
30X-2, 51–52	272.32	6.17	0.74	1.07	0.11	0.33
31X-CC, 14–15	281.40	7.03	0.84	1.29	0.12	0.45
32X-1, 53–54	290.33	8.50	1.02	1.44	0.14	0.42
33X-1, 56–57	299.76	11.72	1.41	ND	ND	ND
33X-2, 75–76	301.45	7.48	0.90	1.04	0.09	0.14
33X-3, 59–60	302.79	6.00	0.72	ND	ND	ND

**Table T20 (continued).**

Core, section, interval (cm)	Depth (mbsf)	CaCO <sub>3</sub> (wt%)	IC (wt%)	Corrected TC (wt%)	TN (wt%)	Corrected TOC (wt%)
33X-4, 112–113	304.82	10.18	1.22	ND	ND	ND
33X-5, 85–86	306.05	5.19	0.62	0.96	0.11	0.34
342-U1405B-						
20H-1, 40–41	176.40	ND	ND	2.67	0.10	ND
20H-1, 80–81	176.80	14.82	1.78	2.10	0.11	0.32
20H-1, 120–121	177.20	15.94	1.91	2.29	0.11	0.38
20H-2, 10–11	177.60	21.55	2.58	2.95	0.10	0.37
20H-2, 10–11	177.60	19.68	2.36	ND	ND	ND
20H-2, 20–21	177.70	33.82	4.05	4.25	0.09	0.20
20H-2, 50–51	178.00	56.68	6.80	6.89	0.07	0.09
20H-2, 80–81	178.30	24.65	2.96	3.20	0.11	0.24
20H-2, 110–111	178.60	19.67	2.36	2.73	0.11	0.37
20H-2, 140–141	178.90	12.36	1.48	1.78	0.10	0.30
20H-3, 10–11	179.11	4.56	0.55	0.86	0.11	0.31
20H-3, 50–51	179.51	3.05	0.37	0.70	0.11	0.33
20H-3, 90–91	179.91	6.57	0.79	1.19	0.12	0.40
20H-3, 130–131	180.31	5.21	0.62	0.95	0.10	0.33
20H-4, 15–16	180.68	6.99	0.84	1.21	0.12	0.37
20H-4, 55–56	181.08	1.29	0.16	0.59	0.12	0.44
20H-4, 95–96	181.48	2.67	0.32	0.71	0.12	0.39
20H-4, 145–146	181.98	6.50	0.78	1.32	0.13	0.54
342-U1405C-						
16H-3, 20–21	142.90	9.86	1.18	ND	ND	ND
16H-3, 60–61	143.30	9.36	1.12	1.67	0.09	0.55
16H-3, 100–101	143.70	4.29	0.51	0.93	0.09	0.42
16H-3, 141–142	144.11	13.64	1.64	2.38	0.09	0.74
16H-4, 30–31	144.50	0.44	0.05	0.48	0.09	0.43
16H-4, 30–31	144.50	0.41	0.05	ND	ND	ND
16H-4, 50–51	144.70	38.72	4.64	ND	ND	ND
16H-4, 80–81	145.00	25.17	3.02	ND	ND	ND
16H-4, 120–121	145.40	17.23	2.07	ND	ND	ND
16H-5, 10–11	145.80	4.78	0.57	0.92	0.10	0.35
16H-5, 50–51	146.20	11.76	1.41	ND	ND	ND
16H-5, 90–91	146.60	6.46	0.78	1.26	0.10	0.48
16H-5, 130–131	147.00	6.00	0.72	1.24	0.12	0.52

For total carbon (TC) with high-carbonate La Luna shale calibration, if TC < 2.2/2.913, corrected TC = 2.913 × x; if TC > 2.2/2.913, corrected TC = 2.2 + (x – 2.2/2.913) × 0.901. Corrected total organic carbon (TOC) is corrected TC minus inorganic carbon (IC). Total nitrogen (TN) values are uncorrected with anomalous values (>0.25%) removed. ND = not determined.

**Table T21.** Core top and composite depth, Site U1405. (Continued on next page.)

Core	Depth		Cumulative offset (m)	Comment	Data set used
	(mbsf)	(m CCSF)			
342-U1405A-					
1H	0.00	0.10	0.10	0.10	Tentative
2H	6.20	5.95	-0.35	-0.25	Tentative
3H	15.70	20.05	4.60	4.35	Tentative
4H	25.20	30.35	0.80	5.15	Tentative
5H	34.70	42.05	2.20	7.35	XRF core scanning
6H	44.20	57.75	6.20	13.55	Tentative
7H	53.70	80.25	13.00	26.55	Unidentified hiatus
8H	63.20	91.35	1.60	28.15	XRF core scanning
9H	72.70	104.78	3.93	32.08	Tentative
10H	82.20	116.03	1.75	33.83	XRF core scanning
11H	91.70	126.73	1.20	35.03	XRF core scanning
12H	101.20	136.63	0.40	35.43	XRF core scanning
13H	110.70	148.28	2.15	37.58	Tentative
14H	120.20	160.58	2.80	40.38	XRF core scanning
15H	129.70	170.56	0.48	40.86	Tentative
16H	139.20	180.41	0.35	41.21	Tentative
17H	148.70	191.91	2.00	43.21	XRF core scanning
18H	158.20	201.73	0.32	43.53	Tentative
19H	167.70	212.33	1.10	44.63	XRF core scanning

Table T21 (continued).

Core	Depth		Offset (m)	Cumulative offset (m)	Comment	Data set used
	(mbsf)	(m CCSF)				
20H	177.20	232.53	10.70	55.33	Hiatus Section 3	XRF core scanning
21H	186.70	242.38	0.35	55.68		XRF core scanning
22H	196.20	252.08	0.20	55.88		XRF core scanning
23H	205.70	263.03	1.45	57.33		XRF core scanning
24H	215.20	273.63	1.10	58.43		XRF core scanning
25H	224.70	283.63	0.50	58.93		XRF core scanning
26H	234.20	293.18	0.05	58.98		XRF core scanning
27X	241.90	300.93	0.05	59.03	Tentative	Physical properties
28X	251.50	310.54	0.01	59.04	Tentative	Physical properties
29X	261.10	320.15	0.01	59.05	Tentative	Physical properties
30X	270.70	329.76	0.01	59.06	Tentative	Physical properties
31X	280.30	339.37	0.01	59.07	Tentative	Physical properties
32X	289.80	348.88	0.01	59.08	Tentative	Physical properties
33X	299.20	358.29	0.01	59.09	Tentative	Physical properties
342-U1405B-						
1H	0.00	0.00	0.00	0.00	Tentative	Physical properties
2H	9.50	9.97	0.47	0.47	Tentative	Physical properties
3H	19.00	19.91	0.44	0.91	Tentative	Physical properties
4H	28.50	29.42	0.01	0.92	Drilling advance	
5H	33.50	42.14	7.72	8.64	Tentative	XRF core scanning
6H	43.00	59.24	7.60	16.24		XRF core scanning
7H	52.50	69.94	1.20	17.44		XRF core scanning
8H	62.00	79.45	0.01	17.45		XRF core scanning
9H	71.50	89.50	0.55	18.00	Tentative	XRF core scanning
10H	81.00	98.23	-0.77	17.23		XRF core scanning
11H	90.50	110.78	3.05	20.28		XRF core scanning
12H	100.00	120.58	0.30	20.58		XRF core scanning
13H	109.50	130.09	0.01	20.59		XRF core scanning
14H	119.00	138.59	-1.00	19.59		XRF core scanning
15H	128.50	154.59	6.50	26.09	Vertical flow	XRF core scanning
16H	138.00	181.59	17.50	43.59	Hiatus Section 3	XRF core scanning
17H	147.50	191.10	0.01	43.60	Tentative	XRF core scanning
18H	157.00	207.20	6.60	50.20		XRF core scanning
19H	166.50	216.81	0.11	50.31		XRF core scanning
20H	176.00	235.21	8.90	59.21		XRF core scanning
21H	185.50	244.26	-0.45	58.76		XRF core scanning
22H	195.00	256.96	3.20	61.96		XRF core scanning
23H	204.50	269.06	2.60	64.56		XRF core scanning
24H	214.00	278.13	-0.43	64.13		XRF core scanning
342-U1405C-						
1H	0.00	6.75	6.75	6.75	Tentative	Physical properties
2H	6.70	14.24	0.79	7.54	Tentative	Physical properties
3H	16.20	24.24	0.50	8.04	Tentative	Physical properties
4H	25.70	36.88	3.14	11.18		XRF core scanning
5H	35.20	45.50	-0.88	10.30		XRF core scanning
6H	44.70	55.01	0.01	10.31		XRF core scanning
7H	54.20	64.81	0.30	10.61		XRF core scanning
8H	63.70	74.32	0.01	10.62		XRF core scanning
9H	73.20	90.62	6.80	17.42		XRF core scanning
10H	82.70	99.45	-0.67	16.75		XRF core scanning
11H	92.20	109.19	0.24	16.99		XRF core scanning
12H	101.70	124.89	6.20	23.19		XRF core scanning
13H	111.20	136.84	2.45	25.64		XRF core scanning
14H	120.70	148.04	1.70	27.34	Tentative	XRF core scanning
15H	130.20	157.19	-0.35	26.99		XRF core scanning
16H	139.70	191.89	25.20	52.19	Hiatus Section 4	XRF core scanning
17H	149.20	203.50	2.11	54.30		XRF core scanning
18H	158.70	216.45	3.45	57.75		XRF core scanning
19H	168.20	224.80	-1.15	56.60		XRF core scanning
20H	175.20	231.85	0.05	56.65	Tentative	XRF core scanning
21H	184.70	241.75	0.40	57.05		XRF core scanning
22H	194.20	255.65	4.40	61.45		XRF core scanning
23H	203.70	266.35	1.20	62.65		XRF core scanning
24H	213.20	278.67	2.82	65.47		XRF core scanning
25H	222.50	286.67	-1.30	64.17	Tentative	XRF core scanning

XRF = X-ray fluorescence.



**Table T22.** Splice tie points, Site U1405.

Hole, core, section, interval (cm)	Depth		Hole, core, section, interval (cm)	Depth		Comment	Data set used
	(mbsf)	(m CCSF)		(mbsf)	(m CCSF)		
342-			342-				
U1405B-1H-6, 45	7.95	7.95	Tie to	U1405C-1H-1, 120	1.20	7.95	Tentative Physical properties
U1405C-1H-5, 9	6.09	12.84	Tie to	U1405B-2H-2, 137	12.37	12.84	Tentative Physical properties
U1405B-2H-5, 99	16.49	16.96	Tie to	U1405C-2H-2, 122	9.42	16.96	Tentative Physical properties
U1405C-2H-6, 21	14.41	21.95	Tie to	U1405A-3H-2, 39	17.60	21.95	Tentative Physical properties
U1405A-3H-4, 39	20.64	24.99	Tie to	U1405C-3H-1, 75	16.95	24.99	Tentative Physical properties
U1405C-3H-6, 105	24.75	32.79	Tie to	U1405A-4H-2, 94	27.64	32.79	Tentative Physical properties
U1405A-4H-7, 55	34.75	39.90	Tie to	U1405C-4H-3, 2	28.72	39.90	XRF core scanning
U1405C-4H-6, 70	33.14	44.32	Tie to	U1405A-5H-2, 77	36.97	44.32	XRF core scanning
U1405A-5H-6, 75	42.95	50.30	Tie to	U1405C-5H-4, 38	40.00	50.30	XRF core scanning
U1405C-5H-CC, 18	44.54	54.84	Append to	U1405C-6H-1, 0	44.70	55.01	XRF core scanning
U1405C-6H-5, 13	50.83	61.14	Tie to	U1405B-6H-2, 40	44.90	61.14	XRF core scanning
U1405B-6H-5, 92	49.92	66.16	Tie to	U1405C-7H-1, 135	55.55	66.16	XRF core scanning
U1405C-7H-6, 1	61.71	72.32	Tie to	U1405B-7H-2, 88	54.88	72.32	XRF core scanning
U1405B-7H-6, 112	61.12	78.56	Tie to	U1405C-8H-3, 124	67.94	78.56	XRF core scanning
U1405C-8H-6, 52	71.72	82.34	Tie to	U1405B-8H-2, 139	64.89	82.34	XRF core scanning
U1405B-8H-6, 118	70.68	88.13	Tie to	U1405A-7H-6, 38	61.58	88.13	Tentative XRF core scanning
U1405A-7H-7, 65	62.85	89.40	Append to	U1405B-9H-1, 0	71.50	89.50	XRF core scanning
U1405B-9H-5, 100	78.50	96.50	Tie to	U1405A-8H-4, 65	68.35	96.50	XRF core scanning
U1405A-8H-7, 40	72.60	100.75	Tie to	U1405B-10H-2, 102	83.52	100.75	XRF core scanning
U1405B-10H-7, 35	90.35	107.58	Tie to	U1405A-9H-2, 130	75.50	107.58	Tentative XRF core scanning
U1405A-9H-6, 53	80.73	112.81	Tie to	U1405C-11H-3, 62	95.82	112.81	XRF core scanning
U1405C-11H-5, 86	99.06	116.05	Tie to	U1405B-11H-5, 6	95.77	116.05	XRF core scanning
U1405B-11H-6, 68	97.91	118.19	Tie to	U1405A-10H-2, 66	84.36	118.19	XRF core scanning
U1405A-10H-6, 62	90.32	124.15	Tie to	U1405B-12H-3, 57	103.57	124.15	XRF core scanning
U1405B-12H-7, 21	109.21	129.79	Tie to	U1405C-12H-4, 40	106.60	129.79	XRF core scanning
U1405C-12H-7, 32	110.73	133.92	Tie to	U1405B-13H-3, 83	113.33	133.92	XRF core scanning
U1405B-13H-5, 103	116.53	137.12	Tie to	U1405C-13H-1, 28	111.48	137.12	XRF core scanning
U1405C-13H-3, 91	115.11	140.75	Tie to	U1405B-14H-2, 66	121.16	140.75	XRF core scanning
U1405B-14H-7, 82	128.34	147.93	Append to	U1405C-14H-1, 0	120.70	148.04	XRF core scanning
U1405C-14H-6, 76	128.96	156.30	Tie to	U1405B-15H-2, 90	130.21	156.30	Tentative XRF core scanning
U1405B-15H-5, 146	135.27	161.36	Tie to	U1405A-14H-1, 78	120.98	161.36	XRF core scanning
U1405A-14H-CC, 16	130.06	170.44	Append to	U1405A-15H-1, 0	129.70	170.56	XRF core scanning
U1405A-15H-CC, 16	139.41	180.27	Append to	U1405A-16H-1, 0	139.20	180.41	XRF core scanning
U1405A-16H-5, 142	146.68	187.89	Tie to	U1405B-16H-5, 30	144.30	187.89	Tentative XRF core scanning
U1405B-16H-6, 152	147.02	190.61	Append to	U1405B-17H-1, 0	147.50	191.10	XRF core scanning
U1405B-17H-5, 52	154.02	197.62	Tie to	U1405A-17H-4, 121	154.41	197.62	XRF core scanning
U1405A-17H-CC, 18	158.42	201.63	Append to	U1405A-18H-1, 0	158.20	201.73	XRF core scanning
U1405A-18H-3, 95	162.16	205.69	Tie to	U1405C-17H-2, 69	151.39	205.69	XRF core scanning
U1405C-17H-5, 80	156.00	210.30	Tie to	U1405B-18H-3, 10	160.10	210.30	XRF core scanning
U1405B-18H-5, 100	164.00	214.20	Tie to	U1405A-19H-2, 37	169.57	214.20	XRF core scanning
U1405A-19H-6, 42	175.62	220.25	Tie to	U1405B-19H-3, 44	169.94	220.25	XRF core scanning
U1405B-19H-6, 139	175.39	225.70	Tie to	U1405C-19H-1, 90	169.10	225.70	XRF core scanning
U1405C-19H-CC, 50	175.15	231.75	Append to	U1405C-20H-1, 0	175.20	231.85	XRF core scanning
U1405C-20H-4, 100	180.72	237.37	Tie to	U1405B-20H-2, 66	178.16	237.37	XRF core scanning
U1405B-20H-5, 140	183.44	242.65	Tie to	U1405C-21H-1, 90	185.60	242.65	XRF core scanning
U1405C-21H-3, 126	188.97	246.02	Tie to	U1405B-21H-2, 26	187.26	246.02	XRF core scanning
U1405B-21H-6, 138	194.42	253.18	Tie to	U1405A-22H-1, 110	197.30	253.18	XRF core scanning
U1405A-22H-4, 65	201.35	257.23	Tie to	U1405C-22H-2, 8	195.78	257.23	XRF core scanning
U1405C-22H-6, 26	201.96	263.41	Tie to	U1405A-23H-1, 38	206.08	263.41	XRF core scanning
U1405A-23H-6, 12	213.32	270.65	Tie to	U1405B-23H-2, 8	206.09	270.65	XRF core scanning
U1405B-23H-4, 107	210.12	274.68	Tie to	U1405A-24H-1, 105	216.25	274.68	XRF core scanning
U1405A-24H-7, 60	223.97	282.40	Tie to	U1405B-24H-3, 127	218.27	282.40	XRF core scanning
U1405B-24H-5, 102	221.05	285.18	Tie to	U1405A-25H-2, 5	226.25	285.18	XRF core scanning
U1405A-25H-4, 47	229.67	288.60	Tie to	U1405C-25H-2, 43	224.43	288.60	Tentative XRF core scanning
U1405C-25H-6, 80	230.86	295.03	Tie to	U1405A-26H-3, 52	236.05	295.03	XRF core scanning
U1405A-26H-CC, 38	241.86	300.84	Append to	U1405A-27X-1, 0	241.90	300.93	Physical properties
U1405A-27X-4, 73	247.13	306.16	Append to	U1405A-28X-1, 0	251.50	310.54	Physical properties
U1405A-28X-2, 53	253.23	312.27	Append to	U1405A-29X-1, 0	261.10	320.15	Physical properties
U1405A-29X-CC, 16	265.46	324.51	Append to	U1405A-30X-1, 0	270.70	329.76	Physical properties
U1405A-30X-CC, 12	272.61	331.67	Append to	U1405A-31X-1, 0	280.30	339.37	Physical properties
U1405A-31X-CC, 10	281.35	340.42	Append to	U1405A-32X-1, 0	289.80	348.88	Physical properties
U1405A-32X-CC, 30	291.08	350.16	Append to	U1405A-33X-1, 0	299.20	358.29	Physical properties
U1405A-33X-CC, 32	306.92	366.01					Physical properties

XRF = X-ray fluorescence.